Investigation of Performance and Fabrication of Metal Microfluidic Heat Sinks

by

Alireza Motieifar

A Thesis
Submitted to the Faculty of Graduate Studies of
The University of Manitoba
In Partial Fulfillment of the Requirements for the Degree of

MASTER OF SCIENCE

Department of Electrical and Computer Engineering
University of Manitoba
Winnipeg, Manitoba

Investigation of Performance and Fabrication of Metal Microfluidic Heat Sinks

By

Alireza Motieifar

A Thesis/Practicum submitted to the Faculty of Graduate Studies of The University of Manitoba in partial fulfillment of the requirement of the degree

Of

Master of Science

ABSTRACT

In this work, the temperature distribution on a microfluidic heat sink is studied using the FEM method. Microfluidic heat exchangers fabricated of copper, silicon, and nickel are simulated and studied in two cases; that of uniform and non-uniform heat sources. The first investigation assumes a uniform heat input of 100 W/cm^2 loaded on the top surface of a 1 cm × 1cm heat sink. The parametric dependence of the overall thermal resistance on the heat exchanger material, fluid velocity, and channel geometry is examined. Performance is compared based on the shape and size of the microchannels, their separating distance from each other, and the coolant flow rate. The cross section of the microchannels is rectangular and water is used as the coolant. It is shown that copper shows its superiority primarily at high channel height to width ratios and fluid mass fluxes. The second investigation assumes a non-uniform heat input consisting of either a 1 mm hot spot of 1000 W/cm^2 or a 3 mm hot spot of 500 W/cm^2 located at the center of the heat sink. These results show that the peak temperature of the hot spot depends on the solid material and the fluid flow rate. The effect of varying the thickness of material separating the coolant from the heat source is investigated. The optimum value for this thickness is ~50 μm for silicon and nickel, and ~100 μm for copper heat sinks. This study can be of importance in cooling of high-power Integrated Circuits (IC) that can have local peaks or hot spots with heat fluxes far exceeding 100 W/cm^2.

Finally, experimental fabrication of an electroplated copper micro-channel system with rectangular channels is shown. A process flow for fabrication of microfluidic heat sinks out of copper and a method and structure for testing it are proposed.

ACKNOWLEDGEMENTS

I would like to thank my advisor Dr. Cyrus Shafai for everything that I have learned from him and for his support during this project. I also thank Prof. Hassan M. Soliman from the department of Mechanical Engineering for teaching me all background science in fluid mechanics and heat transfer that I needed for this project, and for co-advising me through this research. Consulting with him and getting his suggestions were always very valuable. I also thank Prof. Douglas Buchanan for being a member of my project committee, and all of his advices and helps during my study at the University of Manitoba.

I also thank Dr. Behraad Bahreyni, Dr. Graham Ferrier, and Dr. Behzad Kordi for their comments on COMSOL Multiphysics software and FEM, and I especially thank Mr. Marc Levac for assisting me with ANSYS CFX simulations. I also acknowledge Mr. Guy Jonatschick and Mr. Mount-First Ng for installing upcoming versions of COMSOL Multiphysics software and maintaining the UNIX servers and computer systems.

I also appreciate the assistance of the researchers and staff of the Nano Systems Fabrication Laboratory at the University of Manitoba, especially Mr. Dwayne D. Chrusch, for helping me with the fabrication work.

Finally, I would like to gratefully acknowledge the financial support provided by the Natural Sciences and Engineering Research Council of Canada (NSERC).

TABLE OF CONTENTS

LIST OF FIGURES

LIST OF TABLES

NOMENCLATURE

C_f	Specific heat of the fluid
C_s	Specific heat of the solid
C_{th}	Overall thermal capacitance of the heatsink
D_h	Hydraulic diameter of the microchannel
f	Friction Factor
H_C	Channel height
H_B	Thickness of the solid layer under the channels
H_T	Thickness of the solid layer above the channels
k_f	Thermal conductivity of the fluid
k_s	Thermal conductivity of the solid
L	Channel length
L_{Hot}	Width of the hot area
$\dot{m}$	Total transferred fluid mass per second
P	Pressure of the fluid
q''	Input heat flux
Re	Reynolds number
R_{th}	Overall Thermal resistance of the heatsink
S	Channel separation (edge to edge)
T	Temperature
T_{in}	Inlet temperature of the fluid
T_{max}	Maximum temperature of the heat sink surface

T_W The wall temperature

u Fluid velocity in the x direction

v Fluid velocity in the y direction

w Fluid velocity in the z direction

w_m Mean axial fluid velocity (in z direction)

W Total width of the heat sink

W_C Channel width

x, y, z Cartesian coordinates

Greek Symbols:

ΔT Temperature rise (T - T_{in})

ΔT_f Temperature difference between incoming and outgoing water

ρ_f Density of the fluid

μ_f Dynamic viscosity of the fluid

Chapter 1

Introduction

Heat production in microprocessors is increasing with a high rate [1]. Modern microprocessors dissipate approximately 50 W/cm^2 power and have an area of a few cm^2. Making high performance heat sinks will increase the performance and power dissipation capability of modern microprocessors. Such heat sinks can be used also for cooling power electronics devices, high power laser diodes, and mechanical systems, which are currently cooled by large metallic heat sinks and fans, or macro-scale water circulating pipe networks.

Local hot spots are also of concern in the Integrated Circuits (IC) industry. Measurement of the input heat flux of ICs shows local peaks or hot spots far exceeding 100 W/cm^2. Chip temperature for these hot spots can exceed 70 °C and were shown to reach 105 °C [2], even when using state of the art packaging and cooling methods. This impacts their performance and reliability, since high junction temperatures reduce the mean time to failure of devices [3]. The 2005 International Technology Roadmap for Semiconductors (ITRS) indicated that the maximum allowable junction temperature will decrease from 100 °C to 90 °C by 2011 [4]. This reduction in allowed temperature will further challenge thermal cooling performance needs. In [5], the temperature variation on the surface of an HP microprocessor was simulated and compared to experimental measurements. This study showed that the temperature difference between the hottest and coolest points of the chip can reach 21 °C. The study in [6] showed a large variation in the temperature across the surface of a memory chip, and examined the effect of this

temperature variation on the thermal performance and characterization of electronic packages. This temperature difference generates stress in semiconductor electronic structures and metal interconnections, and degrades their performance or even can cause crack or disruptions [7]. The ideal situation is a uniform temperature across the entire surface of the chip.

Microfluidic heat sinks have commonly been fabricated in silicon substrates using micromachining methods. Tuckerman and Pease reported the first microfluidic heat sink in 1981 [8]. They made and tested a 1 cm × 1 cm water-cooled heat sink whose channels were made by anisotropic etching of silicon. A schematic of their heatsink is sketched in Figure 1-1. The width of their channels was 50 μm and the height was 320 μm. This heat sink could transfer 790 W/cm^2 with 2.27 W pumping power and maintaining a 71 °C temperature difference between the hottest point on the surface and the input fluid. That design is still one of the best, and that paper has been the basis for all other works in this field.

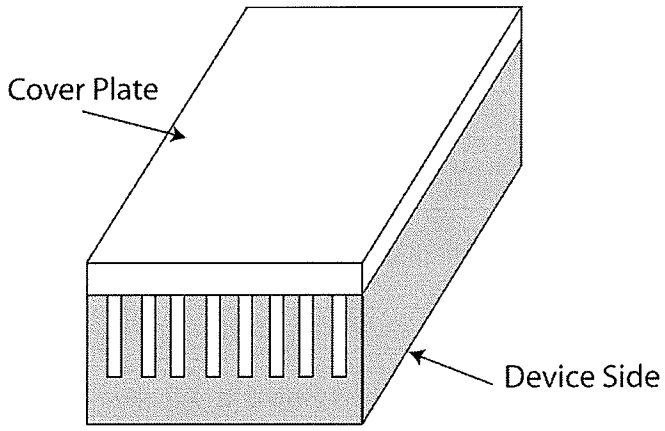

Figure 1-1. The schematic of a microfluidic heatsink with high-aspect-ratio rectangular microchannels. The channels are covered with a lid plate bonded to the substrate.

Fabrication of microfluidic heat sinks in metals is captivating due to the potential of higher heat conductance of some metals compared to silicon. Thermal conductivity of some materials is shown in Table 1-1.

Table 1-1. Thermal conductance of some materials.

	Material	**Thermal Conductance (W/mK)**
Insulators	Diamond	900 – 2320
	Glass	1.1
Metals	Silver	429
	Copper	401
	Gold	318
	Aluminum	237
	Silicon	148
	Nickel	90
	Stainless Steel	13 - 15
Fluids	Water	0.6
	Air	0.025

Thermal energy in metals is transferred by electrons and in insulators by phonons, or lattice vibrations [9]. In insulators the heat flux is carried almost entirely by phonon vibrations. The "electron fluid" of a conductive metallic solid conducts nearly all of the

heat flux through the solid. Phonon flux is still present, but carries less than 1% of the energy [9]. Electrons also conduct electric current through conductive solids, and the thermal and electrical conductivities of most metals have about the same ratio. A good electrical conductor, such as copper, usually also conducts heat well. In metals, thermal conductivity approximately tracks electrical conductivity according to the Wiedemann-Franz law, as freely moving valence electrons transfer not only electric current but also heat energy [10]. However, the general correlation between electrical and thermal conductance does not hold for other materials, due to the increased importance of phonon carriers for heat in non-metals. Diamond which has the strongest crystal structure and is the hardest known material, transfers lattice vibrations more easily and it has the best thermal conductance among solids. Among metals, silver, copper, gold and aluminum have the best conductance, and among them, considering price and heat conductance, copper looks to be the most suitable one to use as the heatsink material.

So far, considerable work has been done on the fabrication of silicon microfluidic heat sinks and also their thermal simulation and analysis. Microfluidic heat sinks in metal have been fabricated mainly by mechanical methods, which are difficult or expensive, and cannot produce narrow and high aspect ratio microchannels. Normally microchannels in metals have a circular shape, because of their fabrication method, which is micro-drilling. Hence many papers on thermal simulation of metal microfluidic heat sinks are based on circular microchannels [11]. In [12] the fabrication of rectangular microchannels was investigated, employing a photoresist mold and electroplating of nickel. Since the thermal conductivity of nickel is less than that of silicon, this method has a reduced advantage.

In this thesis, fabrication of microfluidic heatsink out of copper is investigated. The studied fabrication method is based on molding and electroplating. The channels are covered by a copper lid plate. This plated was bonded to the substrate using a thin layer of tin.

COMSOL Multiphysics software v.3.5a 64 bit [13] was used to simulate the temperature distribution on the surface of a water cooled microfluidic heat sink which is subject to a heat load on its surface. Microfluidic structures were simulated and analyzed using the Finite Element Method (FEM). The surface temperature of the heat sink was studied as a function of heat sink material and geometry, and fluid flow velocity. Three investigations are presented.

The first study assumes a uniform heat source. A detailed study on the comparative heat transfer performance of microfluidic heat sinks made out of nickel, silicon, and copper is presented. These three materials were selected due to their consideration by other groups in the fabrication of microfluidic heat sinks. The parametric dependence of the overall thermal resistance on the heat sink material, fluid velocity, and channel geometry is shown. Performance is compared based on the shape and size of the microchannels, their separating distance from each other, and the flow rate.

The second investigation assumes a non-uniform heat source. This study is of paramount importance in cooling of high-power ICs, which can have local peaks or hot spots with heat fluxes much higher than the average heat generation of the IC. Especially with the transition of microprocessor architectures to multicore design, the issue of thermal non-uniformity is attracting the attention of thermal design engineers [14]. By

varying the geometrical and material heat sink parameters, the effect of these parameters on the peak temperature of the hot spot was investigated, and the optimum heat sink structure for cooling an IC that includes a hot spot region was determined.

The third investigation is about the transient behavior of the heatsink. Transient simulation of the heatsink shows that its characteristic is like a first order differential equation. Hence microfluidic heatsink can be modeled as a first order RC circuit. Dependence of thermal capacitance of the heatsink on different parameters has been studied and it is demonstrated that how this thermal capacitance affects the peak temperature for the short term hot spots. This investigation is of paramount importance, because the hot spots on the cooled surfaces like microprocessors have a dynamic nature and the location of the hot spots and the amount of heat generated by them changes with time.

Chapter 2

Literature Review

Since the early work of Tuckerman and Pease [8] who introduced microfluidic heatsinks, a lot of research has been done in this field. Many researchers from the fields of mechanical engineering, chemical engineering, electrical engineering, and physics have been involved in research on microfluidic heatsinks and heat exchangers. Thousands of papers have been published about this, some conferences are held annually focusing on this subject or related to it, and even a few books have been published about this technology. A few companies have been founded who produce microfluidic heatsinks with different architectures and fabrication methods. Giant companies like IBM, Intel, AT&T, HP, NASA, and Toshiba also have been working on it. Microfluidic heatsinks have been in the market since a few years ago and thy have been used in some products like some desktop computers made by Sony and Apple. In this chapter a review of the papers and works done in the field of microfluidic heatsinks is presented. First the theoretical and experimental works will be briefly reviewed and then the fabrication methods used in the research and industry until now will be reviewed.

2.1. Theoretical and Experimental Study of Microfluidic Heatsinks

So far, many papers resulting from theoretical and experimental research work on microfluidic heatsinks have been published. Generally in these publications the heat source is considered as a uniform and steady heat input on one boundary of the heatsink. Most of the publications in this field consider these conditions. First a review of these publications will be presented, and then a few publications which discuss heatsinks with discrete or transient heat input will be reviewed.

2.1.1. Uniform Steady Heat Input

There are hundreds of papers about microfluidic heatsinks which consider uniform and steady heat input. In his section only a few most important ones are reviewed.

In [8] the first water-cooled integral heatsink was designed and tested. For the input power density of 790 W/cm^2 a maximum substrate temperature rise of 71 °C above the input water temperature was measured. Other conditions were $W_C = S = 50$ μm, $H_C =$ 302 μm, and flow rate = 8.6 cm^3/s. This result was in good agreement with theory. It was confirmed that the flow rate obeyed Poiseuille's equation, and that the thermal resistance was independent of power level.

In [15] a method for optimizing the structure of the microfluidic heatsink was presented. A computer code was written which obtained the optimum values for channel width and height and spacing. Their method for analyzing the heatsink uses thermal resistance models, and it shows that a design to obtain turbulent flow instead of laminar

flow makes a slight improvement in the thermal resistance while increasing the needed pumping power significantly.

In [16] the effect of the electric double layer (explained in section 8.3.3.1) at the solid-liquid interface and the fluid flow electrokinetic field on the pressure-driven flow and heat transfer through a rectangular microchannel were analyzed. The results show that the liquid flow and heat transfer are significantly influenced by the presence of the electric double layer and the induced electrokinetic flow. In this research W_C was 30 μm, H_C was 20 μm, and the mean fluid velocity was 1 m/s.

In [17] a three dimensional model was developed to investigate flow and heat transfer in the microchannel heat sink. The incompressible laminar Navier-Stokes equations were employed as the governing conservation equations which were numerically solved using the generalized single equation framework for solving conjugate problems. It has been validated using the experimental data in the literature. This work showed that the concept of the local heat transfer coefficient and Nusselt number is meaningless in the strongly conjugate problems. The studied structure had the following sizes: $W_C = 57$ μm, $H_C = 180$ μm, and $S = 43$ μm.

In [18] a three-dimensional fluid flow and heat transfer in a rectangular microchannel heat sink were analyzed numerically. A numerical code based on finite difference method and an algorithm called SIMPLE was developed to solve the governing equations. The analyzed heatsink has an area of 1 cm^2 and its microchannels have the following sizes: $W_C = 57$ μm, $H_C = 180$ μm, and $S = 43$ μm.

In [19] a scheme for solving the equations governing the fluid dynamics and combined conduction/convection heat transfer in a heatsink is presented. This scheme

enables the determination of heatsink dimensions that display the lowest thermal resistance. The results indicate that when the pressure drop is small, laminar solutions yield lower thermal resistance, while when the pressure drop is large, the optimal thermal resistance is found in the turbulent region. For this turbulent flow, the parameters of the optimal structure have the following values: Number of channels = 22, W_C = 377 μm, H_C = 365 μm, S = 81 μm, Re = 8459, and flow rate = 59.2 cm^3/s.

In [20] the pressure drop and heat transfer characteristics of a single-phase micro-channel heat sink were investigated both experimentally and numerically. The three-dimensional heat transfer characteristics of the heatsink were analyzed numerically by solving the conjugate heat transfer problem involving simultaneous determination of the temperature field in both the solid and liquid regions. The numerical results are in good agreement with the experimental ones and demonstrate that the conventional Navier-Stokes and energy equations can adequately predict the fluid flow and heat transfer characteristics of micro-channel heatsinks. The fabricated microchannels were 231 μm wide and 713 μm deep.

In [21] the steady, laminar flow and heat transfer equations are solved using a finite-volume method. It was found that the heat input lowers the frictional losses, especially at lower Reynolds numbers, where the temperature of the water increases and this reduces the viscosity, hence the frictional losses decrease. The simulated structures had the following sizes: W = 1 cm, L = 1 cm, W_C = 50 – 64 μm, H_C = 280 - 302 μm and S = 36 – 50 μm.

The experiments in [22] and [23] showed that the geometric configuration had a significant effect on the single-phase convective heat transfer and flow characteristics.

The laminar heat transfer was found to be dependent upon the aspect ratio and the ratio of the hydraulic diameter to the pitch of the microchannels. The turbulent flow resistance was usually smaller than that predicted by classical relationships and the Reynolds number for flow transition to fully developed turbulent flow became much smaller than the ordinary channel flow. Empirical corrections were suggested for calculating both the heat transfer and pressure drop. Geometric parameters of the test sections had the following values: $W = 18$ mm, $L = 45$ mm, $W_C = 0.2 - 0.8$ mm, $H_C = 0.7$ mm.

In [24] the stacked microchannel heatsinks were studied. Stacked microchannel structure can provide a lower thermal resistance, because it provides a larger heat transfer area from solid to fluid. In this work a simple thermal resistance network model was developed to evaluate the overall thermal performance of a stacked microchannel heatsink. The aspect ratio, fin thickness, and the ratio of the channel width to fin thickness are the variables which were optimized. During the optimization the overall dimensions, number of layers and pumping power (product of pressure drop and flow rate) were fixed. This study indicated that reduction in thermal resistance can be achieved by optimizing the channel configuration, and the optimal number of layers for micro-channel under constant pumping power of 0.01 W is 3. The other constraints are as pressure drop to be less than 4 bar and flow rate to be less than 1 lit/min. The optimal structure has these sizes: $W_C = 107$ μm, $S = 41$ μm, and $H_C = 407$ μm.

In [25], in order to investigate the performance of the microchannel heat exchanger, three-dimensional numerical simulations and experiments on heat transfer behavior and pressure loss were performed. The measured pressure loss was in good agreement with analytical results. In their design, the area of the heatsink was 15 × 15

mm^2, and H_C = 180 μm, W_C = 57 μm, and S = 43 μm. The overall flow rate was 2.5 cm^3/s.

In [26] experiments were conducted to investigate heat transfer characteristics of water flowing through trapezoidal silicon microchannels with a hydraulic diameter ranging from 62 to 169 μm. Height of the channels were between 44 an 111 μm. A numerical analysis was also performed by solving a conjugate heat transfer problem. It was found out that experimentally determined Nusselt number in microchannels was lower than that predicted by numerical analysis. A roughness-viscosity model was applied to interpret the experimental results. Based on this model a modified Nusselt relationship was proposed whose result was in good agreement with experimental data.

In [27] and [28] experimental results have been obtained for forced convection in deep microchannels with the channel depth of about 1000 μm and channel width of 251 μm. This structure has reduced temperature non-uniformity in the substrate by utilizing high flow rates. It was also shown that increasing the channel depth can significantly improve the flow and heat transfer performance.

2.1.2. Discrete Heat Input

In [29] detailed power maps are shown of fully operational microprocessors obtained by imaging the temperature-dependent Infra-Red (IR) emission of chips that are cooled by a custom designed IR transparent heat sink.

In [30], the temperature variation on the surface of an HP microprocessor was simulated and compared to experimental measurements. This study showed that the temperature difference between the hottest and coolest points of the chip can reach 21 °C.

The study in [31] also showed a large variation in the temperature across the surface of a memory chip, and has examined the effect of this temperature variation on the thermal performance and characterization of the electronic packages.

In [32] a methodology developed to perform electro-thermal analysis of integrated circuits was presented. A circuit simulator (SPICE) and a thermal simulator (COMSOL) worked together to obtain the junction temperature of a single BJT transistor on a chip. The simulators had to be linked to each other, because some parameters depend on temperature, and hence the simulated system was nonlinear. The junction temperature was about 107.2°C at a power dissipation of 4.5 W.

2.1.3. Transient State Study

In [33] the transient heat transfer in forced convection for simultaneous hydrodynamically and thermally developing laminar flow inside a microchannel heatsink was studied by solving the steady momentum equation and the transient energy equation. A parametric study was performed to investigate the effects of channel width, height, and separating distance, Reynolds number and solid and fluid thermal conductivities. Silicon and InP were used as the wafer materials. Heatsink response to step function and pulsed variations of the uniform input heat were studied. Results showed that the time required for the heat transfer to reach steady state condition is longer for the system with taller channel or larger separating distance and smaller channel width or Reynolds number.

In [34] the transient thermal behavior of microchannel heatsinks during start up and over a short duration power surge was investigated. Three-dimensional conjugate heat transfer equations in the heatsink were numerically solved using finite control-

volume method. The behavior of heatsinks with different values for the fin width, channel width, material thickness between the top of the channels and top of the heatsink, and different heatsink materials was examined during start-up from a uniform initial temperature with a uniform input heat flux, followed by a short duration power surge from the steady-state conditions. It was concluded that increasing the fin width or channel width increases the steady-state and maximum transient temperatures in the solid, and increasing the material thickness between the heatsink channels and the chip or using a material with larger density or specific heat increases the transient period and lowers the maximum transient temperature in the solid during the power surge.

In [35] a microfluidic heatsink was designed and fabricated with a heater, microchannels and distributed temperature sensors. This device allowed an experimental study of the transient behavior of a thermal microfluidic heatsink. The transient temperature behavior of the device was studied for a variety of heater power levels and forced convection flow rates. De-Ionized (DI) water was used as the working fluid. Both heating-up rise time and cooling-down fall time due to a step current input were determined for natural and forced convection heat transfer. The transient temperature response to a sinusoidal power input was also investigated. The resulting temperature distribution was measured as a function of the input signal and the flow rate. The step response under natural convection is exponential for both heating and cooling processes. However, under forced convection, the heating-up time response exhibits a clear overshoot. The response time for both heating and cooling process is about four times faster than that for the natural convection case. Furthermore, under certain conditions, the

periodic temperature response can exhibit a large peak–peak temperature without the occurrence of dry-out phenomenon.

2.2. Fabrication of Microfluidic Heatsinks

The first microfluidic heatsink was made by anisotropic etching of a silicon surface with <110> crystallographic orientation using KOH. The fabricated channels were 320 μm deep and 50 μm wide [8]. The channels were covered by anodic bonding of a glass plate to the silicon substrate. This method has been the most popular method for fabrication of microfluidic heatsinks. In [27] channels with the depth of 1030 μm and width of 251 μm were etched in a 2 mm thick silicon wafer. In [25] the channels were covered with another silicon wafer directly bonded to the substrate. Cooligy company also fabricates its microfluidic heatsinks with KOH etching and anodic bonding to a glass plate [36]. In [26] trapezoidal microchannels with hydraulic diameters of 62 – 169 μm were fabricated by anisotropic etching of silicon. In [37] triangular microchannels with the width of 230 μm and height of 170 μm were fabricated by anisotropic etching of silicon.

Another method for making microfluidic heatsinks is machining the grooves in the metal plates. In [38] rectangular shaped microchannels were machined into stainless steel plates. The fabricated channels were 200 μm wide and 700 μm tall. In [39] a heat exchanger was fabricated by machining 100 μm deep and 200 μm wide channels in the copper foils and then an electro-polishing process to reduce the surface roughness. Several layers of foils were bonded to each other by diffusion bonding to make a multilayer microchannel structure.

In [39] microchannels were fabricated by wet chemical etching of aluminum foils too. In [40] microchannel structures were fabricated by wet chemical etching of 1 mm thick copper plates. Channels were 690 μm wide and 390 μm tall.

Gigabyte Company has produced and is selling devices for cooling CPU and graphic card [41]. These devices are based on copper and water containing anti-freezing and anti-corrosive materials is running in them.

The product of Pipeline Company has a patented design that can provide stable two-phase flow in a microchannel heatsink [42]. Their technology is based on micro-scale machining.

Micros Company has produced a high performance copper microfluidic heatsink called Normal Flow Cold Plate (NCP) that has thermal resistance of 0.03 Kcm^2/W with a relatively low pressure drop [43].

IBM research laboratory in Zurich has fabricated a jet impingement cold plate [44]. Its architecture is based on a micron-sized round nozzle array with interspersed drainage holes on a face-centered quadratic lattice. The latter has a novel parallel manifold that reduces the pressure drop for large numbers of nozzles. This structure is similar to branched hierarchical networks in animals and plants. These features were fabricated using micro-fabrication of silicon wafers followed by bonding processes.

In [45] a method for fabrication of the microfluidic heatsink directly on the back side of the chip was proposed. In this method, first microchannels with the depth of 100 μm were etched on the back of the silicon wafer. They then spin-coated a layer of high-viscosity sacrificial polymer onto the back of the chip, filling in the trenches. Next, a simple polishing step removed excess polymer. The filled trenches were then covered by

a porous overcoat, and the chip was gradually heated in a nitrogen environment. The heating caused the sacrificial polymer filling the trenches to decompose and leave the channels through the porous overcoat, leaving microfluidic channels behind. The porous overcoat was then covered with another polymer layer to make a watertight system. The researchers have so far demonstrated that their microchannels can withstand pressure of more than 35 psi.

In [46] a microfluidic heatsink was fabricated by electroplating nickel on a mold. The fabricated channels were about 10 μm wide and 40 μm tall. At the initial stage, nickel was plated in the space between the photoresist molds to form the channel walls. As electroplating continued, the metal began to form overhangs (Mushrooming). When the gap between the overhangs decreased to 1-2 μm, electroplating was stopped and the photoresist was removed with acetone. With more plating, the gap between the overhangs closed to form a sealed channel filled with electrolyte. Inside the hollow channel was equi-potential and thus no further electroplating occurred on the inside of the channel wall. The electrolyte remaining inside the channel was replaced with DI water from the ends of the channels.

In [47] a stacked microchannel heatsink was fabricated by etching the channels into the silicon wafers and then direct bonding of the silicon wafers to form the stacked structure. Microchannels were etched with DRIE method, and totally five silicon wafers were bonded to each other to make two layers of microchannels. Microchannels were 100 μm deep and 34 μm wide. It was discussed that eutectic bonding is not a suitable method for fabrication of microfluidic heatsinks.

Researchers of IBM in New York have fabricated a microfluidic heatsink with special zigzag channel pattern in silicon [48]. Channel with the depth of 269 μm and width of 60 μm were etched by DRIE method in a 525 μm thick silicon wafer. This substrate was directly bonded to another silicon wafer to seal the microchannels.

2.3. Contributions of This Work

To the best knowledge of the author, the following parts of this work are performed and presented for the first time:

1. Metal microfluidic heatsinks were simulated by COMSOL Multiphysics software in steady state and with uniform heat input. Simulation was performed for heatsinks made out of copper, silicon and nickel and for different sizes and fluid mean velocities, and the results were compared.
2. Microfluidic heatsinks with discrete heat input were simulated, and the results of the simulations for different cases of solid materials and sizes were compared and discussed. Before this, very limited work has been done on this issue by other groups.
3. Microfluidic heatsinks with uniform and discrete heat input were simulated in transient state. Before this, very limited work has been done on this issue by other groups.
4. A method for the fabrication of copper microfluidic heatsinks by electroplating is presented in this work. In previous works, copper microfluidic heatsinks were fabricated by etching or drilling, and electroplating was used to fabricate nickel microfluidic heatsinks.

Chapter 3

Simulation Method, Modeling and Simulated Structure

3.1. Simulated Structure

The simulated microfluidic heat sink was comprised of a large number of parallel microchannels, and it measured a total size of 1 × 1 cm^2. In the simulations it was modeled that the structure was either made up of copper, silicon, or nickel, and the length of the microchannels was L = 1 cm. The cooling fluid was pure water with the input temperature of 300 K. As shown in Figure 3-1, the microchannels had a rectangular cross section.

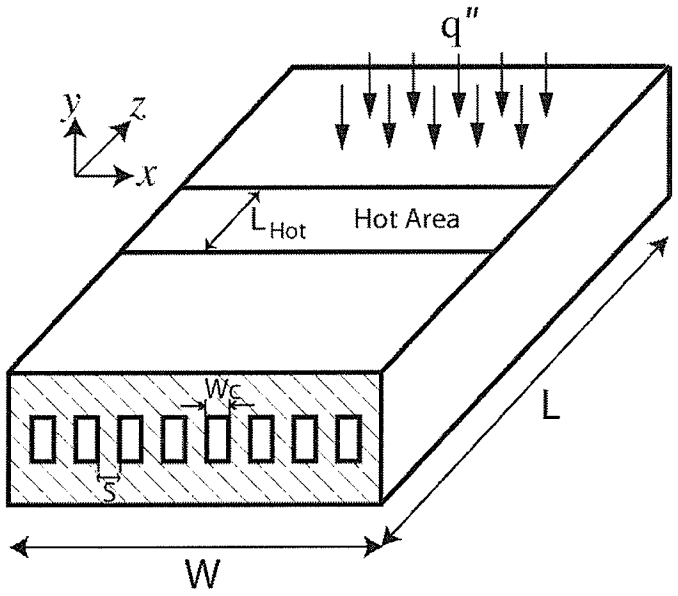

Figure 3-1. Microfluidic heat exchanger with rectangular microchannels.

For the case of a uniform heat input, a heat flux $q'' = 100$ W/cm^2 was applied uniformly to the heat sink top surface. For the case of a non-uniform heat input, the normal input heat flux applied at the top surface was 100 W/cm^2, but a hot spot was considered as a band across the surface of length (L_{Hot}) whose input heat flux was higher. The hot spot was centered at the middle of the top surface of the heat sink. Symmetry of the structure for the hot spot was chosen, because it generated a geometry that was more suitable for FEM simulation. This symmetry made it possible to simplify the simulated structure as a unit cell. These simulations were performed for hot spots of different sizes, $L_{Hot} = 1$ mm and 3 mm. For the hot spot of length $L_{Hot} = 1$ mm, the input heat was 1000 W/cm^2, and for the hot spot of length $L_{Hot} = 3$ mm, it was 500 W/cm^2. These values are in the range of the heat generation for the hot spots presented in [49 to 51].

In all simulated cases, using the benefit of the periodicity and symmetry across the structure, the simulated unit cell was only one half of a microchannel, as shown in Figure 3-2. In order to simulate fully developed flow inside the microchannels in the heat exchanger, and to provide the suitable boundary conditions, an adiabatic channel length of 1 cm was added before entering the solid structure. Uniform conditions of velocity and temperature ($u = 0$, $v = 0$, $w = w_m$, and $T = T_{in}$) were imposed at the inlet of the adiabatic entry length. At the outlet of the adiabatic exit section, the following conditions were imposed:

- Velocity in x and y directions is zero: $u = v = 0$
- Pressure at the outlet: $P = 0$
- Constant velocity along the channel at the outlet is zero: $\frac{\partial w}{\partial z} = 0$

- Temperature gradient along the channel at the outlet is zero: $\frac{\partial T}{\partial z} = 0$

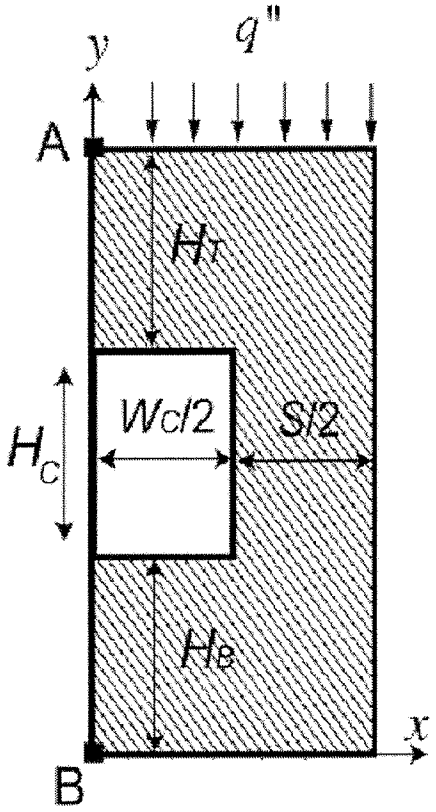

Figure 3-2. Cross-section of the simulated unit.

3.2. Simulation Method

Input heat was applied at the top surface and the boundary condition for the other outer surfaces was thermal insulation (No heat transfer). The complete mathematical formulation for determining the three components of velocity (u, v, and w), pressure (P), and temperature (T) in the fluid is given by the following equations:

Continuity equation (Constant velocity):

$$\frac{\partial u}{\partial x}+\frac{\partial v}{\partial y}+\frac{\partial w}{\partial z}=0 \tag{3-1}$$

Momentum equations:

$$\rho_f\left(u\frac{\partial u}{\partial x}+v\frac{\partial u}{\partial y}+w\frac{\partial u}{\partial z}\right)=-\frac{\partial P}{\partial x}+\mu_f\left(\frac{\partial^2 u}{\partial x^2}+\frac{\partial^2 u}{\partial y^2}+\frac{\partial^2 u}{\partial z^2}\right) \tag{3-2}$$

$$\rho_f\left(u\frac{\partial v}{\partial x}+v\frac{\partial v}{\partial y}+w\frac{\partial v}{\partial z}\right)=-\frac{\partial P}{\partial y}+\mu_f\left(\frac{\partial^2 v}{\partial x^2}+\frac{\partial^2 v}{\partial y^2}+\frac{\partial^2 v}{\partial z^2}\right) \tag{3-3}$$

$$\rho_f\left(u\frac{\partial w}{\partial x}+v\frac{\partial w}{\partial y}+w\frac{\partial w}{\partial z}\right)=-\frac{\partial P}{\partial z}+\mu_f\left(\frac{\partial^2 w}{\partial x^2}+\frac{\partial^2 w}{\partial y^2}+\frac{\partial^2 w}{\partial z^2}\right) \tag{3-4}$$

Energy equation:

$$u\frac{\partial T}{\partial x}+v\frac{\partial T}{\partial y}+w\frac{\partial T}{\partial z}=\frac{k_f}{\rho_f C_f}\left(\frac{\partial^2 T}{\partial x^2}+\frac{\partial^2 T}{\partial y^2}+\frac{\partial^2 T}{\partial z^2}\right) \tag{3-5}$$

Within the solid, there is only one unknown parameter, T, and then only one equation is required, which is the energy equation:

$$\frac{\partial^2 T}{\partial x^2}+\frac{\partial^2 T}{\partial y^2}+\frac{\partial^2 T}{\partial z^2}=\frac{\rho_f C_f}{k_f}\frac{\partial T}{\partial t} \tag{3-6}$$

For steady state conditions $\frac{\partial T}{\partial t}=0$.

The boundary conditions of zero velocity are imposed at all fluid-solid interfaces. Continuity of temperature and heat flux is also imposed at these interfaces. The thermal boundary condition for the top surface where heat comes in is [52]:

$$q''=k_s\frac{\partial T}{\partial y} \tag{3-7}$$

The hydraulic diameter for a rectangular channel is given by the formula [53]:

$$D_h=\frac{4(H_C\times W_c)}{2(H_C+W_c)} \tag{3-8}$$

Hydraulic diameter is the diameter of the circular channel with the same area and perimeter of the rectangular channel. This diameter is calculated in order to plug into the fluid dynamics equation which have been written for circular channel.

Applying a channel width of W_C = 50 μm and by varying the channel height H_C, the hydraulic diameters for several cases are shown in Table 3-1. We can see from Table 3-1 that the change in D_h with channel height is more significant for the smaller channel heights.

Table 3-1. Hydraulic diameters for channels with W_C = 50 μm and different heights (H_C).

H_C	D_h
50 μm	50 μm
100 μm	67 μm
200 μm	80 μm
500 μm	90.9 μm

Using these D_h values and Equation (3-9) given below [52], the Reynolds number is calculated for the water flow in microchannels with four different heights (50 μm, 100 μm, 200 μm and 500 μm), and mean fluid velocity (w_m) of 1 to 14 m/s. The fluid temperature is 300K in these calculations. The results are shown in Figure 3-3.

$$\mathrm{Re} = \frac{\rho_f w_m D_h}{\mu_f} \tag{3-9}$$

In Figure 3-3 it can be seen that for the mean fluid velocity (w_m) of 1 - 14 m/s and channel heights (H_C) of 50 - 500 μm, the Reynolds number remains below 1400, and so the flow is expected to be laminar.

Figure 3-4 shows the dynamic viscosity of water versus temperature. In these simulations, in order to have a linear set of equations (Equations. 3-1 to 3-7), the fluid's dynamic viscosity (μ_f) was considered a constant value in each simulation (0.00089 Pa.s). This is generally a good approximation if μ_f is estimated correctly and related to the average temperature of the fluid flowing inside the heat exchanger. Since, as observed in

Figure 3-4, μ_f highly depends on the water temperature, for higher values of H_C and w_m where the cooling performance is greater and the overall temperature is lower, a larger value for μ_f (0.00089 Pa.s) can be set and for the cases that the overall temperature is higher, a lower value can be set for μ_f. For example for the average fluid temperature of about 80°C the value for dynamic viscosity can be set to 0.0004 Pa.s. Of course as it was tried with some simulations, the heatsink performance and the maximum temperature of the surface didn't depend much on the fluid viscosity. The only parameter that changes with the fluid viscosity is the pressure drop along the channel. Hence for all of the simulation in this thesis the constant value of μ_f = 0.00089 Pa.s was used.

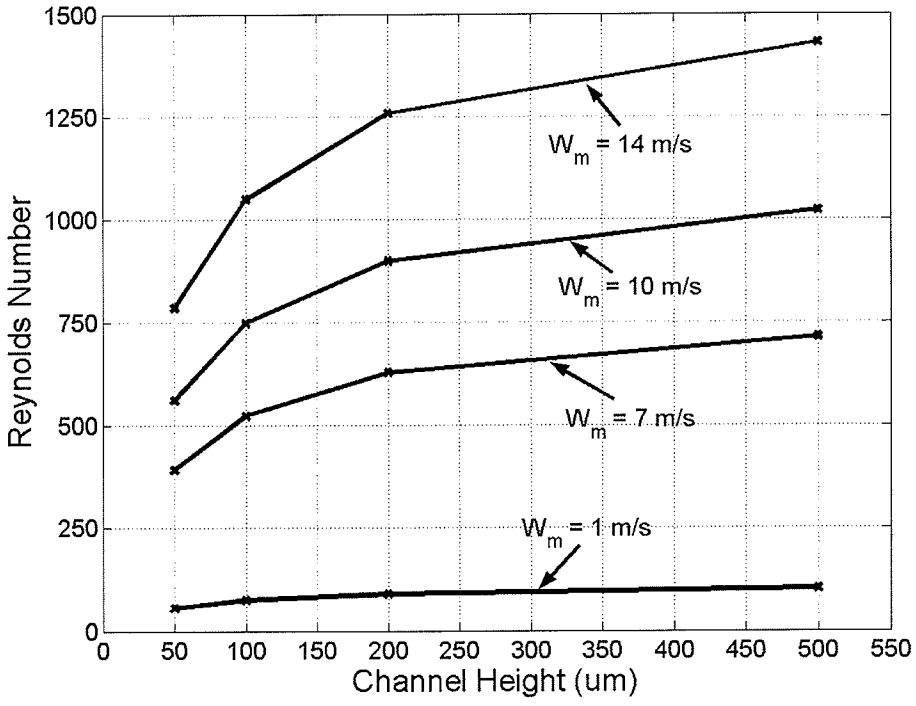

Figure 3-3. Reynolds numbers for four channel heights at different mean fluid velocities.

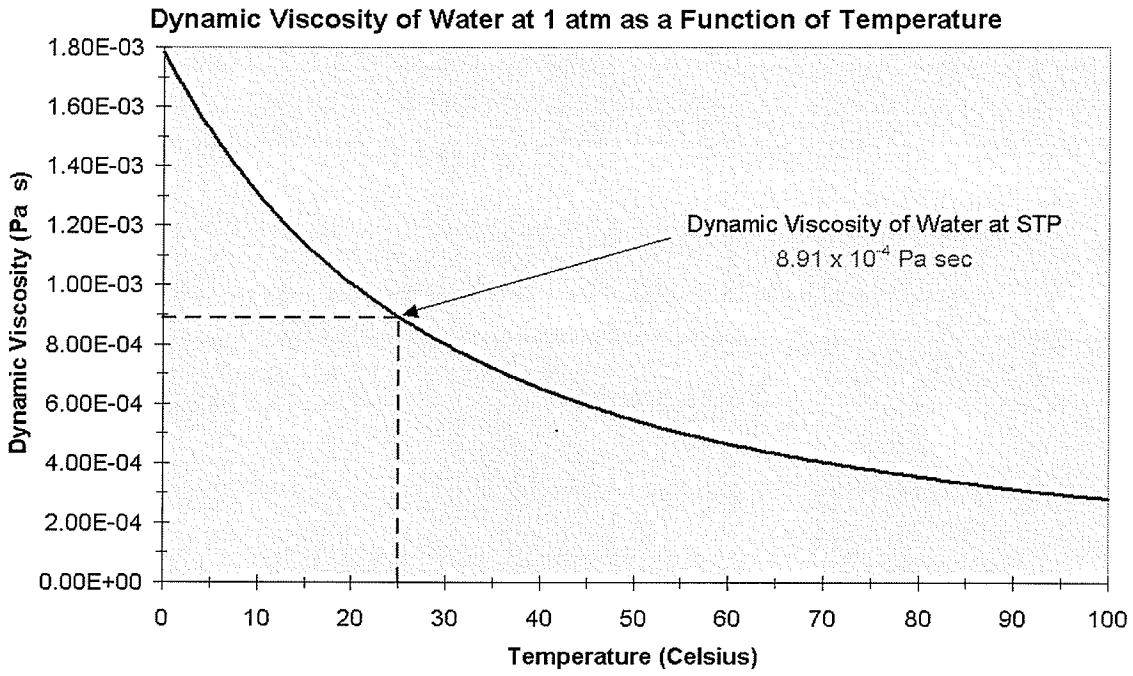

Figure 3-4. Dynamic viscosity of water versus temperature.

3.3. Simulation Tool and Settings

For FEM simulations COMSOL Multiphysics software v.3.5 64bit was used. The simulations were done using "Heat Transfer" and "Fluid Dynamics" packages of this software. All simulations were in steady state (stationary mode) or transient (Time dependent mode) and three dimensional. Since the simulations used two physics and were performed in 3D, they consumed a large amount of memory and time, depending on the mesh size.

COMSOL has several solvers that can be used for this type of multiphysics simulations. Its default solver, UMFPack, needs a lot of memory and is slow. It is good for small and 2D simulations. For example with UMFPack, for a 3D microchannel simulation with about 400,000 mesh elements, the occupied memory easily reaches 32

Giga Bytes and it takes 5-6 hours to solve on the STOUT server in the ECE department of the University of Manitoba. It is a SUN computer (SunFire V880) with four 1 GHz processors and 32 GB of RAM. Of course due to users' restrictions this simulation was able to use only one of these processors at a time.

In version 3.5 of COMSOL software, there is a solver named "Pardiso" which is much faster and more memory efficient than UMFPack, but its required memory size depends on the mesh size. This solver exists only on the PC version of COMSOL, and since the PC memories are limited (to 2-8 GB), Pardiso cannot be used for large simulations with very large number of elements.

The other solver is "BiCGStab" which uses a fixed amount of memory. Using this simulator, 3D microchannels with 800,000 mesh elements were simulated using a PC with Intel Duo Core 2.66 GHz processor and 8 GB ram in 6-7 hours.

The set of equations used for these simulations (eqs. 3-1 to 3-6) were inherently nonlinear. Due to dependence of parameters like K, C, ρ and μ of the solid and the fluid on temperature, they become more nonlinear and solving them becomes more difficult. In COMSOL these parameters can be considered dependent on temperature and solve the equations using a nonlinear solver, but this would make the simulation too complicated and it would take a much longer a time to solve it. In the simulations of this thesis, in order to a little simplify the simulation process, fixed numerical values were assigned to each of these parameters and the linear solver was used for simulation. This is legitimate, because other than the water viscosity, the change in other parameters is very small over the temperature range of 20 – 100 °C. The assigned simulation parameter values (which are for room temperature condition) were:

Thermal conductances:	K_S (Cu) = 400 W/mK
	K_S (Si) = 163 W/mK
	K_S (Ni) = 90.7 W/mK
	K_f (Water) = 0.6069 W/mK
Thermal capacitances:	C_S (Cu) = 385 J/kgK
	C_S (Si) = 703 J/kgK
	C_S (Ni) = 445 J/kgK
	C_f (Water) = 4181.7 J/kgK
Density	ρ_s (Cu) = 8700 kg/m^3
	ρ_s (Si) = 2330 kg/m^3
	ρ_s (Ni) = 8900 kg/m^3
	ρ_f (Water) = 997 kg/m^3
Viscosity	μ_f (Water) = 0.0008899 Pa×sec

The other possible way is to leave the parameters with their temperature dependent expressions, but using the linear solver. Anyway, the linear solver is used for solving the set of nonlinear equations. According to the COMSOL User's Guide [54], "If a model is nonlinear, the linear solver solves the corresponding *linearized* model, evaluated at a specified *linearization point*. The result is equivalent to adding a Newton correction to the linearization point. Repeated linear solutions, updating the linearization each time, is therefore equivalent to an undamped Newton method and will often converge rapidly towards the solution of the nonlinear model." This method also was tried. Simulation in this way takes a little longer, but the result is the same as using the

fixed values for the parameters. The reason is that variation of above mentioned parameters with temperature is very small.

COMSOL v. 3.5a is a user-friendly software, but it has some deficiencies compared to ANSYS. The most important problems are that the user doesn't have enough control on mesh generation. For example, in 3D the mesh elements have only a tetrahedral shape, and cannot be hexagonal which is more suggested to be used for some geometry. Their density in different directions for different parts of the object (x, y, z) cannot be adjusted separately. Most of the other problems are related to post processing. The generated data cannot be processed in many different or complicated ways, as it is possible in ANSYS. For example in ANSYS there are much more options and more flexibility in post-processing the resulting data. More specific example, in COMSOL the resulting data can only be integrated on a whole boundary or physical object, but in ANSYS the data on any arbitrary piece of boundary or object can be integrated.

Chapter 4

Validation and Verification of the Simulations

It is very important to make sure that the simulation results are correct and valid. There are several ways to verify the simulations.

- It should be shown that the simulations are grid independent. In the other words, the number of the elements of the mesh that is used for simulations has to be sufficiently high that the simulation result doesn't change with the number of the elements of the mesh.
- It should be shown that the simulation result is logical and is consistent with the basic physical rules, for example conservation of mass and energy.
- The simulation results should be compared with theoretical and analytical results if available.
- Compare the results with the results of other simulation software.
- Compare the simulation results with the experimental results.

4.1. Mesh Independence Test

For grid dependency investigations a basic microfluidic heatsink structure with the following properties was simulated:

- Solid material: Copper
- $H_C = W_C = S = H_T = H_B = 50$ μm
- $L = 1$ cm
- $w_m = 7$ m/s
- $q'' = 100$ W/cm^2

For these conditions, the Reynolds number is calculated (based on eq. 3-9) as $Re = 392$ and the pressure drop ΔP is calculated based on formula 4-1:

$$\Delta P = \frac{4fL}{D_h}\frac{\rho_f w_m^{\,2}}{2} \tag{4-1}$$

For the above conditions $D_h = 50$ μm and f×Re is a constant value which depends on the aspect ratio of the channel (H_C / W_C). For the aspect ratio of H_C / W_C = 1, the value of f×Re is obtained from [55] as f×Re = 14.23. Hence the friction factor, f, can be calculated:

$$f = \frac{14.23}{Re} = \frac{14.23}{392} = 0.0363$$

and so: $\Delta P = \frac{4fL}{D_h}\frac{\rho_f w_m^{\,2}}{2} = \frac{4\times 0.0363\times 0.01}{50\times 10^{-6}}\times\frac{1000\times 7^2}{2} = 7.1148\times 10^5\,\text{Pa}$

First the simulation was performed with a mesh that was almost uniform in the whole structure, using BiCGStab solver and with Lagrange Quadratic terms. The results

of this test can be observed in Table 4-1. ΔT is the difference between the temperatures of the hottest point on the surface of the heatsink and the input fluid.

Table 4-1. Uniform Mesh in the solid and channel,

Solver: BiCGStab, Lagrange Quadratic terms

Number of Elements	ΔT (K)	ΔP	Difference of ΔP from the analytical value
5,674	14.25	18.2×10^5 Pa	-155.8 %
19,587	17.732	8.04×10^5 Pa	-13 %
58,619	18.198	7.17×10^5 Pa	-0.77 %
181,674	18.873	6.95×10^5 Pa	2.3 %
281,213	18.952	6.71×10^5 Pa	5.7 %
549,534	19.154	6.79×10^5 Pa	4.6 %

As observed, the value of the pressure drop result is converging and is getting close to the analytical value, but not close enough which is less than 1 %. The mesh was changed so that a higher portion of the elements are located in the channel. For this purpose the maximum sizes of elements on the channel boundary and inside its body were set to a small value. The results of the simulation with this type of meshing can be observed in Table 4-2. For the highest number of elements in this table (708,986), the mesh is generated with these parameters:

Maximum element size in the channel: 10 μm

Maximum element size in the solid: 25 μm

Maximum element size on the heat input boundary: 15 μm

Maximum element size on the channel boundary: 10 μm

Element growth rate from the channel boundary: 1.2

Maximum element size on the boundary at the beginning of the channel: 5 μm

Element growth rate from the channel boundary at the beginning of the channel: 1.1

Maximum element size at the channel inlet: 1 μm

Table 4-2. Mesh mostly concentrated in the channel,

Solver: BiCGStab, Lagrange Quadratic terms

Number of Elements	ΔT (K)	ΔP	Difference of ΔP from the analytical value
164,317	18.97	7.01×10^5 Pa	1.5 %
229,688	19.16	6.93×10^5 Pa	2.6 %
287,666	19.20	6.86×10^5 Pa	3.6 %
343,095	19.19	6.96×10^5 Pa	2.2 %
404,205	19.09	7.05×10^5 Pa	0.9 %
541,085	19.08	7.08×10^5 Pa	0.49 %
708,986	19.23	7.09×10^5 Pa	0.35 %

As observed, with mesh sizes over 400,000 elements the value of pressure drop gets much closer to the analytical value ($\Delta P = 7.1148 \times 10^5$ Pa) and the difference between the simulated and analytical values for the highest number of elements is less than 1 %, which is very good. The simulations with this type of mesh were repeated with the following conditions and the results were exactly the same:

- Solver: BiCGStab, Lagrange Linear terms.
- Solver: BiCGStab, Lagrange Cubic terms.
- Solver: UMFPack, Lagrange Quadratic terms.

Since the simulation in the fluid section used two physics (heat transfer and fluid dynamics), compared to simulation in the solid section that uses only one physics (heat transfer), it was expected that to achieve a higher accuracy the mesh has to be mostly

concentrated in the regions of high gradient which are the channel boundaries and the beginning of the channel.

Unfortunately the maximum temperature of the solid surface cannot be found analytically. But from Tables 4-1 and 4-2 it can be said that for this simulated structure the converged value for ΔT is about 19 °C. Figure 4-1 shows the variation of the thermal resistance versus the number of elements. As observed, the overall thermal resistance changes by less than 1.3 %, as the number of elements changes from 164,317 to 708,986. All results presented in this thesis were generated using the number of elements in this range.

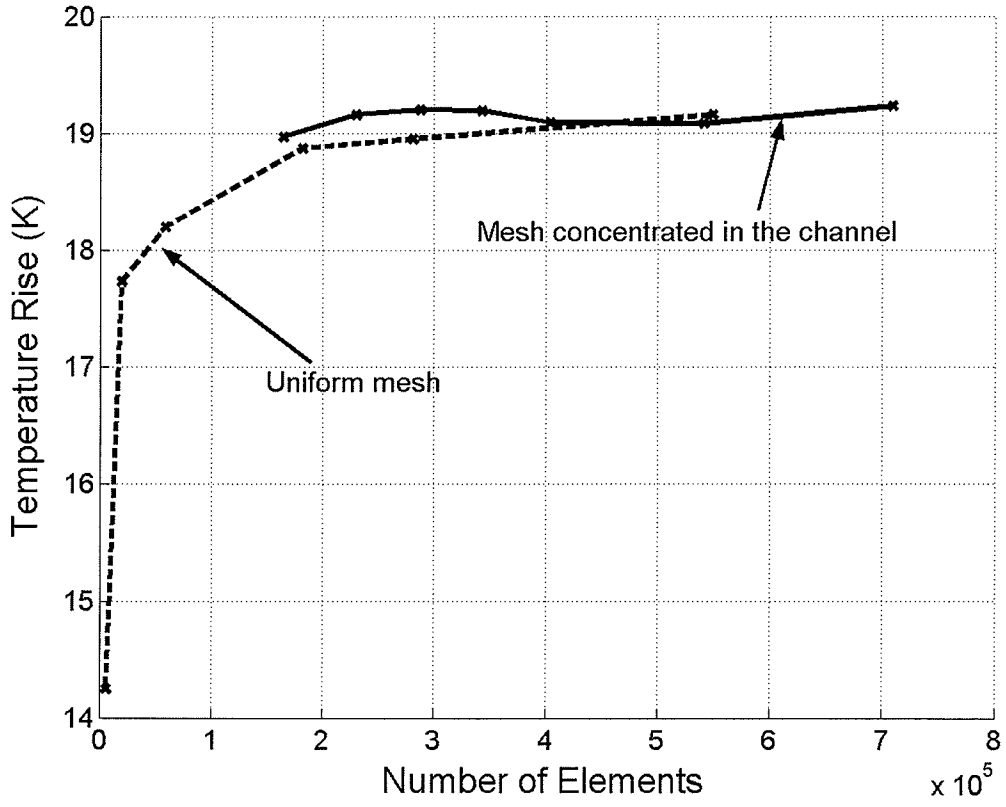

Figure 4-1. Heat Resistance versus the number of mesh elements for the structure described at the beginning of this section.

4.2. Physical Consistency Test

Correct convergence of the FEM simulation solutions in this work can be determined from their fit to the heat transfer formula for the heat sink structure given by eq. 4-2. This relation says that the rate of heat gained by the fluid is equal to the rate of input heat through the hot boundary (Conservation of energy) [52].

$$q'' \times (WL) = \dot{m} C_f \Delta T_f \tag{4-2}$$

where ΔT_f is the total temperature difference between the incoming water and the outgoing water, and $\dot{m}$ is the mass flow rate. In all cases the solution convergence was found to be within ± 0.2%.

4.3. Comparing with Analytical Results

The first comparison with the analytical results was performed and is reported in section 4.1 where the simulated pressure drop was compared with the analytically calculated value.

The other way for examining the validity of the simulation result is to draw a parameter named Nusselt number and comparing it with the predicted value in the literature. The Nusselt number is a parameter that is related to the heat absorption capability of a fluid flowing in a channel from its solid boundaries. It depends on several parameters such as channel size and aspect ratio, type of fluid and its mean velocity and temperature.

In order to do this Nusselt number comparison, a simple microchannel was considered with a channel height and width of 50 μm and a fixed temperature of 360 K at

the boundaries. The fluid mean velocity was 1 m/s and the temperature of the incoming water was 300 K. A parameter named bulk temperature is defined as [52]:

$$T_b(z) = \frac{\int_A wTdA}{\int_A wdA} \tag{4-3}$$

Bulk temperature is the average temperature of the fluid passing through a plane A perpendicular to the direction of fluid flow along z axis. Of course this temperature is weighted with the mass flow rate. The bulk temperature, T_b, is a function of z and these integrations are done over the flat surfaces inside the channel and perpendicular to the fluid flow. The bulk temperature calculated for the above mentioned simulation is sketched in Figure 4-2. This figure shows that the bulk temperature of the fluid increases gradually from 300 K and reaches the wall temperature (360 K).

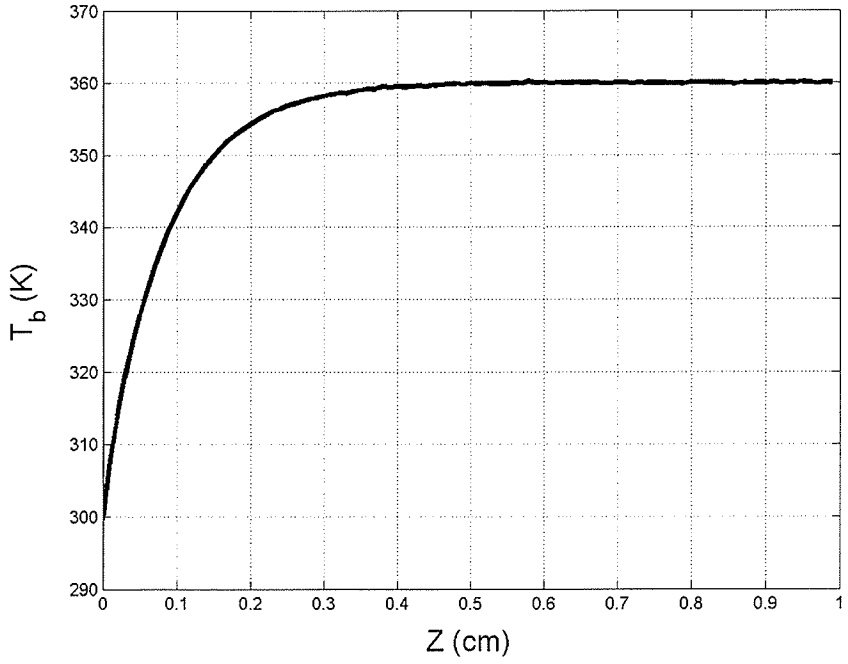

Figure 4-2. The bulk temperature along a microchannel for which $W_C = H_C = 50$ μm, and $w_m = 1$m/s. The incoming water temperature is 300 K and the walls temperature is 360 K.

Using the calculated T_b the value of the axially local heat transfer coefficient (h_{local}) can be found which is defined based on the bulk temperature as [56]:

$$h_{local} = \frac{q''_{local}}{T_W - T_b} \tag{4-4}$$

where q''_{local} is the local heat flux at the wall (unit: W/m^2) and T_W is the wall temperature (360 K). In COMSOL the value of q''_{local} for each boundary can be observed using the post-processing menu. This function is averaged over the perimeter of the channel [56]:

$$\bar{h}_z = \frac{\int h_{local}\, dC}{\int_C dC} \tag{4-5}$$

The local Nusselt number is defined based on $\bar{h}_z$ as [56]:

$$Nu_{z,T} = \frac{\bar{h}_z D_h}{k_f} \tag{4-6}$$

Nusselt numbers in the literature are sketched versus a dimensionless coordinate called z* which is defined as [56]:

$$z^* = \frac{z}{D_h \,\mathrm{Re}\,\mathrm{Pr}} \tag{4-7}$$

This is done in order to make the sketched Nusselt number curve independent from the Reynolds number and the sizes of the channel. It depends only on the aspect ratio of the channel. The Prandtl number (Pr) is a parameter of the flowing fluid defined as [52]:

$$\mathrm{Pr} = \frac{\mu_f C_f}{k_f} \tag{4-8}$$

The value of $Nu_{z,T}$ for the above mentioned simulated channel is sketched in Figure 4-3. As observed, $Nu_{z,T}$ reaches approximately 3.8 at the end of the channel. Figure 4-3 shows the data calculated by Lyczkowski et al presented in [55]. According to this numerically calculated data, the value of $Nu_{z,T}$ has to reach to about 3 (exactly 2.975). There are two main reasons for this difference. First reason is that the handbook's data is for a large value of Reynolds Number (above 1500), while the Reynolds number of the simulated structure is only 56. This causes the difference between the curves at their beginnings. The second reason is that the sections along the simulated structure are not small enough to obtain a precise result. This causes the difference at the end of the curves.

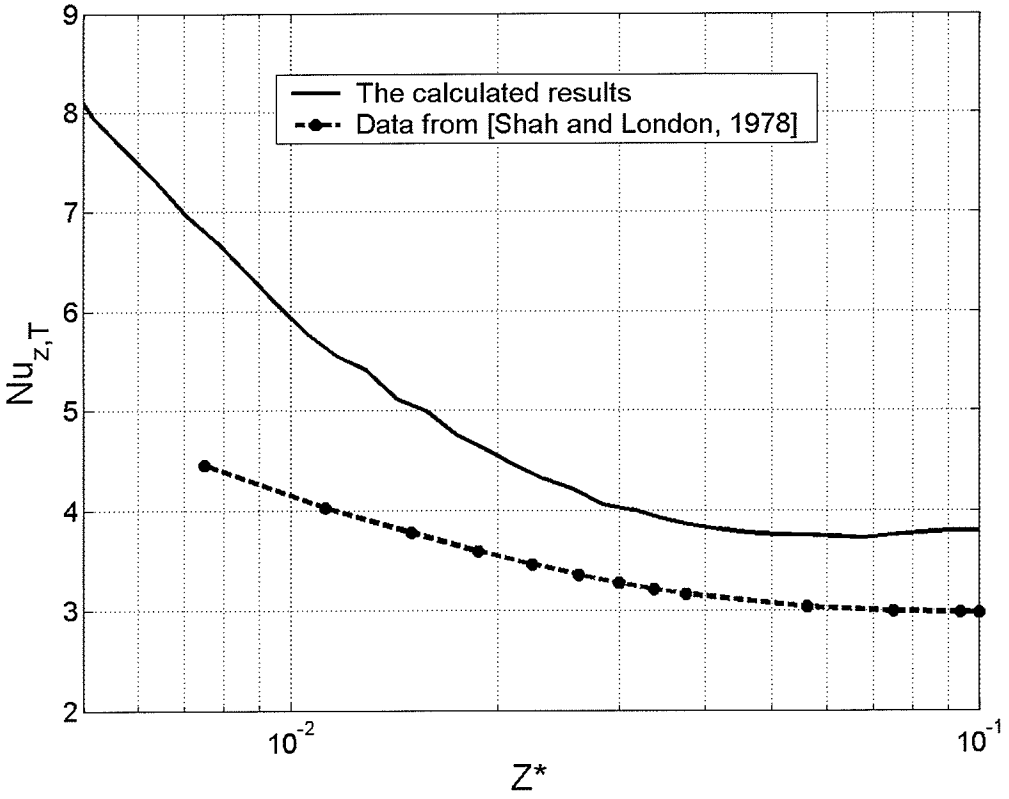

Figure 4-3. $Nu_{z,T}$ for a microchannel with W_C = H_C = 50 μm, and w_m = 1m/s. The incoming water temperature is 300 K and the walls temperature is 360 K.

4.4. Comparing the Results of COMSOL Simulations with the Results of Another Software

Another way to verify the results of simulation with a program is to repeat the simulations with another program and compare the results. For this purpose the COMSOL results were compared with the results of simulation with ANSYS CFX.

Figure 4-4 shows the fluid velocity across the microchannel simulated with two softwares. It is the same structure simulated in section 4-1. The mean velocity for both of these cases is set to be 7 m/s. With integrating the velocity across the channel using these

curves an calculating the mean velocity, the following values are obtained which are very close to the set value:

w_m (COMSOL) = 6.972 m/s

w_m (ANSYS CFX) = 7.024 m/s

The pressure drop that ANSYS gives is 7. 103 × 10^5 Pa which is very close to the analytical result. The velocity profiles are very close to each other. As the pressure drop values were verified in section 4-1, and the fluid velocity here, the COMSOL simulation results for fluid dynamics is in agreement with ANSYS.

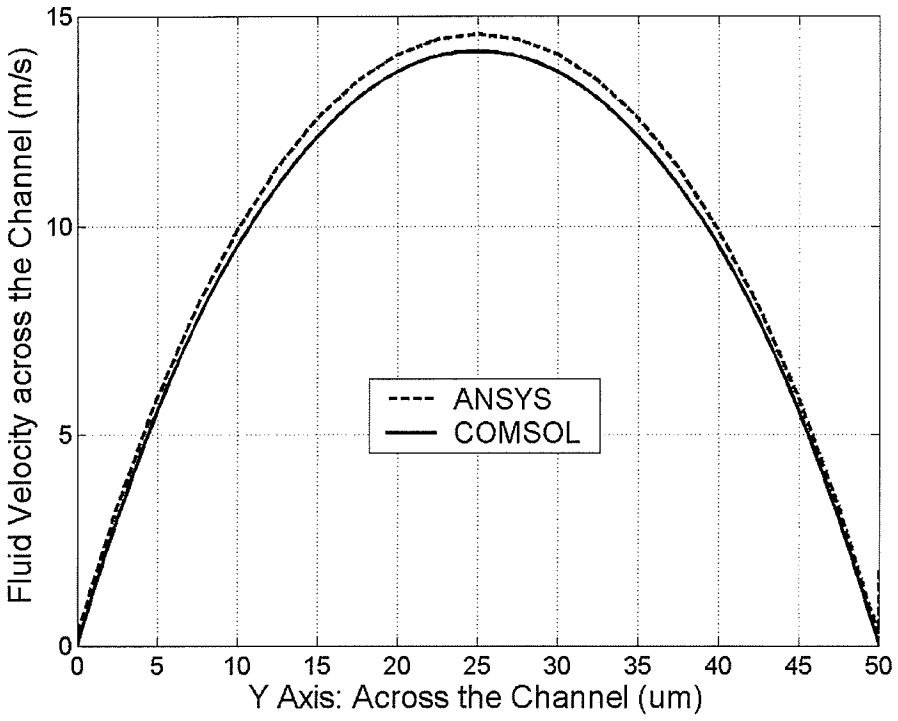

Figure 4-4. Fluid velocity across the microchannel simulated with COMSOL and ANSYS CFX.

Some of the simulations performed with COMSOL were repeated with ANSYS CFX and the results are shown in Table 4-3. The temperature difference between the hottest point of the surface and the base temperature (300 K) for each simulated case is shown in this table.

Table 4-3. Temperature rise for different materials and fluid mean velocities simulated using two different softwares. Mesh number of elements is greater than 500,000 for all cases. Other conditions are $H_C = W_C = S = H_T = H_B = 50$ μm, $L = 1$ cm, $q'' = 100$ W/cm^2.

		Temperature Rise (K)		
	V_m	**2 m/s**	**7 m/s**	**14 m/s**
ANSYS CFX Results	**Cu**	57.0	24.3	17.0
	Si	58.4	25.0	17.5
	Ni	59.1	25.5	18.0
COMSOL Results	**Cu**	52.1	19.3	12.1
	Si	53.0	19.7	12.5
	Ni	53.7	20.2	12.9
Results Difference	**Cu**	4.9	5.0	4.9
	Si	5.4	5.3	5.0
	Ni	5.4	5.3	5.1

As observed there is a ~5 °C difference between the results of two softwares. However, the trend is the same for both and they change in the same way. To investigate more about this difference; temperature across the microfluidic heatsink (from its bottom

to top) is sketched in Figure 4-5. From this figure it is inferred that there could be a problem with the simulated heat transfer at the fluid-solid interface for at least one of the softwares. Figure 4-4 shows that there is almost no difference between the fluid velocity profiles across the channel simulated by two softwares. Therefore the temperature difference should be due to heat transfer simulation.

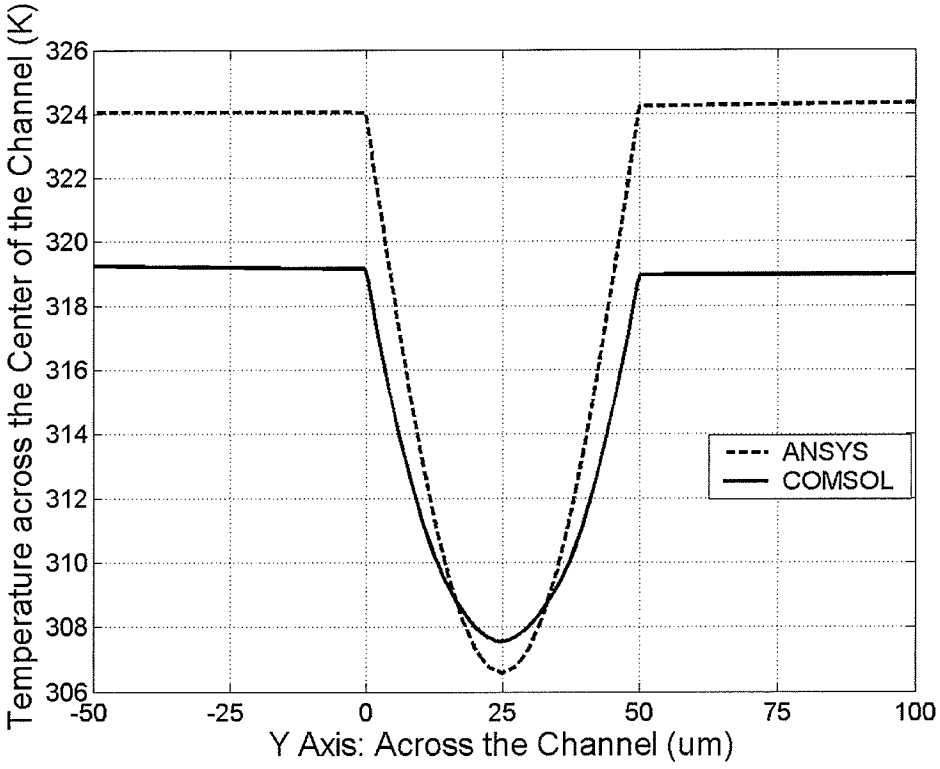

Figure 4-5. Temperature across (bottom to top) the microfluidic heatsink simulated with COMSOL and ANSYS CFX.

In ANSYS CFX and COMSOL, solid and fluid sections were meshed separately. In ANSYS CFX hexagonal elements were used, while for COMSOL simulations, tetrahedral elements were used. This can be a reason for difference in heat transfer simulations. Heat transfer in two simple solid structures was simulated using the two

softwares and the results were exactly the same. This showed that when using only the heat transfer physics, there is no problem, but when combining two physics (heat transfer and fluid dynamics) the temperature results don't match.

From comparison of the simulation results of two softwares it is concluded that while their absolute temperature results don't agree, the trend of their variation with change in the simulation parameters is in agreement and can be relied on.

4.5. Comparing with Experimental Results

The experimental results in the literature for heat sinks with rectangular microchannels at these dimensions are available mostly for silicon and not for copper or nickel. The important problem in comparison of simulation results with experimental results in the literature is that in almost all papers that report experimental results, some parameters are missing. For example in [25] the values of H_T and H_B have not been mentioned.

Two experimental structures for silicon microfluidic heatsinks found in the literature were simulated by COMSOL. These two cases have been used for comparison of results by several other authors too. The results can be seen in Table 4-4. The simulation results are in very good agreement with the experimental results, especially with the results of Kawano et al [25].

The small observed differences can be due to some parameters like the thermal resistance of the contact between heat sink and heat source (which has not been taken into account in the simulations of this work), as well as other experimental factors.

Table 4-4: Comparison of some simulations presented in this thesis with experimental results for fabricated microchannel devices presented in the literature.

Reference	Material	L (mm)	W (mm)	W_C (μm)	H_C (μm)	S (μm)	H_T (μm)	Fluid Flow Rate (cm^3/s)	Mean Fluid Velocity (m/s)	Thermal Resistance (Kcm^2/W)	ΔP (bar)
This work	Si	15	15	57	180	43	100	2.5	2.215	0.23	0.94
Kawano et al [25]	Si	15	15	57	180	43	-	2.5	2.215	0.2	1
This work	Si	10	10	50	302	50	100	8.6	5.695	0.066	2.45
Tuckerman and Pease [8]	Si	10	10	50	302	50	100	8.6	5.695	0.09	2.07

Chapter 5

Investigation of Heat Exchangers with Uniform Heat Source

5.1. Basic Simulations

The first investigation undertaken was to investigate and compare heat sink performance as a function of material thermal conductivity for copper, silicon, and nickel. The following simulation parameters were considered $H_B = H_T = 50$ μm, $S = 50$ μm, $W_C = 50$ μm, and $T_{in} = 300$ K. The input heat flux applied at the top of the structure was $q'' = 100$ W/cm^2. Four channel heights were considered, $H_C = 50$ μm, 100 μm, 200 μm, and 500 μm, and three mean fluid velocities were simulated, $w_m = 2$ m/s, 7 m/s, and 14 m/s. Figure 5-1 shows the results of these simulations. All of these values for the physical parameters are selected due to their consistency with the structure of IC's and prior investigations of microfluidic heat sinks [8, 15, 17, 18, 19, 20, 25, 27, 56, & 57].

Figure 5-1 is the case with channel height $H_C = 50$ μm. The temperature along the 1 cm top surface (Point A in Figure 3-2) of the heat sink is plotted for the three materials and mean fluid velocities. The results show minimal difference, in terms of surface temperature, as a function of heat sink material. Mean fluid velocity is a significant parameter, however, with a large surface temperature reduction obtained by increasing mean fluid velocity from 2 m/s to 7 m/s. This is expected as a larger mean fluid velocity

results in increased cooling fluid's mass flow rate passing through the heat sink. However, it is observed that the surface temperature of the heat sink does not reduce in proportion to the increase in fluid's mass flow rate. For example, at the mid point of the heat sink z = 0.5 cm, it is observed that at w_m = 2 m/s the temperature increase is ~30 °C, while when w_m is increased 3.5 times to 7 m/s, the temperature increase is ~12 °C, an improvement in performance of only 2.5 times. Increasing the velocity further to 14 m/s provides further temperature reduction; however, the percentage benefit is again reduced. The corresponding fluid's mass flow rate through the heat sink is 15 mL/min for w_m = 1 m/s, 105 mL/min for w_m = 7 m/s, and 210 mL/min for w_m = 14 m/s.

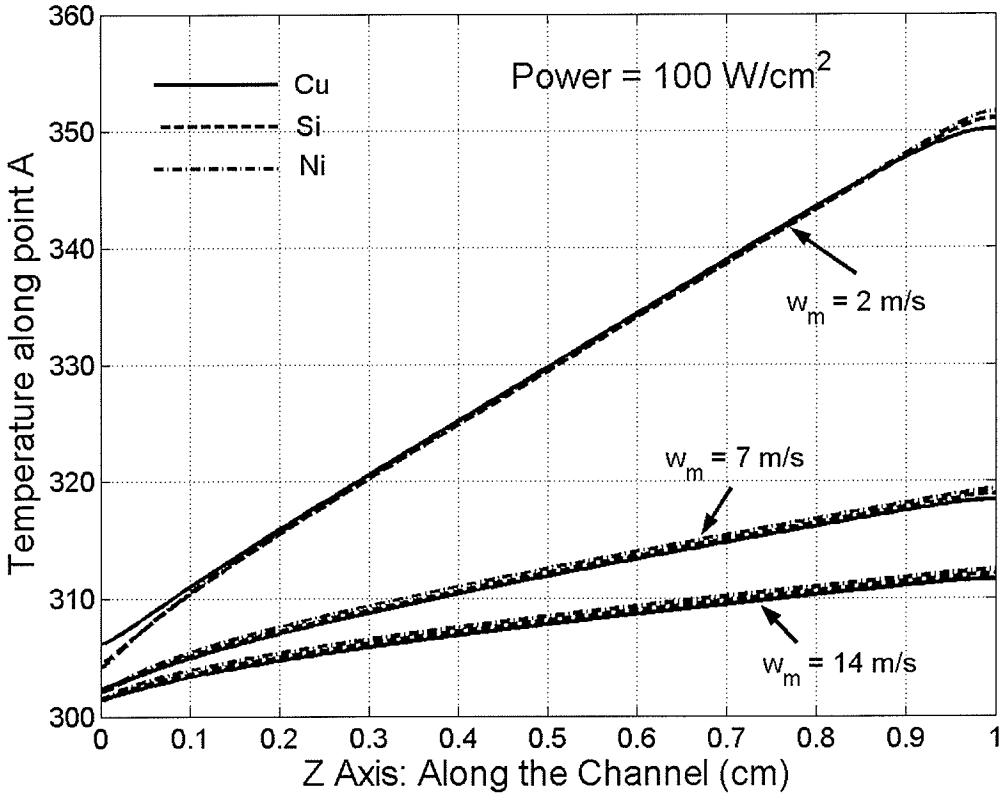

Figure 5-1. Temperature along the 1 cm heat sink surface with W_C = 50 μm and H_C = 50 μm as a function of channel height, heat sink material, and mean fluid velocity.

Figure 5-2 illustrates the fluid temperature inside the copper microchannels, from their center to the right side, for the cases simulated in Figure 5-1. This data is from the end of the 1 cm long microchannel, where the fluid has reached its maximum temperature. As observed, for w_m = 2 m/s, the temperature of water is between about 342 K at the middle of the channel to 350 K at the boundary. However, for w_m = 7 m/s, the temperature is changing from 307 K to 318 K from middle to boundary. The temperature difference here is considerably higher, especially in percentage. Again, it is observed that for w_m = 14 m/s there is a large temperature difference (from 302 K and 312 K), and also

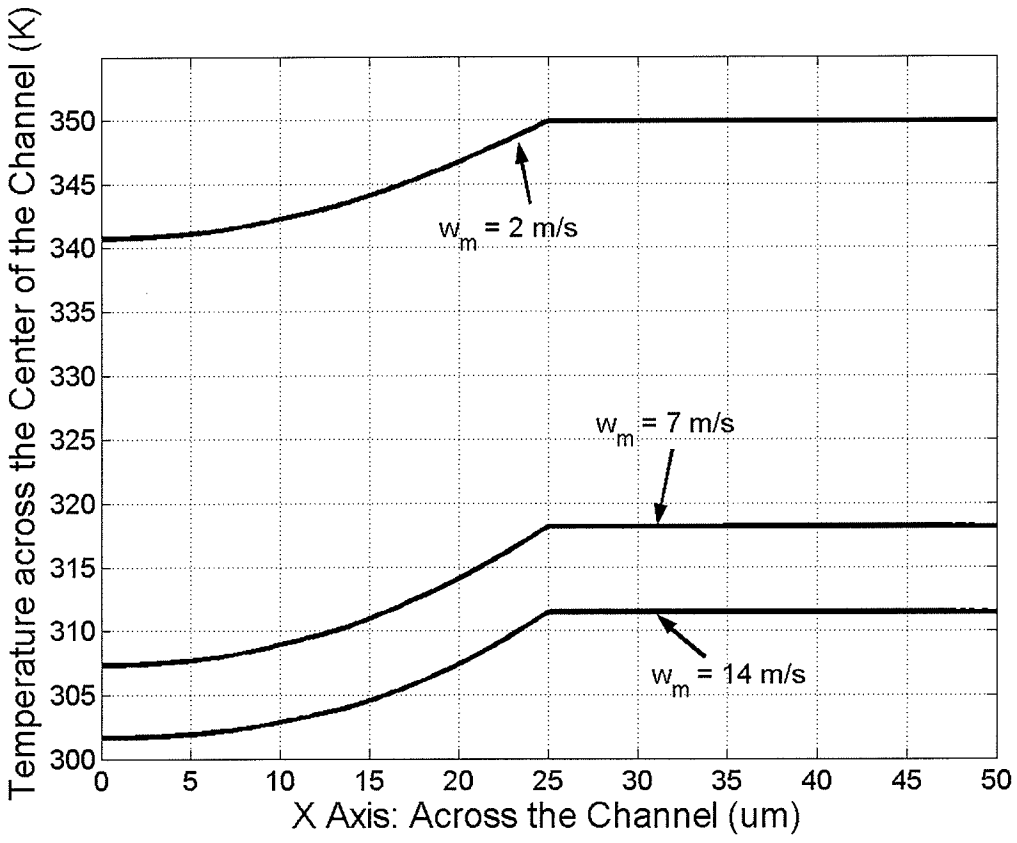

Figure 5-2. Temperature profiles of the fluid within the microchannel at the end of the copper heat sink of Figure 5-1.

that the center of fluid has only increased 2 degrees in temperature. This analysis is significant as it illustrates that with higher velocities, poorer utilization of the fluid's total thermal mass occurs. This explains why the surface temperature of the heat sink in the simulation of Figure 5-1 does not reduce in proportion to the increase in mean fluid velocity.

The inefficient utilization of fluid thermal mass with increasing fluid velocities does, however, indicate that there is opportunity to improve heat sink performance at high fluid velocities if the flow regime in the channel were turbulent. Furthermore, Figure 5-2 shows that this performance improvement would be increasingly significant with increasing the mean fluid velocity.

It is also observed in Figure 5-1 that at the start of the channel ($z < 0.1\text{cm}$) there is a change in the slope of the temperature along the channel length. This is also visible at the end of the channel, but to a lesser degree. This behavior is in agreement with classic heat transfer theory, and is due to the boundary condition for all sidewalls being thermally isolated, and so the derivative of temperature is zero at both ends of the channel.

The simulations of Figure 5-3(a) have the channel height increased to $H_C = 100$ μm. Comparing Figures 5-1 and 5-3(a), it is seen that doubling the channel height results in a reduction in heat sink temperature rise approximately in proportion to the increase in channel height. This relationship is expected since the doubling of the heat sink channel height, results in a doubling in the amount of fluid's mass flow rate. Figure 5-3(a) also shows that heat sink material again plays a minimal role in temperature.

The simulations of Figure 5-3(b) are for the channel height increased to H_C = 200 μm, representing a microfluidic channel height to width ratio of 4:1. Now more benefit is observed in using higher thermal conductivity materials for the heat sink, as a percentage of heat sink temperature rise. The simulations of Figure 5-3(c) have H_C = 500 μm, representing a microfluidic channel height to width ratio of 10:1. The benefit to using higher thermal conductivity materials is now significant, with the difference in temperature rise between nickel and copper heat sinks for fluid velocities of 14 m/s nearly a factor of two. For a given material, however, it should be noted that the reduction of heat sink temperature rise is no longer in proportion with the increase in channel height, with the benefit dropping with progressively increasing channel height. This illustrates that while fluid's mass flow rate is increasing with increasing channel height, the ability of lower thermal conductivity materials to distribute heat becomes a factor for large channel height ratios.

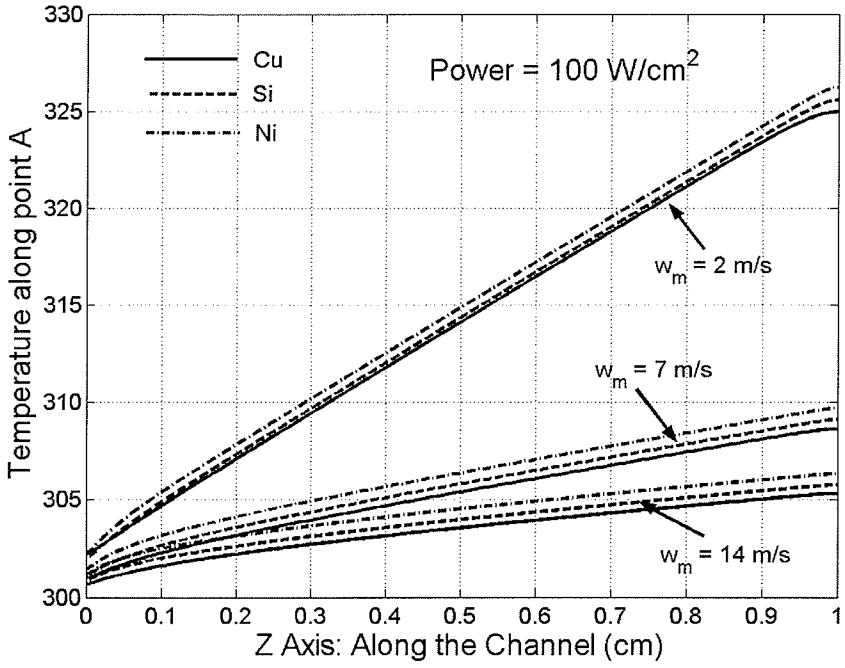
Cu
Si
Ni
Power = 100 W/cm2
wm = 2 m/s
wm = 7 m/s
wm = 14 m/s
Temperature along point A
Z Axis: Along the Channel (cm)
330
325
320
315
310
305
300
0
0.1
0.2
0.3
0.4
0.5
0.6
0.7
0.8
0.9
1

(a)

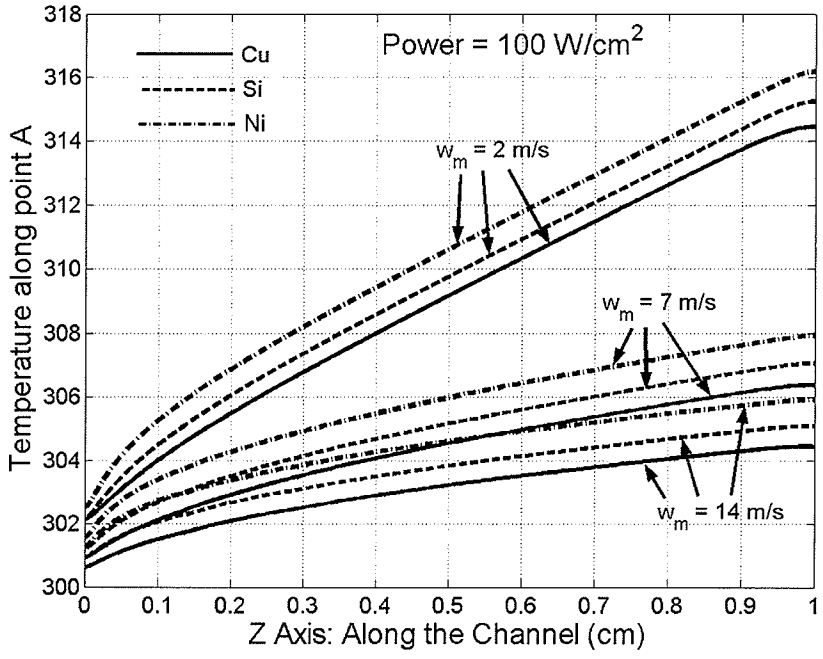
Cu
Si
Ni
Power = 100 W/cm2
wm = 2 m/s
wm = 7 m/s
wm = 14 m/s
Temperature along point A
Z Axis: Along the Channel (cm)
318
316
314
312
310
308
306
304
302
300
0
0.1
0.2
0.3
0.4
0.5
0.6
0.7
0.8
0.9
1

(b)

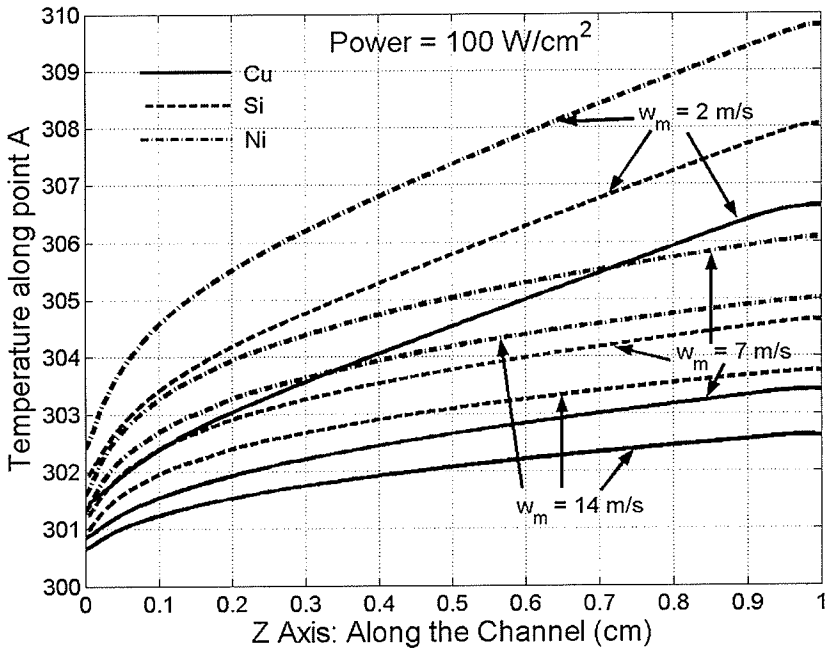

(c)

Figure 5-3. Temperature along the 1 cm heat sink surface with W_C = 50 μm as a function of channel height, heat sink material, and mean fluid velocity. (a) Result for H_C = 100 μm. (b) Result for H_C = 200 μm. (c) Result for H_C = 500 μm.

5.2. The Effect of Channel Height and Fluid Mean Velocity on Thermal Resistance of the Heatsink

The conclusions found from the analysis of Figures 5-1 and 5-3, regarding the effect of thermal conductivity and microfluidic channel height to width ratio on heat sink performance can be more clearly seen upon consideration of the thermal resistance of the structure. Figure 5-4 shows the calculated thermal resistance for the simulated structures. The overall thermal resistance was calculated using equation (5-1):

$$\text{Thermal Resistance} = \frac{T_{\max} - T_{in}}{q''} \tag{5-1}$$

where T_{max} is the temperature of the hottest point of the heat sink, which is normally the point at the end of the flow and on the surface adjacent to the heat source, and T_{in} is the inlet temperature of the water, which was fixed at 300 K.

Figure 5-4(a) shows the Thermal Resistance as a function of mean fluid velocity, channel height, and heat sink material. Figure 5-4(b) is the same data, plotted with channel height as the x-axis.

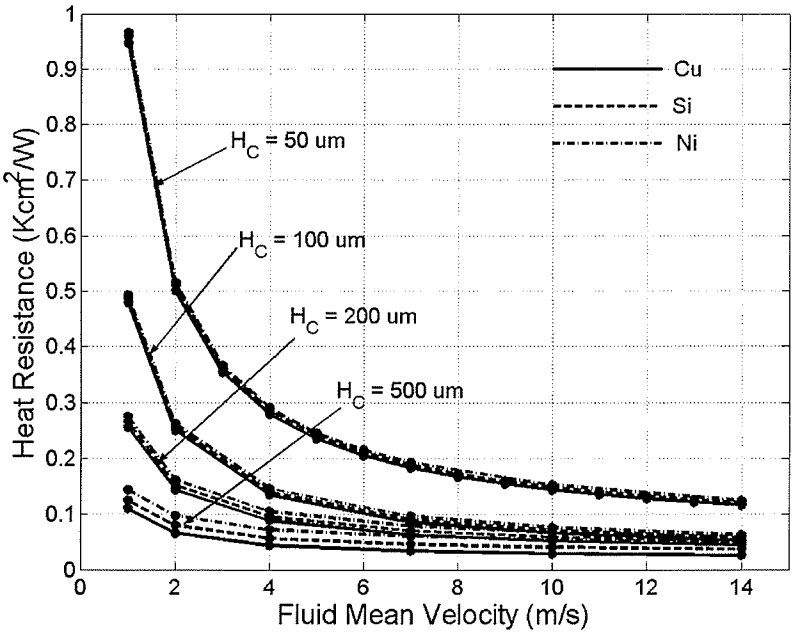

(a)

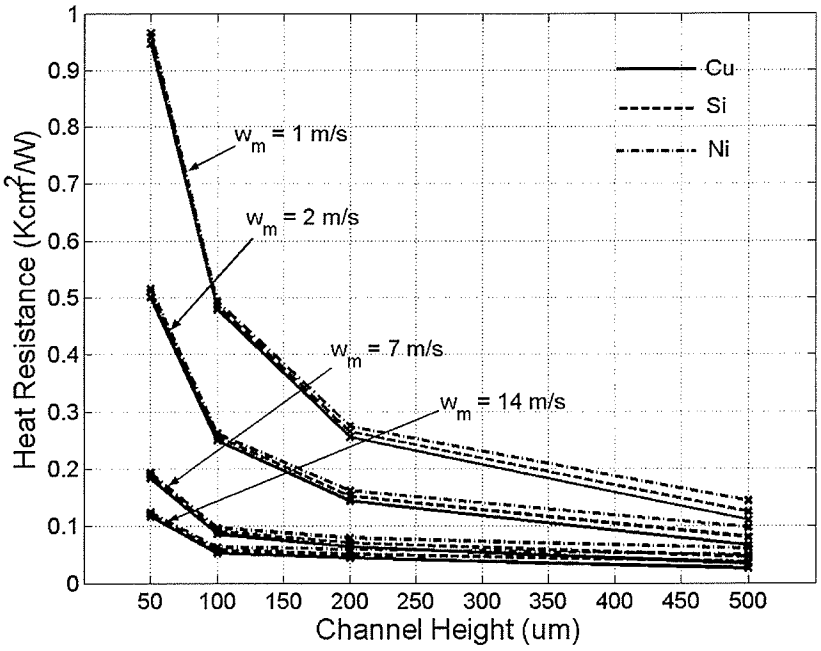

(b)

Figure 5-4. Overall thermal resistance for the simulated cases of Figures 4 and 6 versus mean fluid velocity (w_m), channel height (H), and the solid material. (a) Mean fluid velocity as the x-axis. (b) Channel height as the x-axis.

The percentage reduction in Thermal Resistance of nickel and silicon compared to copper is shown in Figure 5-5, as function of channel height and mean fluid velocity.

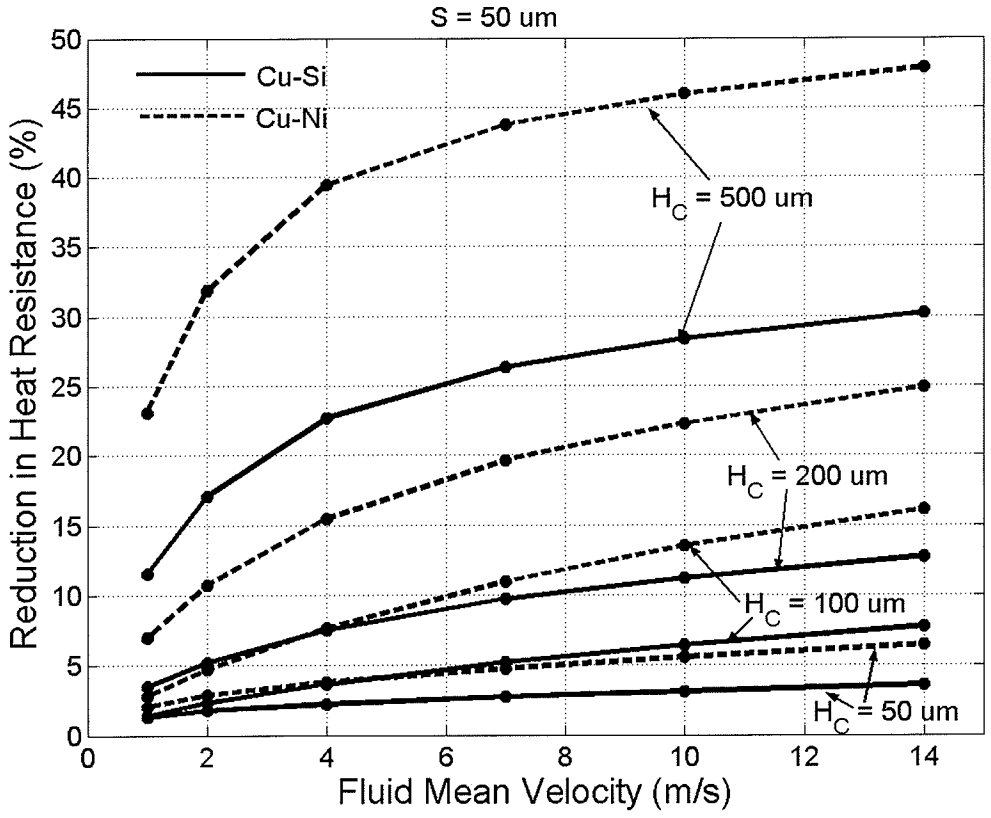

Figure 5-5. Percentage change in the overall thermal resistance of the heat sink due to changing the material from Si or Ni to Cu, as a function of mean fluid velocity and channel height.

These figures clearly show that the benefit of high thermal conductivity materials is minimal for small channel height to width ratios, and only becomes significant with larger channel height to width ratio. Also observed, is that the benefit of increasing channel height to width ratio is more significant at greater fluid velocities. For the channel height of 200 μm, using copper instead of nickel, improves the thermal resistance by 25 % for a 14 m/s mean fluid velocity. This increase is close to 50 % for the channel height of 500 μm.

Figures 5-4(a) and 5-4(b) clearly illustrate the benefit of higher fluid velocities. An important observation, however, is that the reduction in Thermal Resistance is not constantly proportional to the increase in mean fluid velocity (and associated fluid's mass flow rate). Rapid reduction of Thermal Resistance is seen when increasing mean fluid velocities from 1 m/s, while the reduction to Thermal Resistance is minimal when increasing velocities beyond, for example, 10 m/s. The cause of this is the inefficient utilization of total fluid thermal mass, as was illustrated in Figure 5-2.

5.3. The Effect of Channel Separation Distance on Thermal Resistance of the Heatsink

The other parameter that was investigated was the separation distance (S) between the fluid filled channels. The channel separation distance affects the heat sink performance in two ways. First, a larger separation distance means that fewer fluid cooling channels are present. This would be expected to reduce the Thermal Resistance performance in proportion to the loss in fluid mass, for situations where heat is efficiently transferred to the total mass of the fluid. Referring to Figure 5-2, it is seen that at the low average fluid velocity of 2 m/s the fluid exiting the channel has a nearly uniform temperature, while at the higher average fluid velocities of 7 m/s and 14 m/s heat transferred to the fluid is not uniformly distributed. Accordingly, it would be expected that the Thermal Resistance of the heat sink would increase in similar proportion to the loss of fluid mass for low fluid average velocities around 2 m/s, and less so for higher fluid velocities. Figure 5-6 is a simulation of thermal resistance as a function of channel separation distance S for a heat sink containing fluid channels with W_C = 50 μm and H_C =

50 μm. For a given mean fluid velocity, the cases where S changes from 50 μm to 150 μm are compared, representing a reduction in fluid cooling mass by a factor of 2. At the low average fluid velocities of 1 m/s and 2 m/s as expected a near doubling in Thermal Resistance is observed, while the increase is reduced at the high fluid velocities of 7 m/s and 14 m/s. This is in agreement with the above discussion.

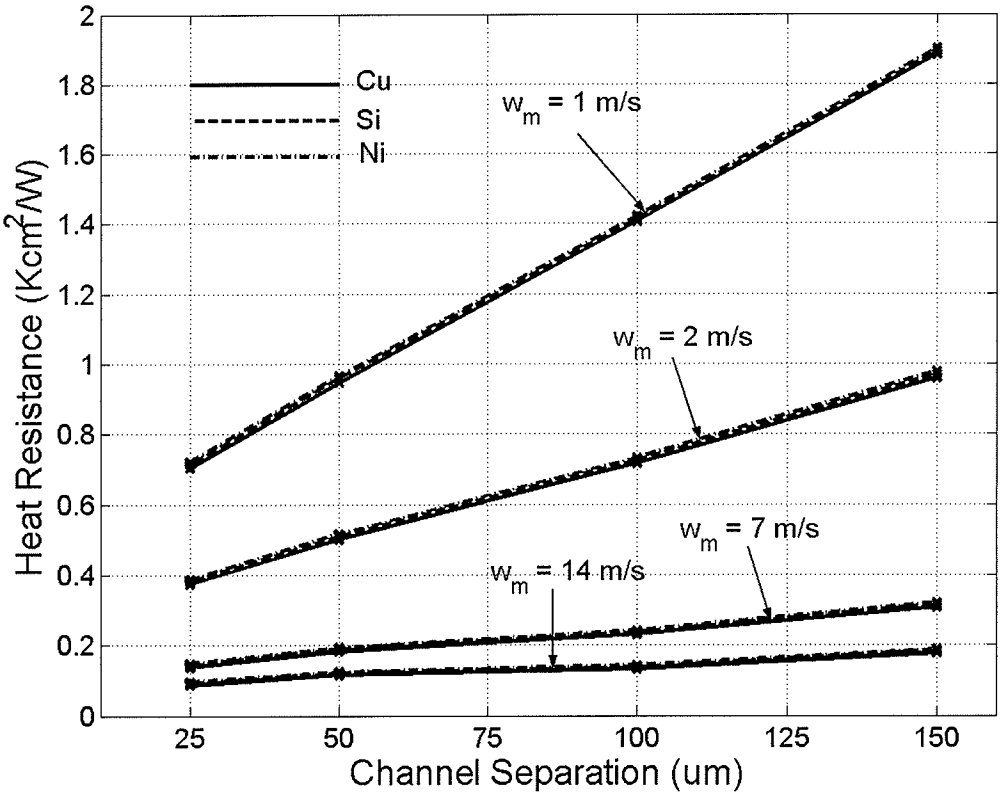

Figure 5-6. Thermal Resistance versus channel separation distance (S) for a 1 cm heat sink with H_C = 50 μm and W_C = 50 μm. Four sets of data are shown for four different mean fluid velocities.

5.4. Discussion

The above discussions of Figures 5-1 to 5-6 show that improved performance can be gained by increasing total fluid's mass flow rate. The following discussion compares the benefits of increasing fluid's mass flow rate by increasing channel height versus increasing the number of microchannels via a reduction in channel edge-to-edge separation. Table 5-1 shows the simulated temperature difference (T_{max} - T_{in}) between the maximum temperature on the surface of the heatsink and the entering cooling fluid, as a function of fluid's mass flow rate, channel height, and channel spacing. Channel width is W_C = 50 μm for all simulated cases. Investigating the results of Table 5-1 shows two prominent conclusions. First, for a given fluid's mass flow rate passing through the microchannel heat sink, decreased channel separation provides superior benefit over increased channel height. It should be noted, however, that this result is due in part to the fact that each additional microchannel adds additional top and bottom surfaces, which augment conductive heat transfer into the fluid.

Second, examination of the simulations for w_m = 14 m/s reveals some limitations to performance. It should be recalled that at this fluid average velocity, heat transferred to the fluid is not uniformly distributed throughout the total mass of the fluid. Compare the results for the cases were H_C = 200 μm. It is important that the following comparison be done for identical H, since fluid velocity distribution within a microchannel depends on H_C and W_C ratio. For S = 100 μm and H_C = 200 μm (the ratio of H_C to S equals 2:1), nickel achieves no further improvement in performance when increasing H_C to 500 μm. In fact simulations imply the performance degrades. For S = 50 μm (the ratio of H_C to S equals 4:1), silicon achieves no further improvement in performance when increasing H_C

to 500 μm. For S = 25 μm (the ratio of H_C to S equals 8:1), copper appears to reach a performance limit. It is worth noting that these performance limits as a function of H_C to S ratio, appear to be in proportion to the respective differences in thermal conductivity of nickel, silicon, and copper. This implies that narrow microchannel separation S restricts the ability for heat to transfer to the sidewalls of microchannels when H_C to S ratio becomes appropriately significant.

Table 5-1. Simulated temperature difference (T_{max} - T_{in}) between the maximum temperature on the surface of the heatsink and the entering cooling fluid, as a function of fluid's mass flow rate, channel height, and channel spacing. Channel width is W_C = 50 μm.

		H_C = 50 μm		H_C = 100 μm		H_C = 200 μm		H_C = 500 μm	
	w_m	2 m/s	14 m/s	2 m/s	14 m/s	2 m/s	14 m/s	2 m/s	14 m/s
S = 25 μm	**Cu**	39.4°C	9.2°C	21.3°C	5.8°C	11.5°C	3.7°C	8.1°C	3.6°C
	Si	40.1°C	9.6°C	22.0°C	6.4°C	12.5°C	4.5°C	10.1°C	5.2°C
	Ni	40.8°C	10.1°C	22.8°C	7.1°C	13.8°C	5.6°C	12.5°C	6.9°C
	Fluid Mass Flow Rate (ml/sec)	0.67	4.67	1.33	9.33	2.67	18.7	6.67	46.7
S = 100 μm	**Cu**	-	17.9°C	41.5°C	11.1°C	21.8°C	6.5°C	14.1°C	5.4°C
	Si	-	18.4°C	42.5°C	11.5°C	22.7°C	7.1°C	15.4°C	6.4°C
	Ni	-	18.8°C	43.2°C	12.1°C	23.5°C	7.8°C	16.9°C	7.8°C
	Fluid Mass Flow Rate (ml/sec)	-	2.33	0.67	4.67	1.33	9.33	3.33	23.3
S = 50 μm	**Cu**	52.1°C	12.1°C	28.0°C	7.5°C	14.9°C	4.5°C	9.9°C	4.0°C
	Si	53.0°C	12.5°C	28.8°C	8.0°C	15.7°C	5.2°C	11.4°C	5.3°C
	Ni	53.7°C	12.9°C	29.5°C	8.6°C	16.7°C	6.1°C	13.2°C	6.8°C
	Fluid Mass Flow Rate (ml/sec)	0.5	3.5	1	7	2	14	5	35
S = 150 μm	**Cu**	-	23.7°C	54.9°C	14.6°C	28.7°C	8.4°C	13.7°C	5.2°C
	Si	-	24.3°C	56.2°C	15.1°C	29.7°C	9.1°C	14.8°C	6.0°C
	Ni	-	24.9°C	57.1°C	15.7°C	30.7°C	9.8°C	16.0°C	7.0°C
	Fluid Mass Flow Rate (ml/sec)	-	1.75	0.5	3.5	1	7	2.5	17.5

Chapter 6

Investigation of Heat Exchangers with Discrete Heat Source

6.1. Simulations

The second investigation undertaken in this work was to study heat sink performance when a non-uniform heat source is present on the heat sink surface. Simulations were performed for heat sinks with microchannels of height H_C = 50 μm, width W_C = 50 μm, and edge-to-edge separating distance S = 50 μm. The heat flux at the top surface was q'' = 100 W/cm^2, except in the center region of length L_{Hot}. In this hot spot region, two cases were considered. For L_{Hot} = 1 mm, the input heat was 1000 W/cm^2, and for L_{Hot} = 3 mm, it was 500 W/cm^2. The thickness of metal below the microchannels was H_B = 50 μm, while the thickness of metal above the microchannels H_T was varied.

There are two mechanisms affecting the peak temperature of the hot spot. One is simply the heat conduction length through the solid material between the heat source and the fluid, which increases with increasing top layer thickness (H_T). This mechanism will work to increase the peak temperature in the hot spot region with increasing thickness H_T. The second mechanism is axial conduction. This mechanism decreases the peak temperature as H_T increases, and its influence depends on the thermal conductivity of the solid material. These two mechanisms compete with each other, and depending on the conditions, one of them may dominate. The following simulation results illustrate this

concept, and reveal the design parameters that obtain the minimum peak temperature at the hot spot.

In order to illustrate temperature *(T)* along the structure and its variation with different parameters, such as the mean axial fluid velocity (w_m), the solid material, and the heat sink top surface thickness (H_T), the temperature rise above ambient along the channel at position "A" of Figure 3-2 is plotted. In all cases inlet fluid temperature is equal to the ambient temperature (300K). Figure 6-1 shows the temperature rise on the surface of the heat sink along the channel (point A) for a 1 mm hot spot centered at z = 0.5. This temperature has been sketched for two velocities, w_m = 7 in Figure 6-1(a) and 14 m/s in Figure 6-1(b). For a better comparison, the surface temperature rise of the copper heat sink for the basic situation (without hot spot) is sketched as a dotted line.

As seen in Figures 6-1 and 6-2, in all cases, the maximum temperature happens almost at the end of the hot spot region (z = 0.55 cm for the 1 mm hot spot, and z = 0.65 cm for the 3 mm hot spot). It is also observed that by changing the solid material from nickel to copper, heat is spread more and the axial conduction is larger, because copper has a better heat conductance. Hence the peak temperature decreases.

In order to investigate the effect of the top layer thickness (H_T), simulations were done for different values of the top layer thickness. In Figure 6-2, the temperature rise on the surface of the copper heat sink along the channel (position A) with a hot spot centered at z = 0.5 cm was simulated for a few values of top layer thicknesses (H_T) and mean fluid velocity of w_m = 14 m/s. In Figures 6-1 and 6-2 it is observed that the hot spot considerably increases the temperature at the hot spot location and downstream from it.

The hot spot peak temperature depends a lot on the heat sink material, but the surface temperature after the hot spot does not.

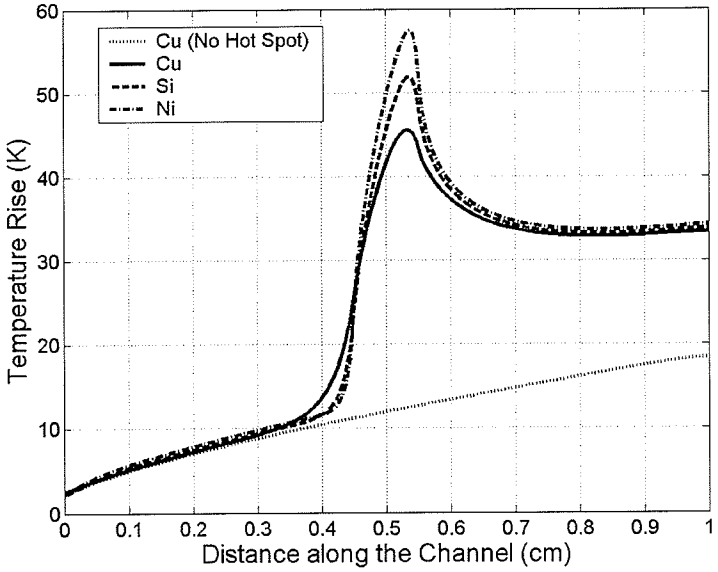

(a)

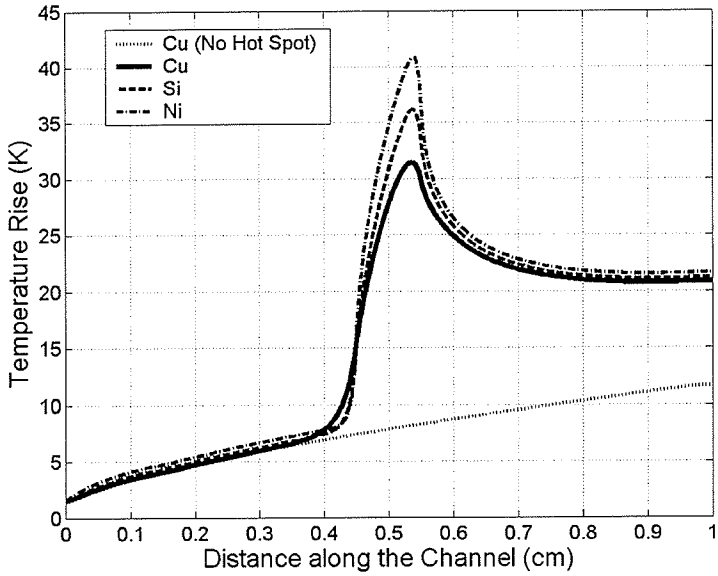

(b)

Figure 6-1. Temperature rise of the surface of the heat sink along the channel with a 1 mm wide hot spot centered at $z = 0.5$ cm for $H_C = 50$ μm, $W_C = 50$ μm, and $H_T = 50$ μm. (a) $w_m = 7$ m/s. (b) $w_m = 14$ m/s.

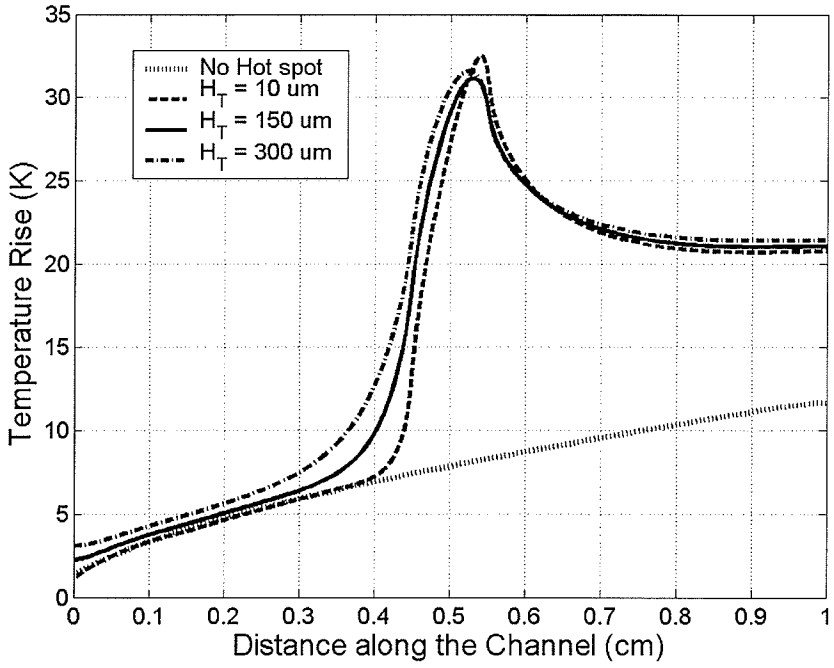

(a)

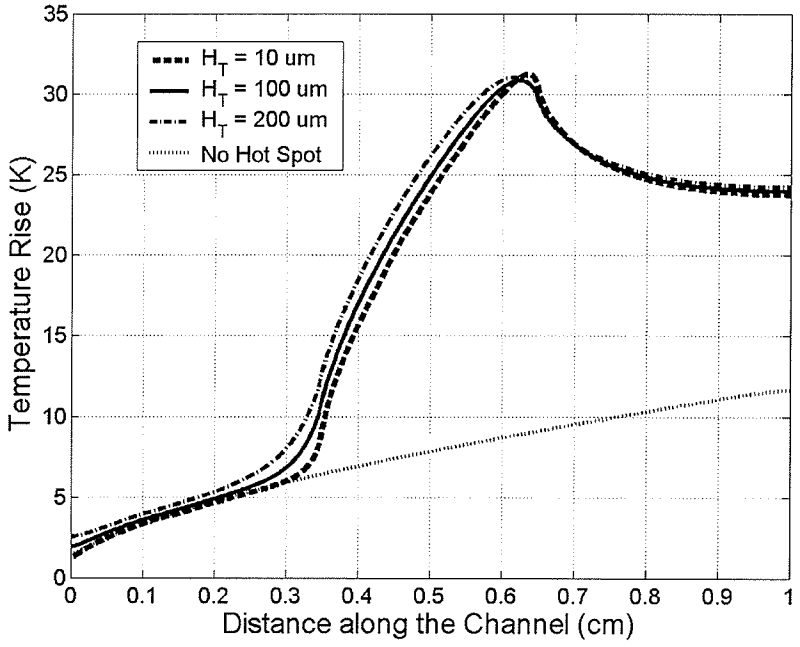

(b)

Figure 6-2. Temperature rise of the surface of the copper heat sink along the channel with a hot spot centered at z = 0.5 cm for H_C = 50 μm, W_C = 50 μm, w_m = 14 m/s, and three thicknesses. (a) 1 mm hot spot (b) 3 mm hot spot.

6.2. Discussion

Figure 6-3 plots the peak temperature rise as a function of heat sink material and H_T for a 1 mm hot spot, for w_m = 7 m/s and 14 m/s. These results are summarized in Table 6-1. In each column of this table, the minimum temperature rise for each material is written with bold font. Several points are observed in this table:

1. Although the mean axial fluid velocity doubles from 7 to 14 m/s, the peak temperature rise is not reduced by the same factor. This result is consistent with the earlier analysis for the uniform heat source condition.

2. The effect of the thickness (H_T) of the solid layer on top of the channels can be easily observed. As observed, silicon and nickel achieve the lowest peak temperature at around 50 μm and 25 μm, and performance reduces noticeably for H_T = 150 μm.

3. For copper, the minimum peak temperature depends on the mean fluid velocity. For w_m = 7 m/s, the optimum H_T is 300 μm, while for w_m = 14 m/s, the optimum H_T is 150 μm.

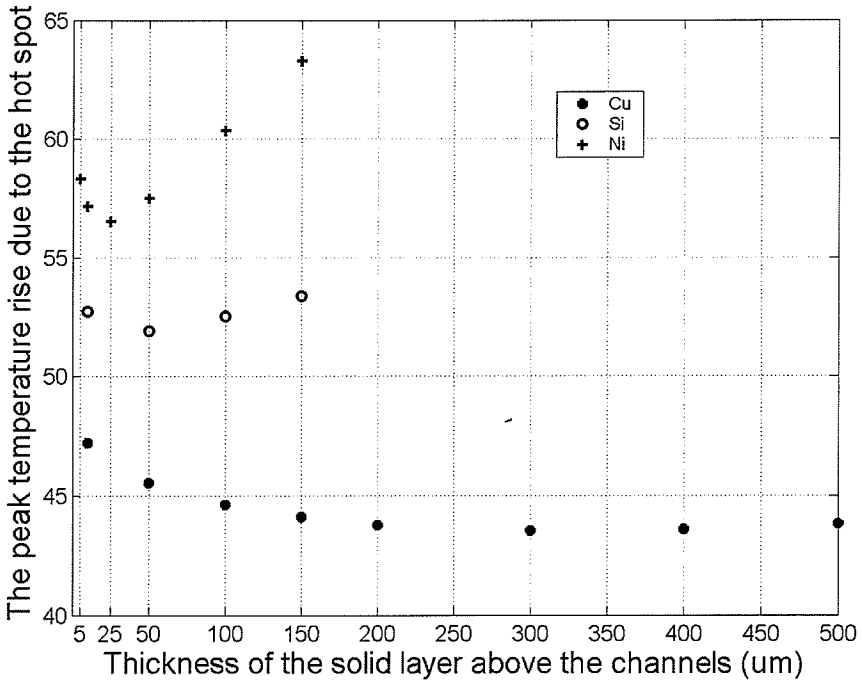

(a)

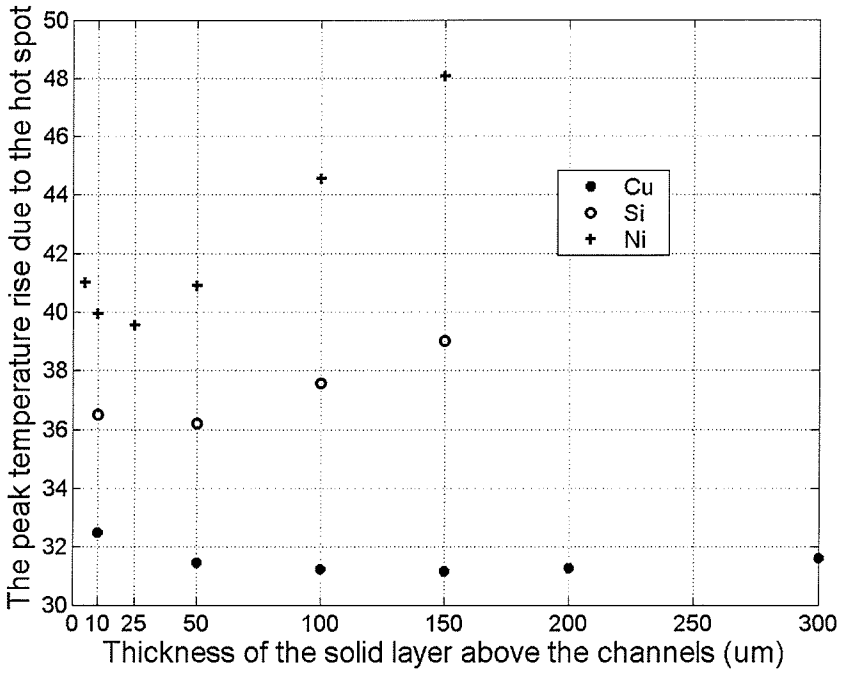

(b)

Figure 6-3. Peak temperature rise due to the 1 mm wide hot spot as a function of material and H_T. (a) w_m = 7 m/s. (b) w_m = 14 m/s.

Table 6-1. The peak temperature rise due to 1 mm and 3 mm the hot spots for the different simulated cases.

		Hot Spot Width = 1 mm		**Hot Spot Width = 3 mm**	
	w_m **(m/s)**	**7**	**14**	**7**	**14**
H_T**= 5 μm**	**Ni**	58.34	41.01	-	-
H_T**= 10 μm**	**Cu**	47.21	32.49	-	31.23
	Si	52.74	36.51	-	-
	Ni	57.16	39.94	-	-
H_T**= 25 μm**	**Ni**	**56.53**	**39.55**	-	-
H_T**= 50 μm**	**Cu**	45.53	31.46	-	30.92
	Si	**51.91**	**36.21**	-	-
	Ni	57.53	40.91	-	-
H_T**= 100 μm**	**Cu**	44.63	31.23	-	**30.87**
	Si	52.55	37.58	-	-
	Ni	60.36	44.56	-	-
H_T**= 150 μm**	**Cu**	44.11	**31.17**	-	30.95
	Si	53.40	39.01	-	-
	Ni	63.27	48.09	-	-
H_T**= 200 μm**	**Cu**	43.78	31.28	-	31.05
H_T**= 300 μm**	**Cu**	**43.54**	31.61	-	-
H_T**= 400 μm**	**Cu**	43.59	-	-	-
H_T**= 500 μm**	**Cu**	43.82	-	-	-

The thickness H_T where the minimum peak temperature occurs is when the competing effects of heat spreading (due to material thermal conductivity) and heat conduction length (due to increasing top layer thickness H_T) are optimum. These two mechanisms are related to two heat flow passages for the input heat. As shown in Figure

6-4, part of the thermal energy after entering the heatsink goes directly toward the fluid in the channel, and part of that goes in the axial direction (upstream or downstream). The amount of hot spot heat which goes upstream is higher than the one going downstream, because temperature in the upstream is lower.

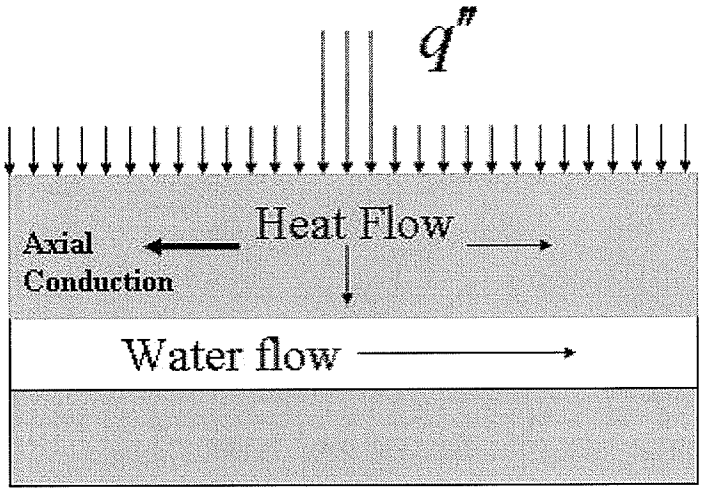

Figure 6-4. Two directions of flow of the input heat from the hot spot.

6.3. Summary

It is interesting to observe from Figure 6-3 and Table 6-1 that the optimum thickness for the top solid layer (H_T) for each heat sink varies approximately in proportion with the ratios of the thermal conductivities of the heatsink solid material. For the simulated cases, nickel and silicon achieve the lowest peak temperature at around 25 μm and 50 μm respectively, and performance reduces noticeably for H_T = 150 μm. This is in proportion to their thermal conductances which are 90, 148 and 401 W/mK. This can be explained by considering the flow of the input heat from the hot spot in two directions.

Chapter 7

Investigation of Transient Behavior of Microfluidic Heatsinks

7-1. Importance of Transient Study of Microfluidic Heatsinks

In this chapter the transient behavior of a microfluidic heatsink is studied and discussed. Transient response of the heat sink is important, because heat input in an IC is often dynamic with transient nature. It is the transient characteristics and behavior of the heat sink that determines the surface temperature profile in response to the dynamic heat input. It is important to know how fast the heatsink temperature changes with the variation of the input heat. It is also important to characterize how this transient behavior depends on the structure of the heatsink and the thermal conductivity and thermal capacity of the materials of the heatsink.

7-2. Simulated Cases

For transient analysis, a time dependent term is added to equations 3-5b and 3-6:

$$k_s\left(\frac{\partial^2 T}{\partial x^2}+\frac{\partial^2 T}{\partial y^2}+\frac{\partial^2 T}{\partial z^2}\right)=\rho_s C_s\frac{\partial T}{\partial t} \tag{7-1}$$

$$\frac{\partial T}{\partial t}+u\frac{\partial T}{\partial x}+v\frac{\partial T}{\partial y}+w\frac{\partial T}{\partial z}=\frac{k_f}{\rho_f C_f}\left(\frac{\partial^2 T}{\partial x^2}+\frac{\partial^2 T}{\partial y^2}+\frac{\partial^2 T}{\partial z^2}\right) \qquad (7\text{-}2)$$

The UMFPACK solver in COMSOL was used for these simulations, since the BiCGStab solver was too slow for time dependent simulation. All simulations were in transient state (Time dependent mode) and three dimensional. Since the simulations used two physics (heat transfer and fluid dynamics), they consumed a large amount of memory and time. This is one of the reasons why very few papers can be found on transient study of microfluidic heatsinks.

7-3. Transient Response of the Heatsink to Uniform Heat Step Function

First, a uniform heat step function, u(t) = 100 W/cm^2, was applied to a copper heatsink surface with $H_C = H_T = H_B = W_C = S = 50$ μm and $w_m = 7$ m/s. The result of the transient simulation is sketched in Figure 7-1. As observed, it takes less than 30 ms for the temperature of the hottest point of the surface, which is at the end of the heatsink, to reach the steady state value.

In Figure 7-2 a first order exponential curve is fitted (with the method that is going to be explained) to this transient simulation. We can see that the simulation transient response is close to that of the fitted first order exponential curve.

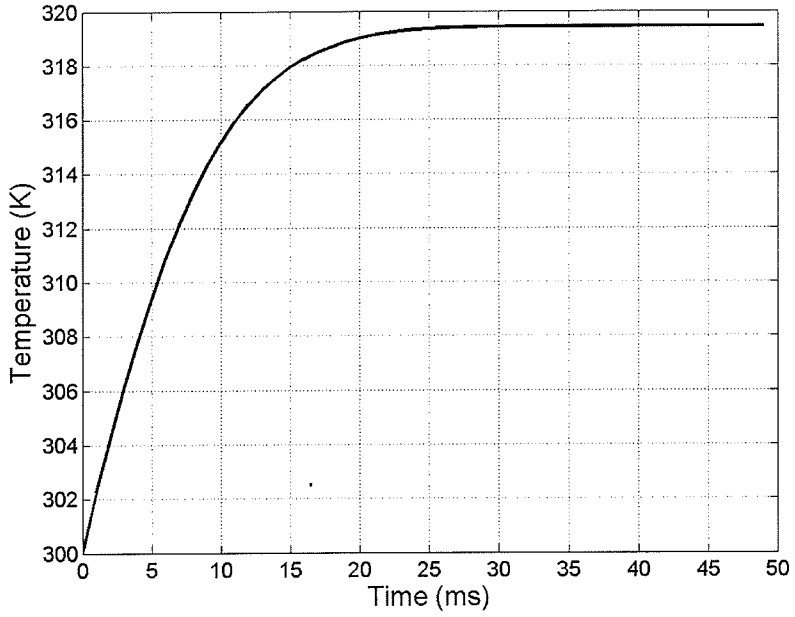

Figure 7-1. Temperature of the hottest point of the heatsink, which is at the end of the surface of the heatsink, versus time (w_m = 7 m/s).

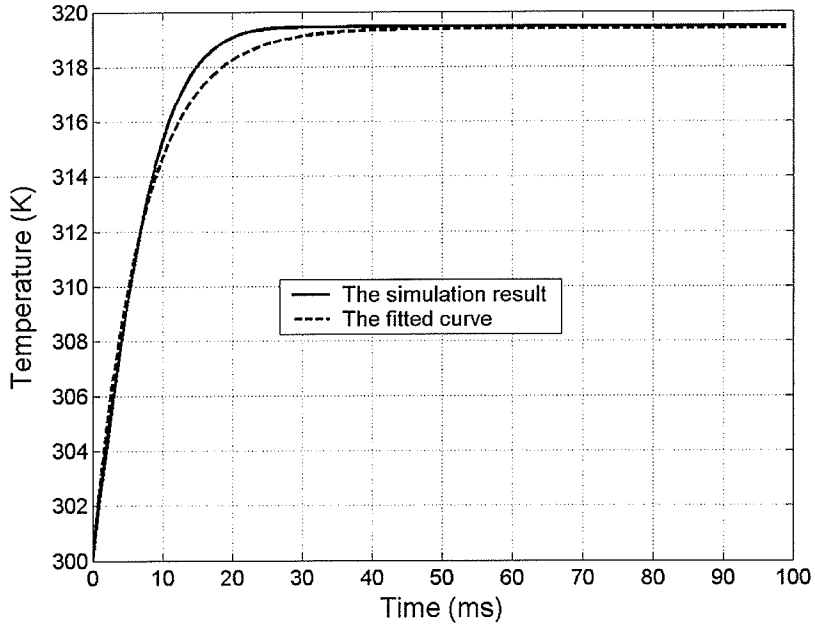

Figure 7-2. Transient response of the heatsink to an input heat step function compared to a first order exponential curve.

Figure 7-3 proposes a first order RC circuit model for the heatsink where R_{th} is equivalent to the overall thermal resistance of the heatsink and C_{th} is equivalent to its overall thermal capacitance, and the input current (I_0) is equivalent to the input heat (q''). This circuit model is described by equation 7-3 where T_{in}, the initial temperature of the heatsink and the temperature of the input water (300 K) is considered as the base temperature.

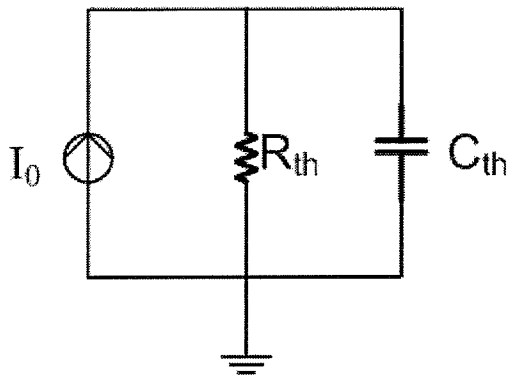

Figure 7-3. An RC circuit that can be modeled by a first order differential equation.

$$T_{\max}(t) - T_{in} = R_{th} q'' \left(1 - e^{-\frac{t}{R_{th} C_{th}}} \right) \tag{7-3}$$

From circuits theory we know that after 4 time constants ($\tau = RC$) $T_{max}(t)$ reaches 98 % of the final value. The final (or steady state) value of $T_{max}(t)$ also depends solely on the thermal resistance. Therefore in order to find R_{th} and C_{th} from the step function response of the heatsink the following steps are taken:

1. First from the final value (steady state) of $T_{max}(t)$ thermal resistance is calculated.

$$R_{th} = \frac{T_{\max}(\infty) - Tin}{q''} \tag{7-4}$$

2. Then from the time that it takes in the simulation result for the curve to reach 98 % of the final value, time constant (τ) is calculated.

$$\tau = \frac{t(98\%)}{4} \tag{7-5}$$

3. From τ and R_{th} thermal capacitance is calculated:

$$C_{th} = \frac{\tau}{R_{th}} \tag{7-6}$$

For 36 cases (Materials: copper, silicon, nickel; w_m = 2, 7, 14 m/s; and H_T = 10, 50, 100, 150 μm) transient simulation was performed and R_{th} and C_{th} values were found based on the time constant of the rise time listed in Table 7-1. The obtained thermal resistances and capacitances for different simulated cases are listed in Table 7-2. In Figure 7-4 the simulated transient temperatures in response to a heat step function input and the temperatures obtained from the first order differential equation model are sketched for 6 different simulated cases. These figures show that the first order exponential equation is a good approximation for the heatsink and the first order RC circuit model can be used as an equivalent model for the heatsink.

Table 7-1. Time constants of the rise time for 36 simulated cases.

		Time Constant (ms)		
	w_m (m/s)	**2**	**7**	**14**
H_T = **10 μm**	**Cu**	13.2	5.08	3.3
	Si	8.06	2.9	1.77
	Ni	15	5.73	3.48
H_T = **50 μm**	**Cu**	18.1	7.08	4.7
	Si	10.4	3.92	2.53
	Ni	20.9	8.18	5.3
H_T = **100 μm**	**Cu**	24.3	9.67	6.34
	Si	13.3	5.17	3.39
	Ni	28.4	11.3	7.3
H_T = **150 μm**	**Cu**	30.3	11.7	7.66
	Si	16.4	6.17	3.99
	Ni	35.6	14	9.01

Table 7-2. Thermal Resistances (Kcm^2/W) and Capacitances (J/Kcm^2) based on curve fitting for heatsinks with 4 different values of H_T, 3 different values of fluid mean velocity, and for heatsinks made out of copper, silicon, and nickel.

		Thermal Resistance (Kcm^2/W)			Thermal Capacitance (J/Kcm^2)		
	w_m (m/s)	**2**	**7**	**14**	**2**	**7**	**14**
$H_T = 10$ µm	**Cu**	0.527	0.194	0.123	0.0250	0.0262	0.0268
	Si	0.534	0.197	0.125	0.0151	0.0148	0.0142
	Ni	0.539	0.199	0.127	0.0278	0.0288	0.0274
$H_T = 50$ µm	**Cu**	0.525	0.194	0.124	0.0345	0.0365	0.0380
	Si	0.534	0.199	0.128	0.0195	0.0197	0.0198
	Ni	0.541	0.204	0.132	0.0386	0.0401	0.0403
$H_T = 100$ µm	**Cu**	0.523	0.195	0.125	0.0464	0.0496	0.0507
	Si	0.535	0.202	0.131	0.0250	0.0256	0.0259
	Ni	0.545	0.209	0.137	0.0522	0.0541	0.0532
$H_T = 150$ µm	**Cu**	0.522	0.188	0.121	0.0580	0.0625	0.0633
	Si	0.536	0.196	0.128	0.0306	0.0315	0.0312
	Ni	0.548	0.206	0.137	0.0650	0.0678	0.0658

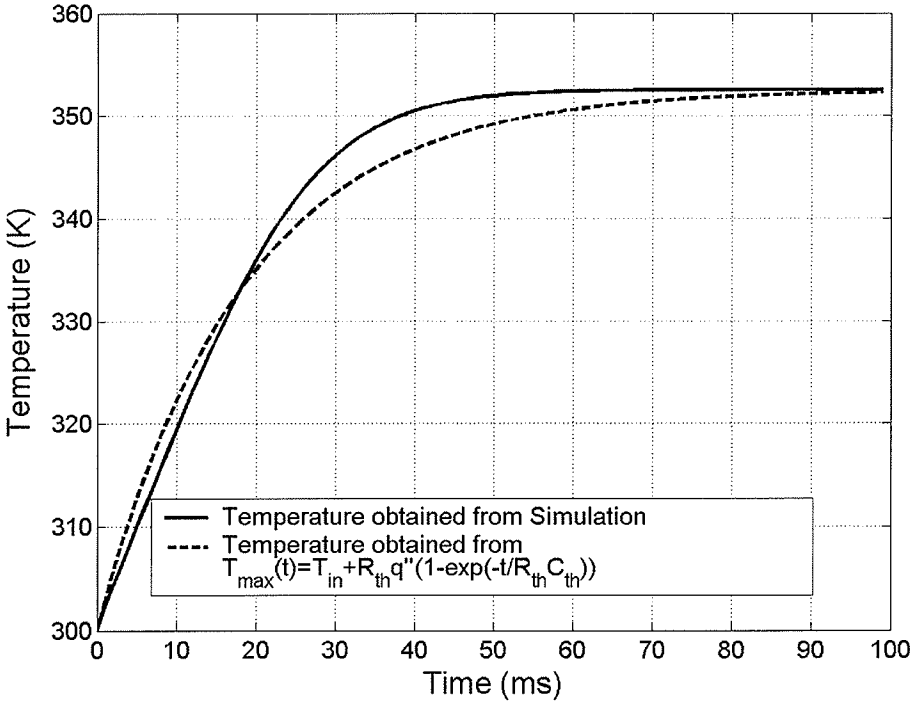

Figure 7-4(a). Solid material: Cu, $w_m = 2$ m/s, $H_T = 50$ μm.

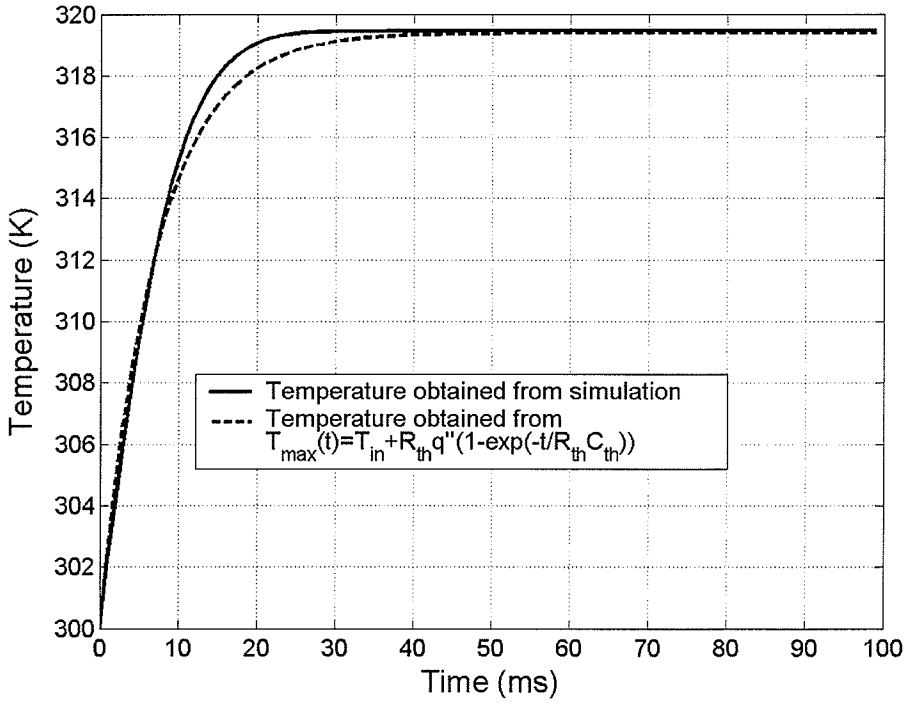

Figure 7-4(b). Solid material: Cu, $w_m = 7$ m/s, $H_T = 50$ μm.

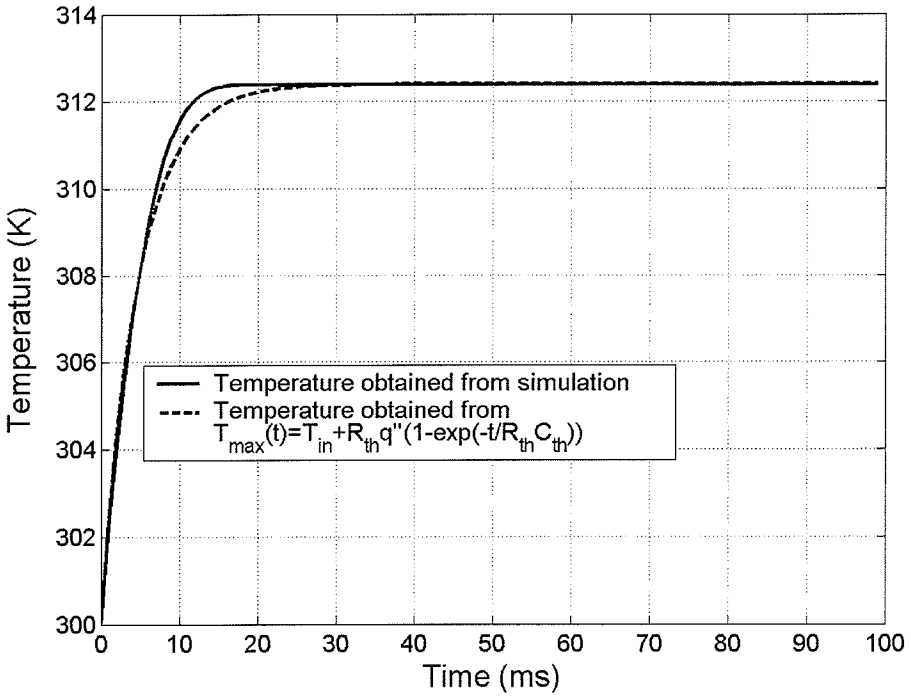

Figure 7-4(c). Solid material: Cu, $w_m = 14$ m/s, $H_T = 50$ μm.

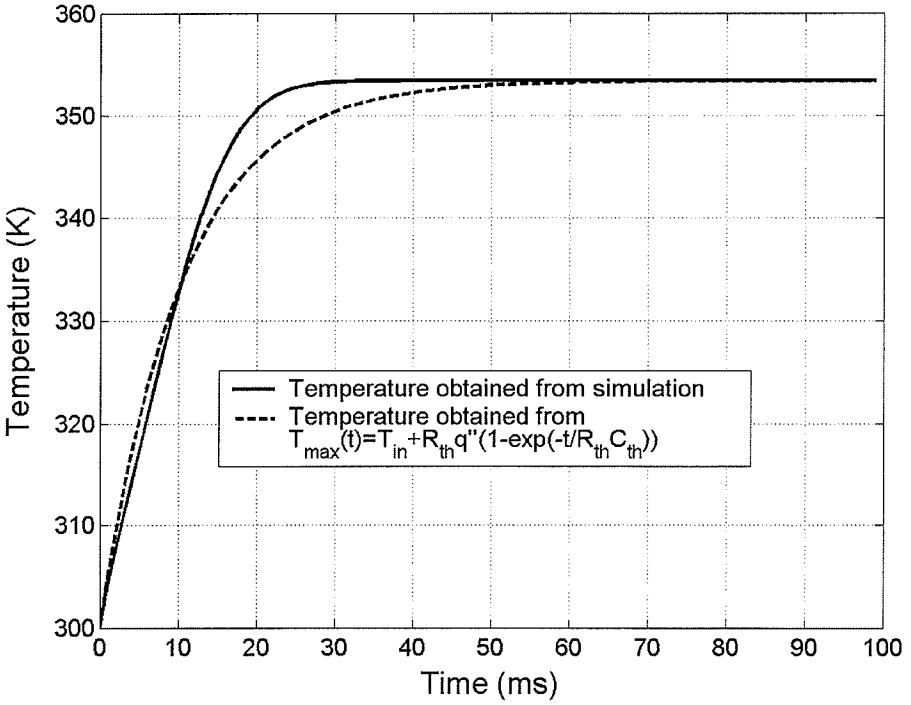

Figure 7-4(d). Solid material: Si, $w_m = 2$ m/s, $H_T = 50$ μm.

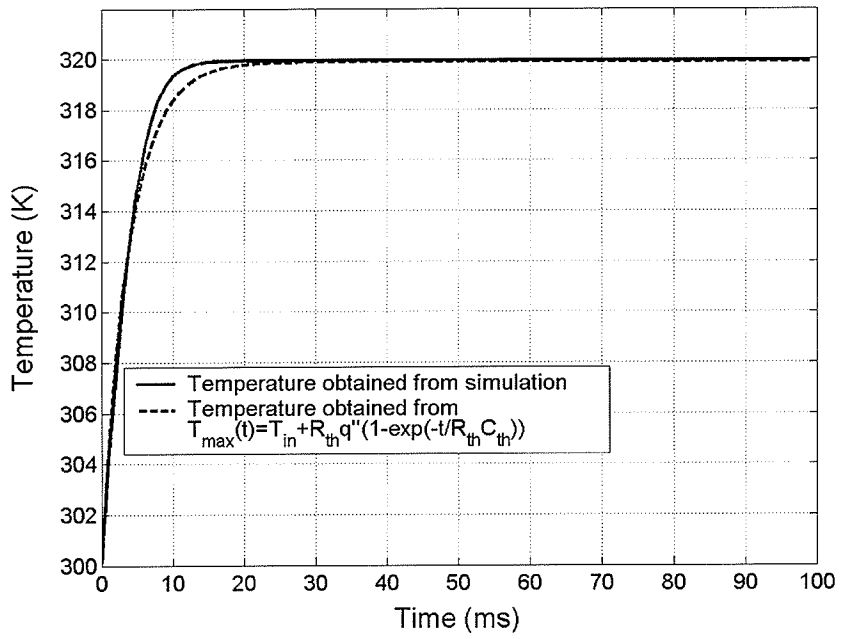

Figure 7-4(e). Solid material: Si, w_m = 7 m/s, H_T = 50 μm.

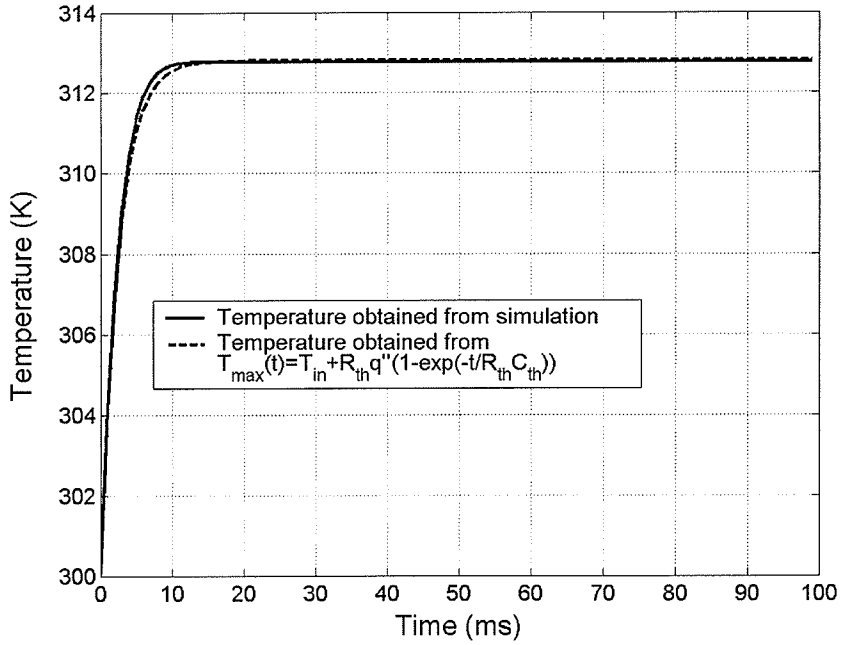

Figure 7-4(f). Solid material: Si, w_m = 14 m/s, H_T = 50 μm.

Figure 7-4. Simulated transient response of the heatsink to an input heat step function compared to the closest first order exponential curves for 6 different cases.

As observed in Table 7-2, in most cases, with increasing the fluid velocity, the thermal capacitance increases. Also with increasing H_T the thermal capacitance increases. These both are expected, because the overall thermal capacitance is directly proportional to the total mass of the heatsink. The ratios of the thermal capacitances for the different simulated cases are listed in Table 7-3.

Table 7-3. Ratios of Thermal Capacitances for different simulated cases.

		Hot spot width = 1 mm		
	w_m (m/s)	**2**	7	**14**
H_T = **10 µm**	**Cu / Si**	1.65	1.77	1.88
	Cu / Ni	0.9	0.91	0.98
H_T = **50 µm**	**Cu / Si**	1.77	1.85	1.92
	Cu / Ni	0.89	0.91	0.94
H_T = **100 µm**	**Cu / Si**	1.86	1.93	1.96
	Cu / Ni	0.89	0.92	0.95
H_T = **150 µm**	**Cu / Si**	1.89	1.98	2.03
	Cu / Ni	0.89	0.92	0.96

Considering the numbers listed in Table 7-3 more quantitatively, it is observed that at a specific fluid velocity for all values of H_T:

$$R_{th}(Cu) \approx R_{th}(Si) \approx R_{th}(Ni) \quad (7\text{-}8)$$

$$C_{th}(Cu) \approx 2\, C_{th}(Si) \quad (7\text{-}9)$$

$$C_{th}(Cu) \text{ is slightly less than } C_{th}(Ni) \quad (7\text{-}10)$$

These relationships show that thermal resistance depends mostly on the fluid velocity and it does not depend much on the heatsink material or H_T. Opposite to R_{th}, the thermal capacitance depends mostly on the heatsink material and H_T, but doesn't change much with the fluid mean velocity. As observed, C_{th} is determined mostly by the mass and specific heat of the solid part of the heatsink, and not the fluid.

Table 7-4 shows the specific heat of the different materials used for the studied heatsinks [53]. On the third column of this table the thermal capacitances of the volume unit of these materials are listed. This value is obtained from equation 7-8 from the specific heat and density of these materials:

$$C_{tot} = \rho Cp \quad (7\text{-}11)$$

From Table 7-3 we can see that the thermal capacitances of the solid materials vary as:

$$C_{th}(Cu) = 2.08\, C_{th}(Si) \quad (7\text{-}12)$$

$$C_{th}(Cu) = 0.87\, C_{th}(Ni) \quad (7\text{-}13)$$

These relationships are similar to the relationships concluded from Table 7-3 (relation 7-8 to 7-10).

Table 7-4. Thermal capacitances of the materials used for the studied heatsinks.

	C_p (J/kgK)	ρ (kg/m^3)	C_{tot} (J/m^{3}K)
Cu	385	8920	3,434,200
Si	710	2330	1,654,300
Ni	444	8908	3,955,152
Water	4181	1000	4,181,000

Comparing the ratios of Table 7-3 with the ratios of relationships resulting from Table 7-4 (relations 7-12 and 7-13) supports conclusion that C_{th} is determined mostly by the mass and specific heat of the solid part of the heatsink. It can be said that the origin of copper's superior C_{th} to that of silicon is its higher density. The other concluded point is that as observed in Table 7-3 for Cu/Si ratio, as H_T or the fluid velocity increases, the ratios of the thermal capacitances get closer to the ratios of the thermal capacitances of the solids (equation 7-12).

Table 7-5 shows the thermal capacitances of the different parts of the solid heatsink. Comparing these values to the values of C_{th} in Table 7-2 gives some information about the dependence of the thermal capacitance of the heatsink on different parameters. As observed, for H_T = 10 μm the thermal capacitance of all of the heat sink solid body is very close to the total actual thermal capacitance of the heatsink, but for H_T > 100 μm the thermal capacitance of the top and walls of the heatsink approximately equals its total actual thermal capacitance. This shows that for small H_T, the entire heatsink's solid body participates in heat transfer, but as H_T increases, the bottom plate

and the bottom part of the walls do not transfer much heat, and their thermal capacitances are not included in the total actual thermal capacitance of the heatsink.

Table 7-5. Heat Capacitances (J/Kcm^2) of the solid parts of the heatsink.

		C_{th} of the solid part (J/Kcm^2)	**C_{th} of the top layer and separating walls** (J/Kcm^2)	**C_{th} of the top layer** (J/Kcm^2)
H_T = 10 μm	**Cu**	0.0292	0.0120	0.0034
	Si	0.0141	0.0058	0.0017
	Ni	0.0337	0.0139	0.0040
H_T = 50 μm	**Cu**	0.0429	0.0258	0.0172
	Si	0.0207	0.0124	0.0083
	Ni	0.0494	0.0297	0.0198
H_T = 100 μm	**Cu**	0.0600	0.0430	0.0344
	Si	0.0289	0.0207	0.0166
	Ni	0.0692	0.0494	0.0395
H_T = 150 μm	**Cu**	0.0774	0.0602	0.0516
	Si	0.0373	0.0290	0.0249
	Ni	0.0891	0.0693	0.0594

Figures 7-5 to 7-7 show the transient surface temperatures of the heatsinks made out of copper, nickel, and silicon in response to a uniform heat step function for three mean fluid velocities of w_m = 2, 7 and 14 m/s. The other simulation parameters were:

- W_C = 50 μm.
- $H_C = H_T = H_B$ = 50 μm.
- S = 50 μm.

As observed, at the beginning of the transient condition the difference between the maximum surface temperatures of copper or nickel and silicon heatsinks is considerable. This difference happens due to the difference in the time constants of these heatsinks as mentioned in Table 7-1. For example, at w_m = 2 m/s the time constants are τ_{Cu} = 18.1 ms and τ_{Si} = 10.4 ms, a difference of 7.7 ms. At w_m = 14 m/s the time constants are τ_{Cu} = 4.7 ms and τ_{Si} = 2.53 ms, a difference of 2.17 ms. Hence at w_m = 14 m/s the maximum difference between the two surface temperatures is much less than that at w_m = 2 m/s. Since τ_{Ni} is close to τ_{Cu}, transient surface temperatures of copper and nickel heatsinks are similar to each other and the difference between them is about zero compared to the difference between their temperature and temperature of the silicon heatsink.

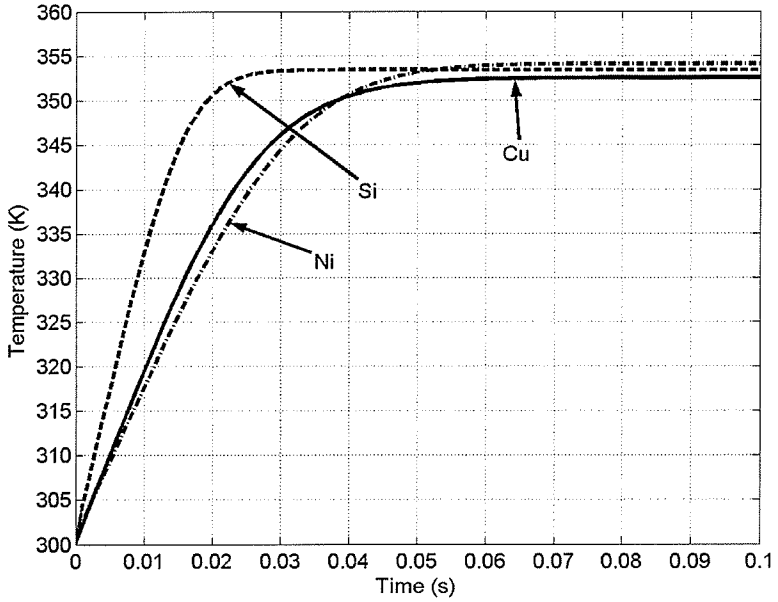

(a)

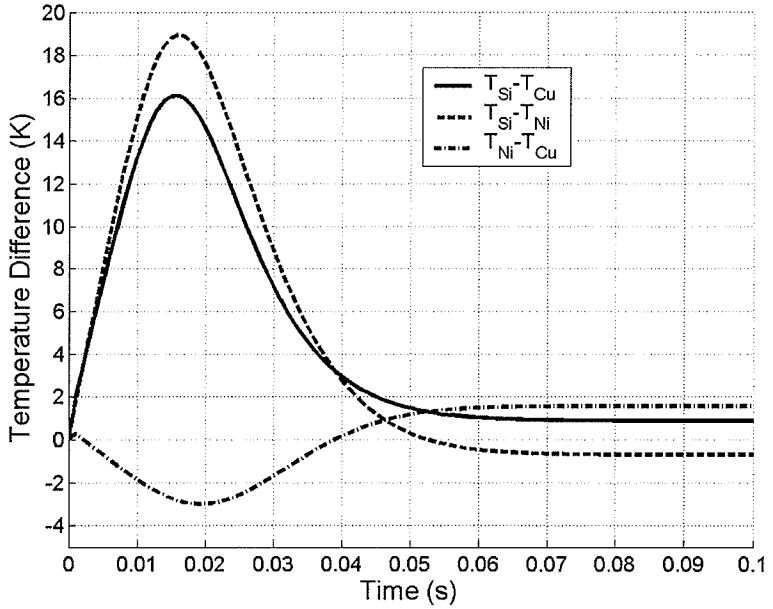

(b)

Figure 7-5. (a) Surface temperatures of the microfluidic heatsinks constructed from silicon, nickel, and copper in response to an input uniform heat step function with $w_m = 2$ m/s. (b) The difference between those three surface temperatures.

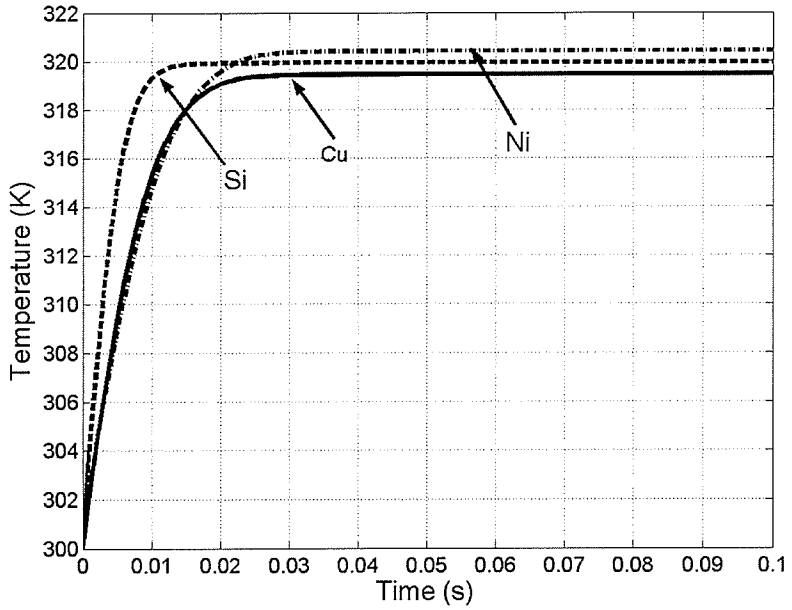

(a)

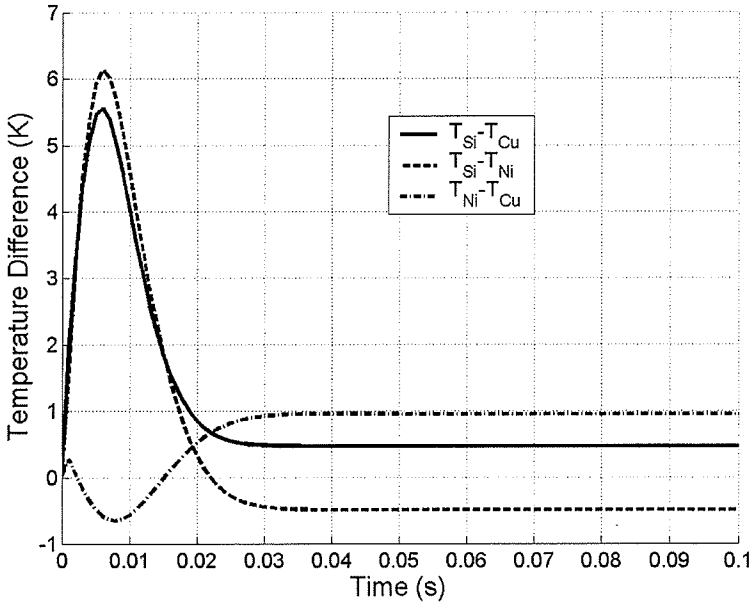

(b)

Figure 7-6. (a) Surface temperatures of the microfluidic heatsinks constructed from silicon, nickel, and copper in response to an input uniform heat step function with w_m = 7 m/s. (b) The difference between those three surface temperatures.

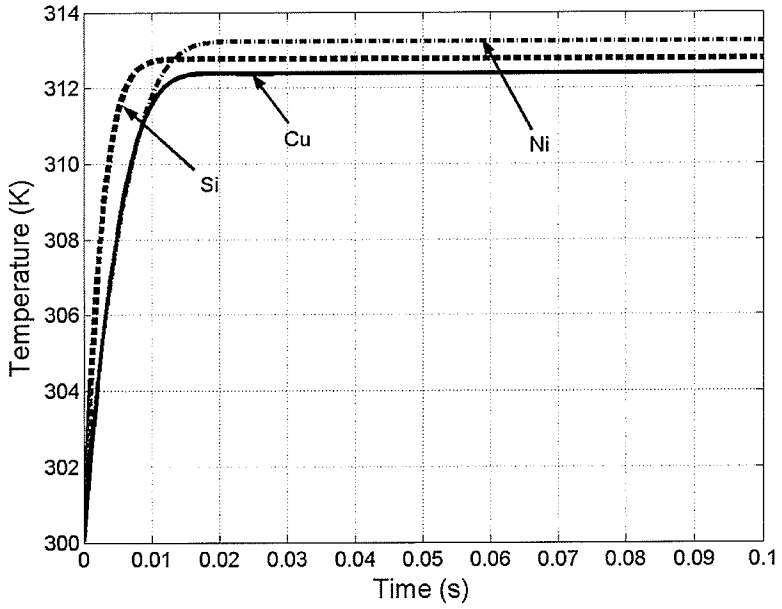

(a)

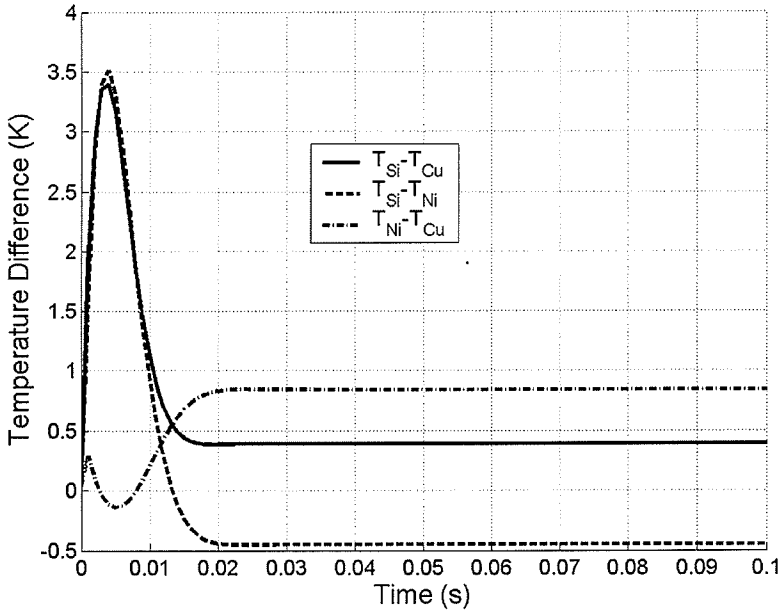

(b)

Figure 7-7. (a) Surface temperatures of the microfluidic heatsinks constructed from silicon, nickel, and copper in response to an input uniform heat step function with w_m = 14 m/s. (b) The difference between those three surface temperatures.

7.4. Summary

The simulations of this chapter show that the surface temperature of the copper heatsink in transient condition, and for variable heat input, is lower than the surface temperature of the silicon and nickel heatsinks. Therefore, a conclusion is that the copper heatsink is better for transient conditions, especially at high fluid velocities.

Another conclusion that can be made based on this study and data of Table 7-1 is that since larger H_T provides a larger time constant, and hence a lower peak temperature on the surface of the heatsink during the rise time, larger values of H_T are more desirable for transient conditions.

This study also shows that using a material with higher heat conductance is not necessarily good if it possess a small heat capacitance. This is illustrated by the simulations showing that the silicon heat sink performs poorer in transient situations than the nickel heat sink.

Finally, it should be mentioned that with the knowledge of the time constant for the heat sink and its transient characteristics, an IC chip can be designed in a way that its heat pulses and the time difference between them are set so that the chip's peak temperature doesn't exceed a certain limit.

Chapter 8

Fabrication of Metal Heat Exchangers

8.1. Fabrication of Microfluidic Heat Sinks

Microfluidic heatsinks are usually fabricated from two types of materials, silicon and metals. Silicon is a cheap material, it has a good heat conductance, and it is a familiar material in microtechnology labs, and the micromachining processes for it have been already developed. The other advantage of investigating silicon for fabrication of microfluidic heat sink is that integrated circuits are almost always fabricated on silicon wafers, and the microfluidic heat sink structure can be fabricated on the other side of the IC. For fabrication of microchannels in silicon, micromachining methods like anisotropic wet etching and DRIE are used. Anisotropic chemical etchants like KOH etch silicon with surface crystallographic orientation of <110> vertically. In this way, deep channels with the depth of up to 1000 μm and width of 1/5 of the depth have been fabricated [28]. Another way for fabrication of high aspect ratio microchannels in silicon is a process called Deep Reactive Ion Etching (DRIE) which is a type of plasma etching. For using this method, the surface crystallographic orientation of silicon can be anything. But generally DRIE is an expensive method due to its complexity and the cost of its tools. Using this method, microchannels with the depth of up to 200 μm and width of 1/6 of the depth have been fabricated [48].

Metals like aluminum, copper, and steel also are used for fabrication of microfluidic heat sinks. Microfluidic heatsinks in metals have been fabricated mainly by mechanical methods like milling and drilling. The problem of these mechanical methods is that very thin or high aspect ratio channels cannot fabricated easily. Most microchannels that have been fabricated with these methods have low (less than or around one) aspect ratio rectangular (close to square) cross-section or semi-circular cross-section shape [58].

Metal microfluidic heat sinks can be fabricated by micromachining methods too. These methods are based on either wet etching or electroplating. Using wet etching, semi-circular (or semi-elliptical) microchannels are made on the surface of the metal plate. The problem of this method (as will be shown) is that the channels have a very low aspect ratio. In the other method, which is based on micro-molding and electroplating, rectangular shape channels with low or high aspect ratio can be fabricated.

In this work mainly the method of fabrication using electroplating process has been investigated and a process flow for fabrication of microfluidic heat sink out of copper has been proposed.

8.2. Fabrication of Metal Microfluidic Heat Sink with Wet Etching Process

One of the simplest methods for fabrication of microfluidic heat sinks out of metal is based on chemical etching of metal. In this method, first the substrate is patterned by a photoresist and then microchannels are etched into the metallic substrate. For metals, isotropic etching using liquid chemicals is much easier than anisotropic

etching. Then the channels are sealed by a cap layer, which is bonded or glued to the substrate. Process flow of this idea is shown in Figure 8-1. Using this method, microchannel structures out of metals like stainless steel, copper, and aluminum have been fabricated. One problem of this method is that since isotropic etching proceeds in all directions with the same rate, as the channels are etched in depth, etching proceeds almost with the same rate toward the sides under the photoresist layer causing an under-cut. Hence the maximum width of the channel will be almost equal to the photoresist opening plus twice the channel depth. This under-cut causes the microchannel to be semi-elliptic instead of semi-circular, and reduces the aspect ratio of the channels.

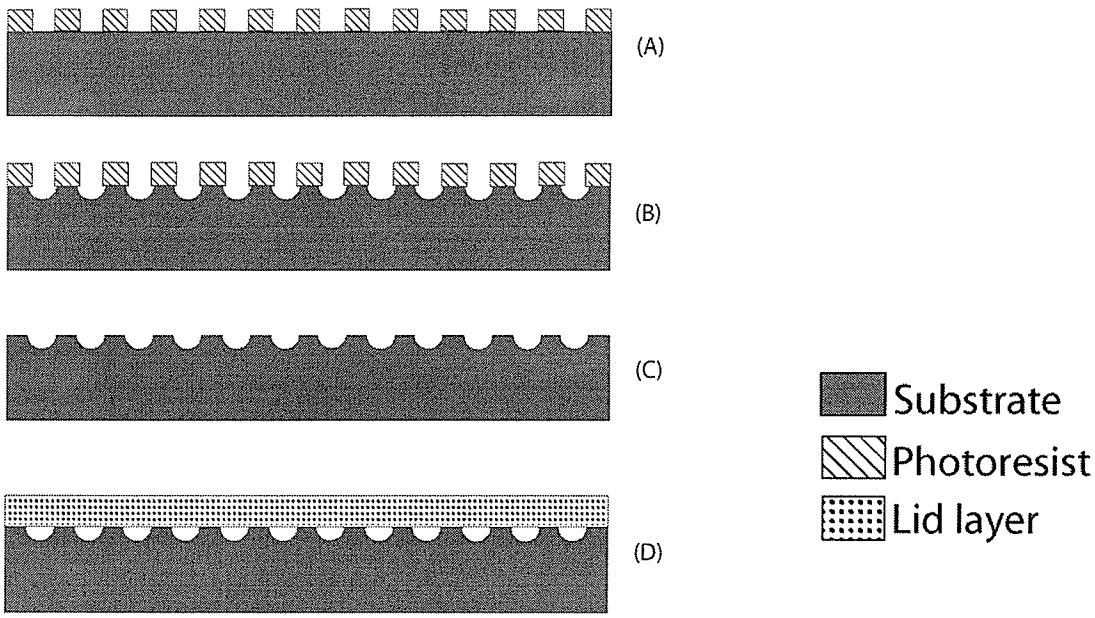

Figure 8-1. (A) Substrate with patterned photoresist on it. (B) Making the channels by wet etching of metal. (C) Removing the photoresist. (D) Covering the channels by bonding another layer on top of the substrate.

This etching method was tried with aluminum according to the following scheme:

1. The aluminum plate surface was polished with very fine sand paper (grit 2000).
2. Then it was patterned with 1 μm thick layer of a positive photoresist, HPR 504.
3. The surface was etched using aluminum wet etch process. The Al etchant solution containing phosphoric acid, acetic acid and nitric acid was obtained from Arch Chemicals. The etching is done at 50 °C and the etch rate of aluminum at this temperature is about 530 nm/min.

Figure 8-2 shows the cross-section of this structure. Microchannel and reservoirs are etched and the through holes are drilled. In Figure 8-3 the top view of the fabricated microchannels is shown. As seen in the image, the microchannels end at the reservoir that is connected to inlet/outlet. In Figure 8-4 the profile of the etched channels is shown. This image is obtained by Alpha-Step profiler. Since the etch window opening made by lithography process was 50 μm, channels with the height (or depth) of about 60 μm and the width of about 150 μm were fabricated. As observed in Figure 8-4 the maximum undercut etching on each side is about 75 μm (giving a maximum width of 200 μm for the channels) and maximum etching at the depth is 65 μm.

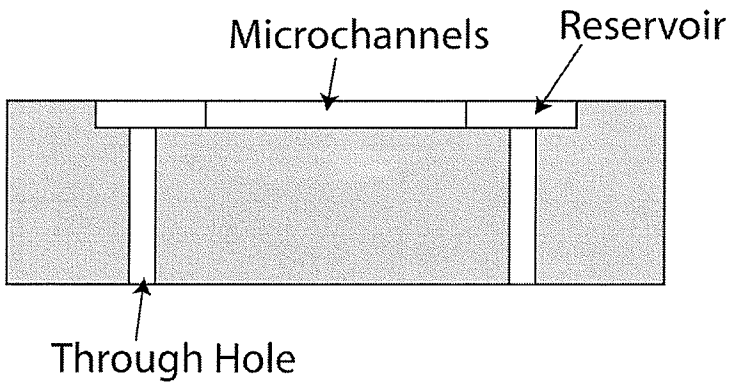

Figure 8-2. Cross section of the microchannel structure made by wet etching. Microchannels and reservoirs are etched and the through holes are drilled.

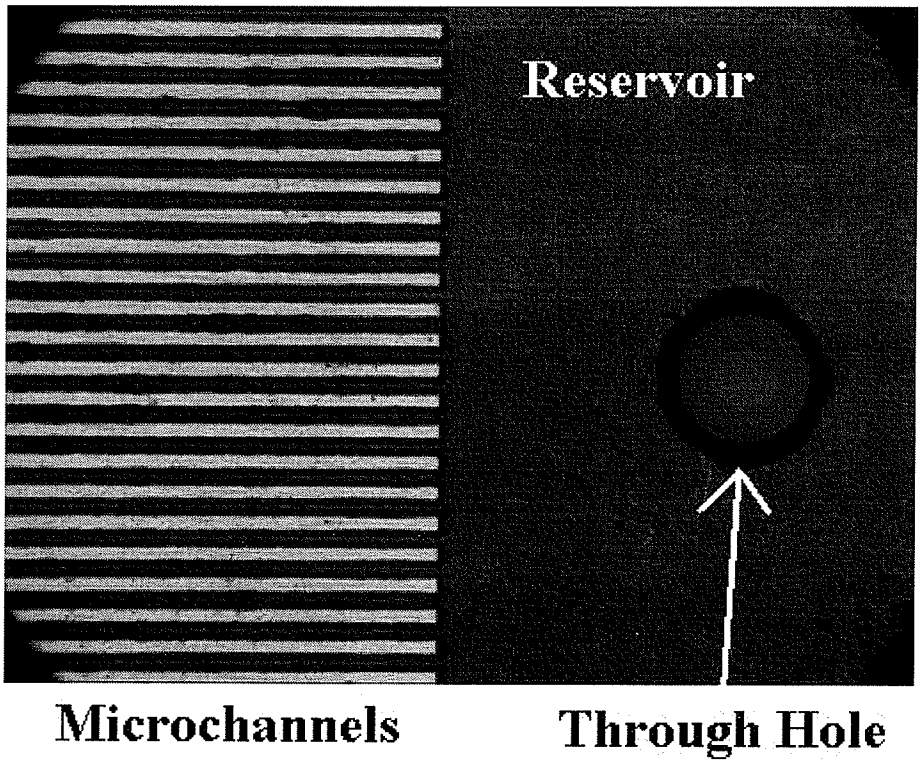

Figure 8-3. Photograph of the etched channels in Aluminum plate and the inlet/outlet hole.

This fabrication method has some problems:

- Since the isotropic etching process has significant undercut, the fabricated microchannels have semi-circular or semi-elliptic shape and have a very low aspect ratio. This limits the performance of the microfluidic heatsink, because low aspect ratio microchannels have a small area for heat transfer from solid to fluid.
- Metal wet etching process is a hard to control process and leaves the microchannel edges and surfaces rough and inconsistent. This can be observed in Figure 8-3 by looking at the edges of the microchannels.

Due to these problems it was decided to focus the fabrication work of this thesis on another method based on mold and electroplating.

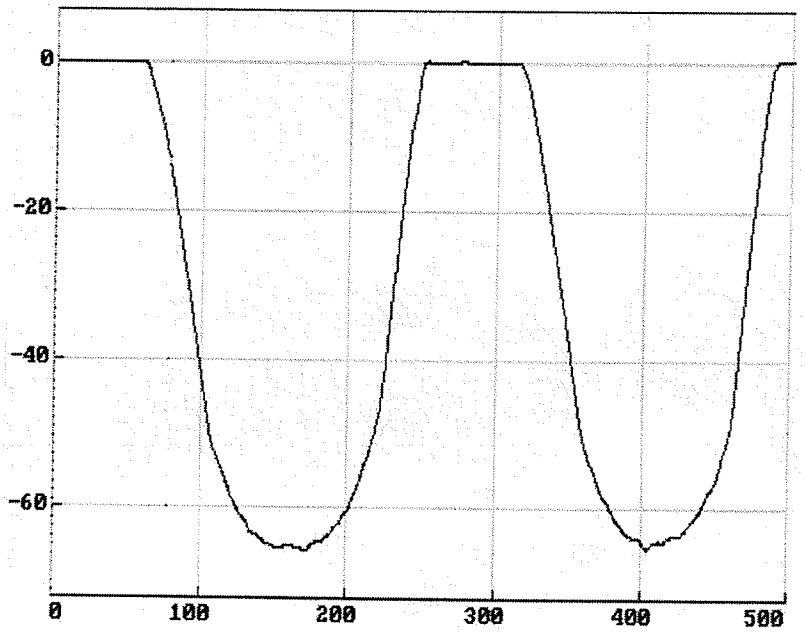

Figure 8-4. Profile of the etched channels obtained by Alpha-Step profiler.

8.3. Fabrication of Copper Microfluidic Heat Sink using Electroplating Process

Microfluidic heatsinks can be fabricated using electroplating process too. In this method, the channels or more correctly the walls between the channels are formed from electroplated copper. Copper is selected due to its very high heat conduction compared to other easily available materials, and lower cost than gold, which can also be electroplated. A method for fabrication of copper microfluidic heat sink with electroplating process is demonstrated. The main challenge is in the last step which is removing the photoresist and covering the channels.

The first process flow that was investigated is illustrated in Figure 8-5. First, a thin and flat substrate of appropriate size (a few cm^2) is needed. For this purpose either polished silicon wafers or copper plates were prepared (Polishing method is explained more in section 8.3.1). Since for the electroplating process a conductive seed layer is needed, when using a polished silicon wafer as the substrate it is necessary to deposit a very thin (~0.1 μm) layer of copper (or gold) on the silicon substrate (Figure 8-5.A). This can be done by sputtering or evaporation, and since copper doesn't adhere to silicon directly, a thin (~10 nm) chrome layer also is used as an adhesion layer. Unoxidized chrome adheres well to both silicon and copper.

A thick layer of a photoresist is then used as the electroplating mold. Thickness is defined by the height of the micro-channels which are to be made. This thickness can be from tens of microns to a few hundreds of microns. Using a lithography process, the

photoresist layer is patterned to form the electroplating mold needed to define the micro-channels (Figure 8-5.B).

Copper is then electroplated inside the mold on the surface (Figure 8-5.C). The electroplating is continued, until the copper grows over the height of photoresist mold (Figure 8-5.D). This over-growth process (often termed mushrooming) is continued until copper covers the entire photoresist layer, thus, forming the top of the future micro-channels. If desired, the top surface of the copper can be polished to smooth out the mushroomed channel tops. Finally, the photoresist mold has to be washed away by an appropriate solvent like acetone. After photoresist removal, the final structure is of copper walled channels on the substrate surface (Figure 8-5.E).

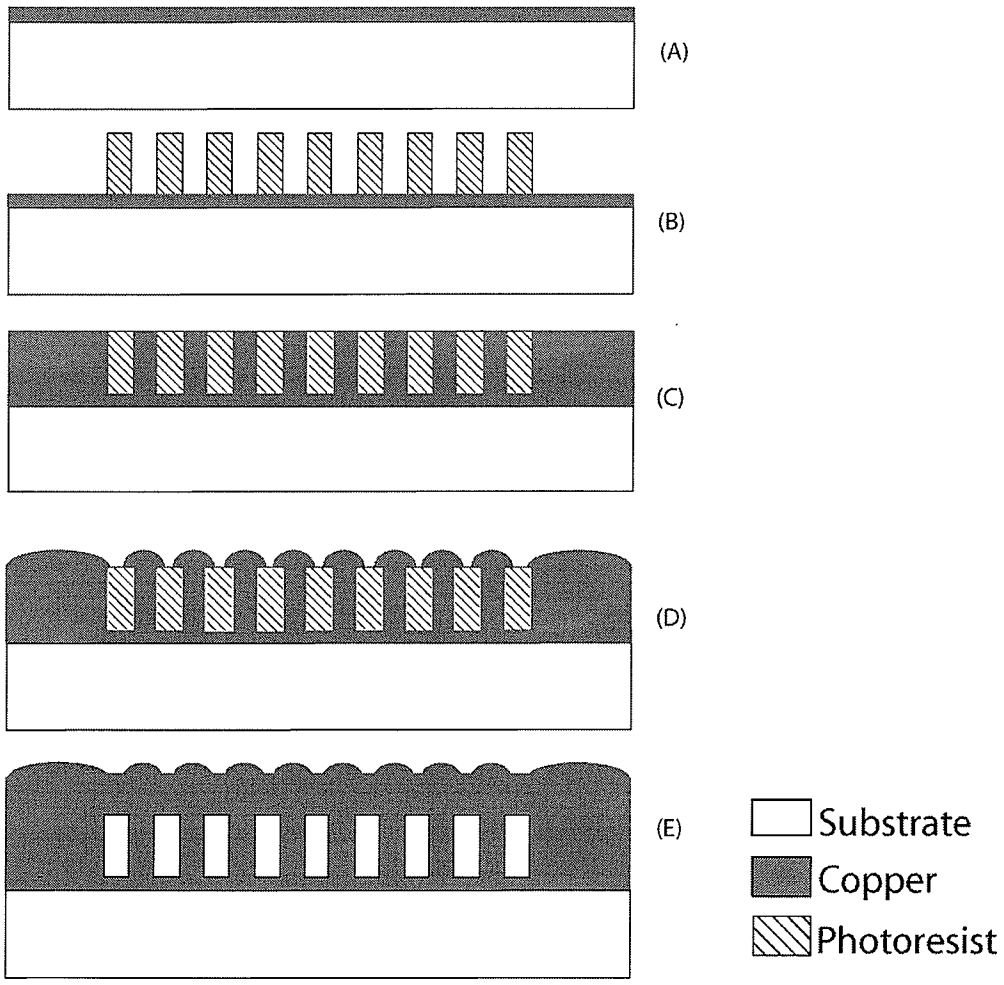

Figure 8-5. (A) Coat substrate with electroplating seed layer. (B) Coat with molding material and pattern it lithographically. In this work a spin-on photoresist is used. (C) Electroplating the copper metal into the regions defined by the mold. (D) Continue the electroplating over the mold to seal the top surface of the defined channel. (E) Remove the photoresist mold, leaving the microchannels surrounded by copper walls and top.

In Figure 8-6 step-by-step covering of the mold by electroplating and so called mushrooming process is demonstrated. The mushrooms grow, reach each other and merge, and make the top solid layer.

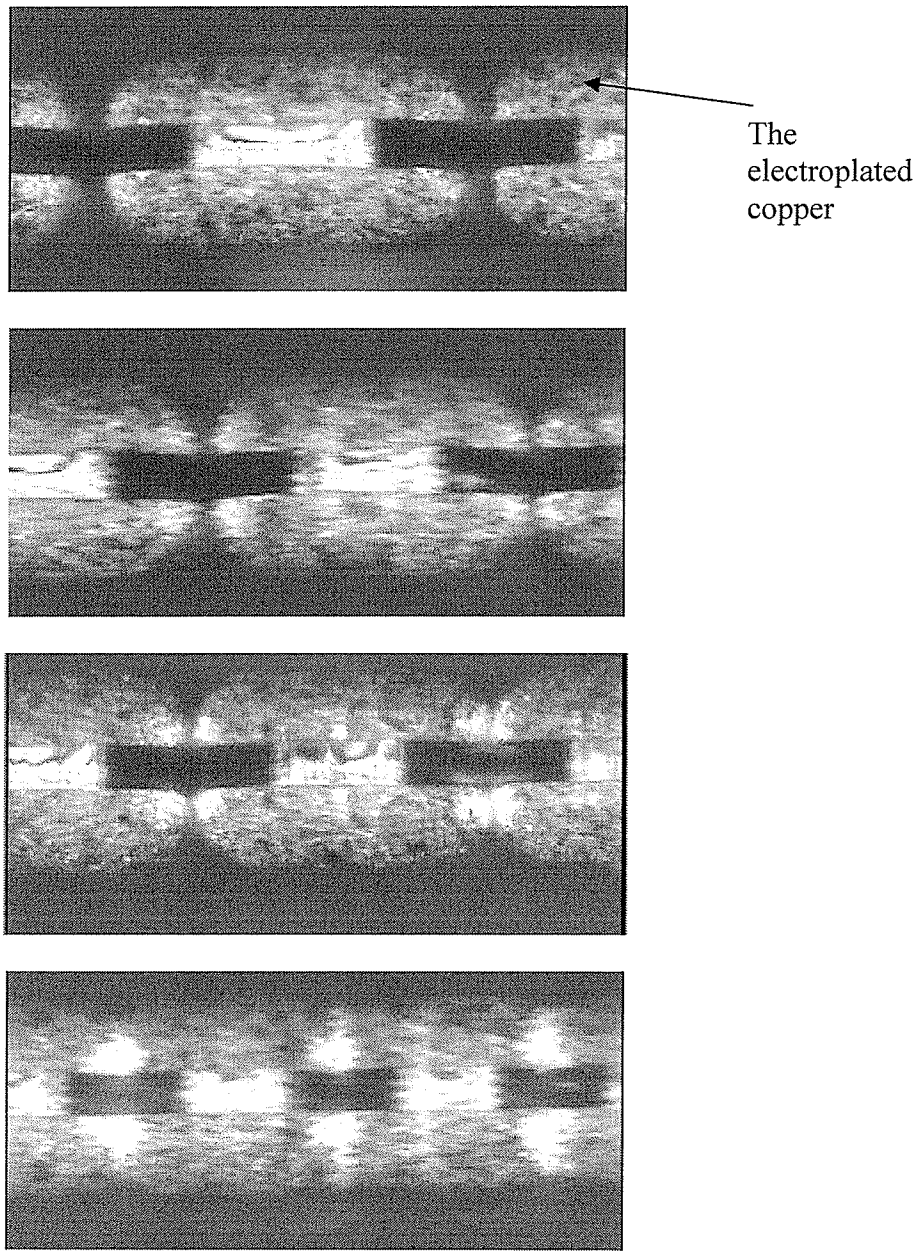

Figure 8-6. From top to bottom: Steps of covering the photoresist mold by mushrooming process. The bottom half of each picture is just the reflection of the electroplated layer in the mirror-like substrate.

The problem with this method is that removing the photoresist from the covered long and narrow channels is not easy. If just the structure at the end of step 8-5.D is put in the solvent (acetone), the photoresist will be dissolved extremely slowly. Using Shipley Megaposit SPR 220-7.0 photoresist with channel height of 30 μm and channel width of 50 μm even after 24 hours only a few tens of microns of photoresist along the channel was removed. For solving this problem, there are four solutions:

1. Push the solvent (e.g. acetone) by pressure into one end of the microchannels [59]. For the success of this technique the plated layer has to have a very good adhesion to the substrate, or it has to be held by a strong external force against the substrate during pushing the solvent.

2. Stop electroplating just before that the channels are totally covered and a small distance of a few microns remains between the mushroom edges. Then wash the photoresist, and continue the electroplating to cover the channels and form the top layer with enough thickness. In doing this method a few microns of copper will deposit on the internal surfaces of the channels also. In order to compensate for this extra thickness on the walls, the walls can be designed narrower in the lithography step. This method was used to fabricate a microfluidic heat sink structure by electroplating nickel [12].

3. Use a photoresist that turns into gas at elevated temperature, and so it can exit through the inlet/outlet holes and the walls. For example Unity Sacrificial Materials (from Promerus Electronic Materials) are a family of photosensitive polymers (photoresist) that decompose into gas at temperatures below 250 °C. In

[60] a microfluidic heat sink based on this method was fabricated. The problem with this method is that only special types of photoresists can be used.

4. Instead of using mushrooming to cover the microchannels, bond a lid layer to cover them. In this method, copper is electroplated as thick as the photoresist, photoresist is removed, and then channels are covered by bonding another plate on top of the microchannel structure.

The process flow based on the 4th solution is shown in Figure 8-7. Steps A-C of this process flow are like the method explained in Figure 8-5. In step D of Figure 8-7, a thin layer of tin (1-2μm) is electroplated on top of the copper layer, and also on another plate (lid plate) which will be used to seal the channels. The photoresist is then removed (Figure 8-7.E). After photoresist removal, the cover layer is put on top of the microchannels and by increasing the temperature to above the melting point of tin, 232°C, and applying some pressure they will bond to each other (Figure 8-7.F). In Figure 8-8 the fabricated microchannel structure at the end of step E (before sealing) is shown. In this case, the substrate is a 3 × 4.5 cm and 1 mm thick copper plate whose surface has been polished. The width of the channels and the distance between them is 50 μm and two holes in the reservoir at the end of the channels have to be drilled to be used as the inlet and outlet for water. These inlet and outlet holes can be made on either the bottom plate or the top plate.

In Figure 8-9 a close-up photograph of the same copper microchannel structure is shown. The height of the channels is about 20 μm and their width is about 50 μm. Due to

some extra electroplating, some mushrooming has happened and hence the width of the walls appears larger than the channel width, due to the angle that this picture was taken.

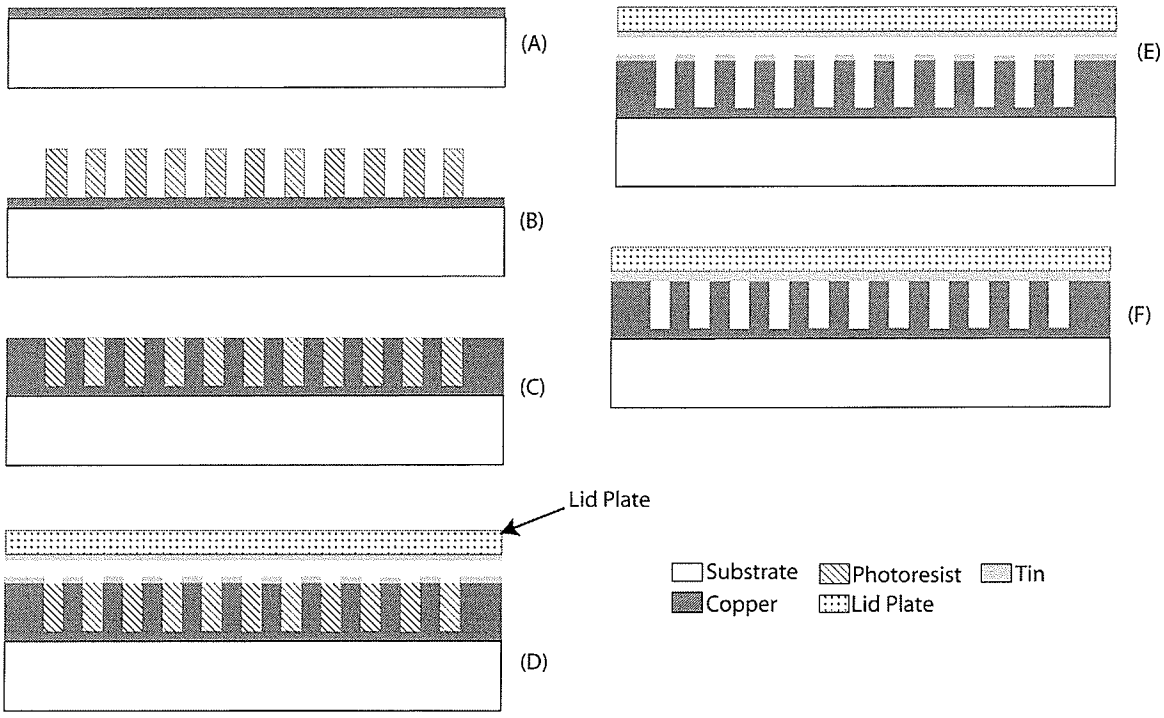

Figure 8-7. Process flow for fabrication of microfluidic heat sink in copper. (A) Coat substrate with sputtering seed layer on it. (B) Coat with molding material and pattern it lithographically. In this work a spin-on photoresist is used. (C) Electroplating the copper metal into the regions defined by the mold. (D) A thin layer of tin is electroplated on top of the copper layer, and also on the lid plate which will be used to seal the channels. (E) The photoresist is removed. (F) The lid plate is bonded to the substrate to cover and seal the microchannels.

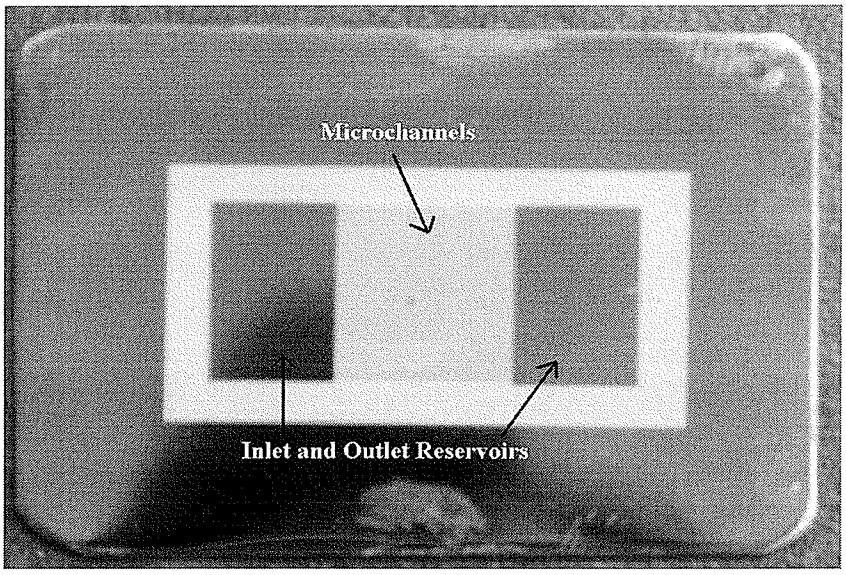

Figure 8-8. Top view of the copper microchannel structure made by electroplating. Inlet and outlet holes can be made at either bottom plate or top plate.

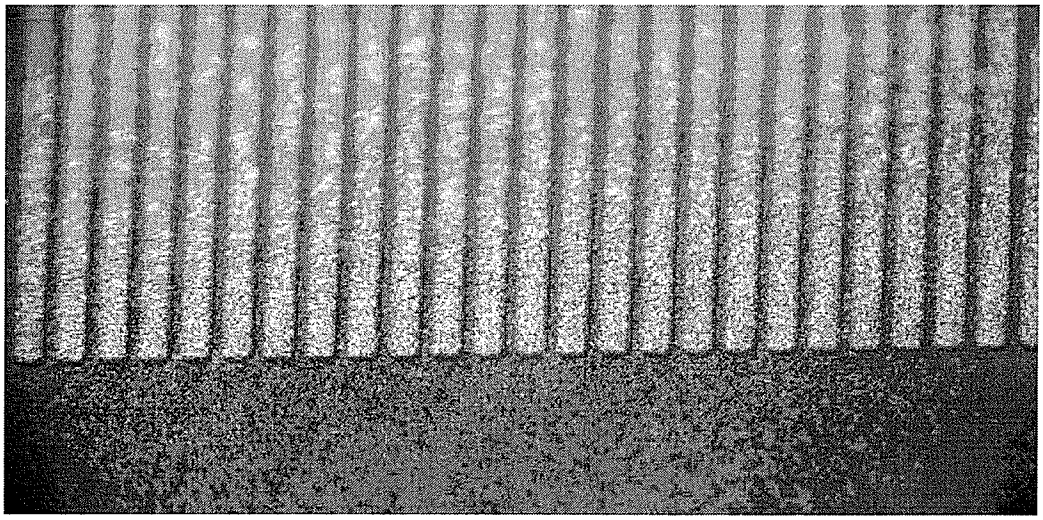

Figure 8-9. Photo of the side and top view of the copper microchannels. The height of the channels is about 20 μm and their width is about 50 μm. Due to some extra electroplating, some mushrooming has occurred and therefore the width of the walls from top looks larger than the channels width.

This micro-molding fabrication method has several important advantages over common methods of fabrication of microfluidic heat sinks in silicon and metal. This process is cheap and is done at low temperatures; hence it can be integrated on the back of electronic chips and sensitive devices. This method is applicable to any substrate, including metals, or silicon wafers with any crystallographic orientation. Channels made by the electroplating technique can have any shape and even be curved; while channels made by crystallographic etching of silicon are limited in their geometry and can be only straight.

This electroplating method allows the fabrication of much smaller channels in metals compared to the milling method. By using smaller channels, more channels per unit area can be fabricated, and since smaller channels have a larger surface area to volume ratio, the microfluidic heat sink made by this method can transfer more heat. In the next sections the details of the experimental work on this proposed fabrication method are explained and discussed.

8.3.1. Polishing the Copper Substrate

Since the height of the microchannel structures which are fabricated on the substrate is at least on the order of several microns, the roughness of the substrate has to be very small. The reason is that large roughness deteriorates the fabrication process (e.g. photoresist spinning) and occupies some volume of the fabricated microchannels. In order to polish the copper plates, the following steps are taken:

1. A 1 mm thick copper plate is cut at the suitable size (for us, 3×4.5 cm^2). Then with a double sided masking tape it is mounted on a metal holder (Figure 8-10).

2. The plate is polished with sanding paper with the grits of 300 (the roughest), then 600, then 800, then 1200, then 1500, and at last 2000 (the finest). The plate obtained at the end of this step looks very smooth and had a roughness height of 10-100 nm as measured by Alpha-Step profiler.

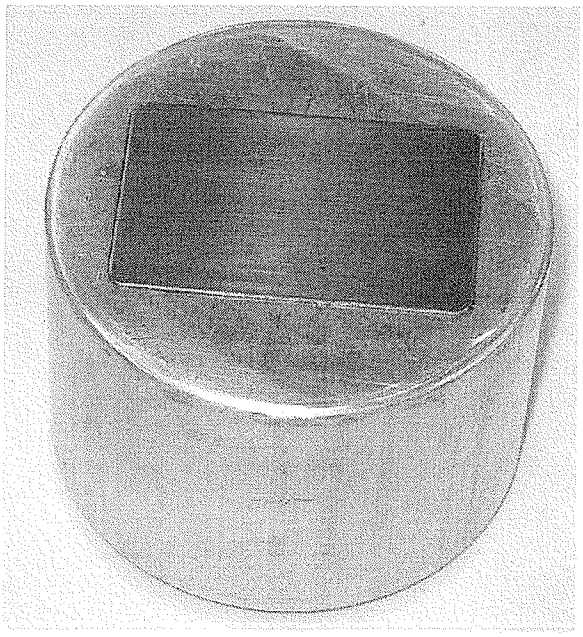

Figure 8-10. The copper plate mounted on the metal holder for polishing.

There are some important points regarding polishing of copper plates.

1. Copper, contrary to silicon, is a soft material. It can be bent, curved and scratched easily. Hence it should be treated very carefully during and after polishing. Even the residue of copper on the sand paper and polishing wheel can scratch the surface. Hence water should always be running on the sand paper, and the polishing wheel should be cleaned with DI water very often.

2. The direction of polishing on the surface should be changed constantly. When polishing with sand paper, when the sanding paper is changed to a finer one, the plate should be polished in the direction perpendicular to the previous one. In this way the grooves made by one sand paper will be polished and removed by the finer one. When using a polishing wheel, the direction of the plate surface on the wheel should be changed and rotated constantly. Keeping the plate surface in the fixed position on the polishing wheel causes parallel grooves on the surface.
3. Other than roughness, one other issue with the plate surface is its flatness. In order to keep the copper plate flat, it should be separated from the metal holder and masking tape very carefully. The reason that double sided masking tape was used for mounting is that allows easy removal of the copper plate. It is enough to hold it under the water tap and use a blade to separate the copper plate.

8.3.2. Lithography and Mold Fabrication

After polishing, the copper plate should be washed well to become ready for the lithography step. It should be washed by DI water and liquid soap, and then acetone and then isopropanol, and again DI water.

For making the mold, Megaposit SPR 220-7.0 photoresist from Shipley (now Rohm and Haas Company) was used. This is a positive photoresist and adheres to copper surface very well and resists the copper electroplating solution. Films as thick as 10 μm can be made with this photoresist in a single spin and with good uniformity. However, thicker layers were desired for the microchannels to investigate the copper plating

process in this thesis. With double spinning of SPR 220-7.0 photoresist a film thicker than 20 μm and with very good side walls was obtained. Here are the details of this double spin lithography process:

1. Spin the first layer of photoresist for 30 seconds at 1500 rpm with a 5 second acceleration time.
2. Softbake for 60 seconds at 110°C and with a 100 second ramp. This step for a single layer of photoresist is 90 seconds at 115°C. But because two layers are spun, and the Softbake step will be done twice, each time it is done for a shorter period and at a lower temperature.
3. Spin the second layer of photoresist for 30 seconds at 1500 rpm with a 5 second acceleration time.
4. Second softbake for 60 seconds at 110°C and with a 100 seconds ramp.
5. Exposure for 10 minutes using i-line ABM mask aligner. The normal exposure time is much shorter for a thin layer of this photoresist, but for this thick layer 10 minutes is needed. Several shorter exposure times were tried, but after the developing step a thin layer of photoresist still remained on the substrate surface.
6. Leave the sample in the air for at least 4-5 hours to absorb humidity.
7. Post exposure bake for 30 seconds at 90°C in the oven. This step is very short because the photoresist layer is thick and if this step takes more than 2 minutes, it will crack.
8. Developing for 7 minutes by hand using Microposit 452 developer from Shipley.

8.3.3. Copper Electroplating Process

Microchannel heatsinks require tall and high aspect ratio electroplated structures. The problem with plating a thick layer of copper is that the plated layer, if not plated with very special method, has a lot of residual stress and it peels off after a certain thickness. Generally when a thick plated metal layer is needed, usually it is made by electroplating of nickel, since nickel plated with DC electroplating has low residual stress. However copper is desired for heatsinks due to its high thermal conductance. Hence a method to plate a thick layer of copper with minimum stress and good quality has to be found.

8.3.3.1. Theoretical Background

In Figure 8-11 the schematic of an electroplating bath is depicted. A solid pure metal source called anode is used to provide the metal ions into the solution. To do so, a positive voltage source is connected to this anode in order to draw electrons and produce these positive metal ions. These metal ions travel through the electroplating solution and are attracted to the negative voltage electrode, called cathode, and deposit there.

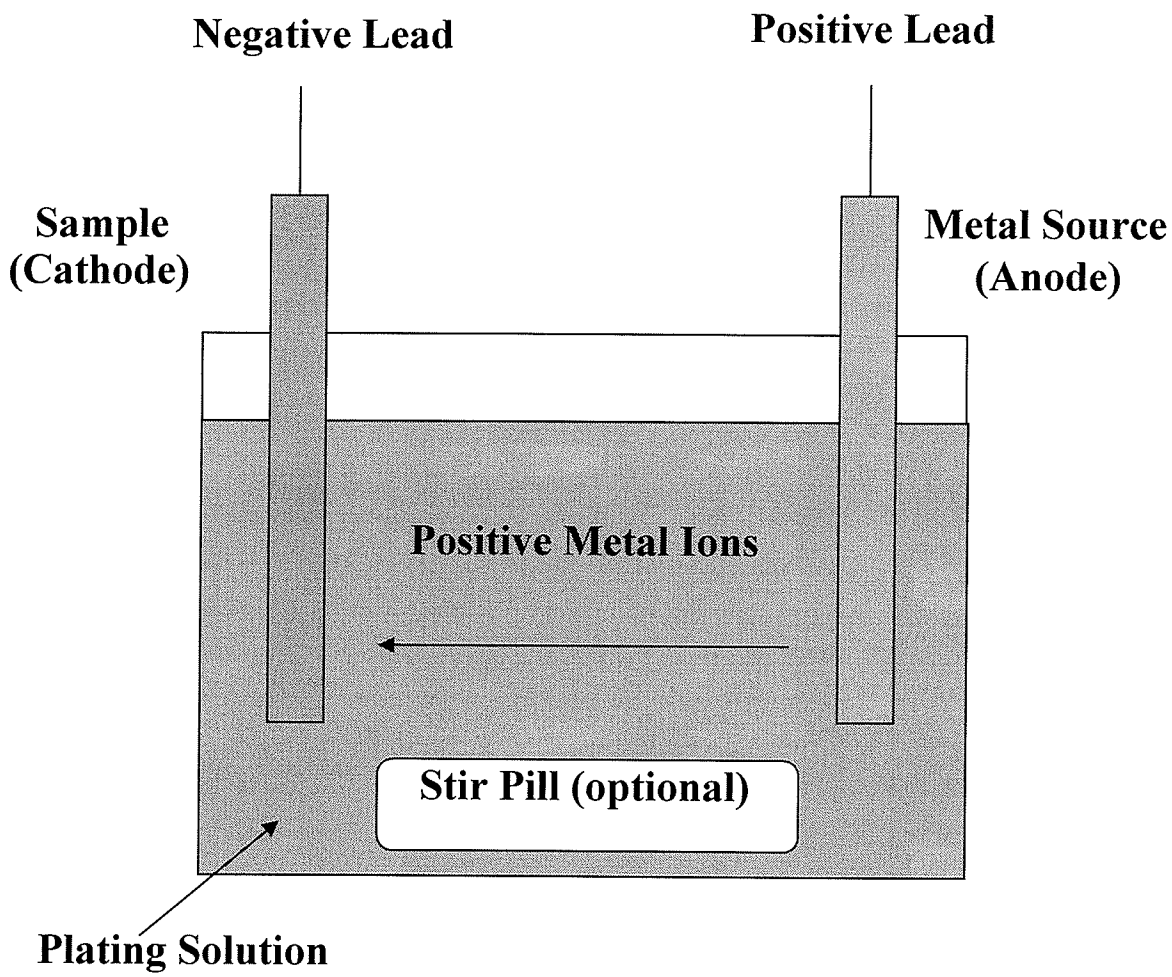

Figure 8-11. The schematic of an electroplating bath.

The following reactions happen at the anode and cathode:

Anode: $Cu \rightarrow Cu^{2+} + 2\,e^{1-}$

Cathode: $Cu^{2+} + 2\,e^{1-} \rightarrow Cu$

A profile of the concentration of the ions in the electrolyte during electroplating is illustrated in Figure 8-12. The distance between the electrodes is assumed to be $2L$. A current density of $i = i(t)$ is assumed to be carried by a single type of carrier (ions) in

which its local time-dependent concentration between the electrodes is $C(z,t)$. The model is described by the diffusion of carriers, or the so-called Fick's second law [61]:

$$\frac{\partial C}{\partial t} = D\frac{\partial^2 C}{\partial z^2} \tag{8-1}$$

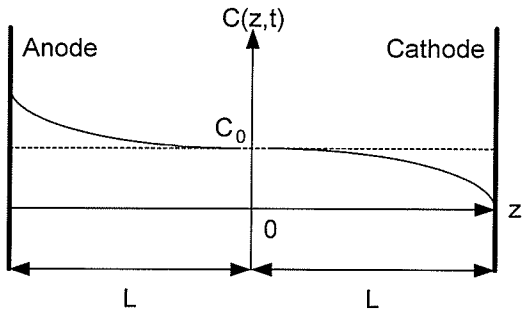

Figure 8-12. The profile of current density between electrodes in the simple electrolytic cell.

The electric current density generally results from two different mechanisms similar to the carrier transport in semiconductors [61]. The first mechanism is based on the local density imbalance of carriers producing a net diffusion current. This current can be estimated by Fick's first law. The next mechanism is the drift of carriers resulting from the local electric field. Therefore, the total current can be found by summing up these two terms as:

$$i = -nFD\frac{\partial C}{\partial z} + \mu enCE \tag{8-2}$$

where D is the diffusion constant, n is the valence of ions, F is the Faraday constant, E is the electric field, μ is the mobility of ions and e is the unit electronic charge. The

accuracy of this diffusion model for prediction of the concentration of reacting species at the electrode surface under pulsed current analysis has been established in [62].

When the electrode is placed into the electrolyte solution, a structure called electrical double layer is formed on the surface of the electrode. This structure consists of two parallel layers of ions. One layer is the surface charge on the surface of the electrode. The other layer consists of the free ions with opposite charge gathered in the liquid very close to the electrode surface screening the first layer. The net charges of these two layers are equal to each other, hence the total charge of the double layer structure is neutral. The overall result is two layers of charge (the double layer) and a potential drop which is confined to only this region

The electrode double layer consists of charged ions of opposite polarity and they scatter the charged carriers through coulomb collisions. Hence the diffusion process dominates the transport near the electrodes (for discussion on a method for determination of the thickness of this layer refer to [63]). Since the electrode double layer reduces the mobility of carriers considerably, it is assumed that the drift term is about zero near the electrodes. Then from relation (8-2) the following boundary conditions are obtained:

$$D\left.\frac{\partial C}{\partial z}\right|_{Z=-L} = D\left.\frac{\partial C}{\partial z}\right|_{Z=L} = -\frac{i}{nF} \tag{8-3}$$

The model becomes complete with the addition of Butler-Volmer kinetics [61]:

$$\mathbf{i}\cdot\mathbf{n} = I_0\left[\exp\left(\frac{-\alpha_a nF\eta}{RT}\right) - \exp\left(\frac{\alpha_c nF\eta}{RT}\right)\right] \tag{8-4}$$

Here, $\mathbf{n}$ is the vector normal to the electrodes, α_a and α_c are the transfer ratios of anode and cathode, R is the universal gas constant, T is the absolute temperature, I_0 is the exchange current density, and η is the overpotential. The overpotential is an

electrochemical term which refers to the potential (voltage) difference between a half-reaction's thermodynamically determined reduction potential and the potential at which the reduction-oxidation reaction is experimentally observed. In an electrolytic cell the overpotential requires more energy than thermodynamically expected to drive a reaction [64]. Numerical values for the parameters introduced in (8-3) and (8-4) may be found in [65] for the acid-copper bath.

A good electro-deposited layer is characterized with some qualitative features such as uniformity, adhesion, low porosity, low residual stress, and brightness [66]. One of the most important issues in obtaining a good film is that the electrolytic processes should not be in the transport limited regimes. Usually, due to low ion transport velocity, there is lack of ions at the cathode. More exactly, the electrode diffusion layer limits the rate of carrier transport, and thus several features of the deposit are affected. In order to obtain better deposition, usually the thickness of the electrode diffusion layer has to be reduced. There are several methods to achieve this goal.

1. Use DC electroplating and stirring the solution constantly. Any kind of perturbation reduces the diffusion layer thickness or even can terminate it.
2. One of the major non-steady methods is to apply an alternating current (AC) sinusoidal voltage to electrodes instead of a direct current (DC) voltage. This signal should have an offset value and its frequency can be in a wide range from tens of Hertz to few hundreds of kilo Hertz. It can be much more that one hundred kHz, because the relaxation time of the ions in the electrolyte doesn't permit it.

3. Use a shaped pulsed signal. The input voltage can be a wide range of pulse shapes with a non-zero average, and a frequency between several tens of Hertz and hundreds of kilo Hertz. This is the method that is used in this work for electroplating of copper.

Pulse-plating has found application in plating of alloys [67], thin films [68], and even decorative coatings [69]. In the pulse-plating process, general improvements in the quality and hardness of the plates have been reported [70]. Several studies have addressed the time-dependent carrier concentration and transport in pulse plating methods for some basic waveforms [71], using the simple diffusion model reported in [72]. For this method mass transfer requirements are addressed in [73]. It has been observed that the bath's efficiency (The ratio of the useful electric current carried by deposited ions to the total transferred charge in positive and negative cycles of current) may also decrease under pulse periodic plating [74].

There are many papers in the literature about pulse plating of copper [75]. It is well known that pulse reverse current electroplating is the best method for plating a thick layer of copper [76]. Current is applied as the input signal and is monitored as the control parameter rather than voltage. The reason is that since current is linearly proportional to the number of deposited ions, and so by monitoring current it is much easier to control the transferred mass. The current passing through the anode and cathode is very sensitive to the applied voltage and the I-V characteristic of the electroplating bath is highly nonlinear. Hence, it is better to monitor current instead of voltage signal.

In industry, usually various organic and inorganic ingredients are also added to the electrolyte solution to improve the quality, uniformity and speed of plated layer and plating. However in [77] it is shown that these additives are effective only in DC plating, and they don't have so much benefit in pulse reverse plating.

Let us assume that the current has an arbitrary pulse shape shown in Figure 8-13. The period of signal is denoted by T and the forward and reverse amplitudes are given by A_r and A_f. These relations and definitions about this pulse shape signal should be considered:

$$T = 1/f = t_f + t_r \tag{8-5}$$

$$\text{Duty cycle} = t_f / T \tag{8-6}$$

$$I_{P\text{-}P} = A_f + A_r \tag{8-7}$$

$$I_{av} = (A_f t_f - A_r t_r) / (t_f + t_r) \tag{8-8}$$

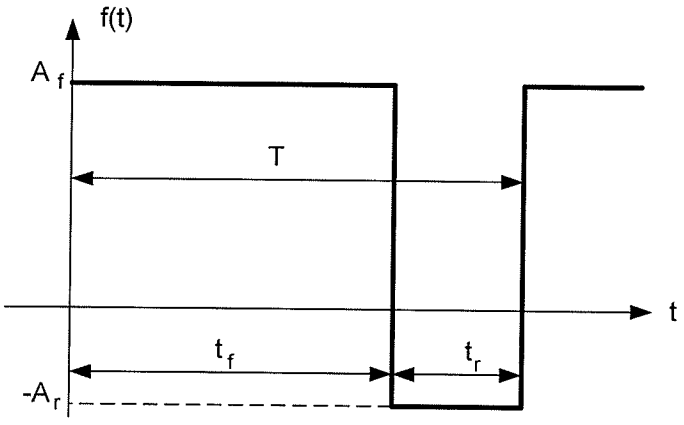

Figure 8-13. Electric current waveform and the parameters.

In [78] the effect of changing the parameters of this pulse waveform on the concentration of ions at the cathode is studied mathematically and experimentally, and it is revealed that the best pulse shape for the best quality of plating is when a small forward current for the most of the period, and a large reverse current for a short time are applied [79]. In other words, the reverse current should consist of sharp and narrow pulses.

This has been shown experimentally [80] and this method is used in industry for electroplating thick layers of copper [81]. An explanation of this result is that this sharp pulse of reverse current separates the weakly plated ions on the cathode, and leaves the strongly held ions, and this causes the good quality of the plated layer.

8.3.3.2. Experimental Work and Results

The set up of the electroplating system is shown in Figure 8-14. The system consists of a large bath containing the electrolyte and placed on top of a magnetic stirrer. The anode and cathode are supported in the solution by two metal holders which are electrically isolated from their bases. The distance between the anode and cathode and their position related to each other is an important parameter. In these experiments the distance between the anode and cathode is kept in the range of 4-10 cm. The distance between the anode and cathode and their sizes affects the hydrodynamics of the electrolyte solution, the electric field around anode and cathode and between them, and ultimately ion transfer. Therefore, the distance between the anode and cathode, and their sizes, affect the quality of the plated layer. If the distance between them is too small, the electric fields and ion migration will not be normal to the plated substrate and the liquid

between the electrodes will not be perturbed enough by stirring. If the distance is too large, the rate of ion transfer between the electrodes will decrease. An experiment was done to test the quality of plating with the distance of about 20 cm and the plated layer was rougher than plating with 4-10 cm distance between the electrodes.

A very pure 99.999 % copper foil bought from Sigma-Aldrich was used as the anode and a copper sulphate based solution as the electrolyte. The solution was made by using the following method: 50g (0.2 mol) of copper sulphate ($CuSO_4.5H_20$) is put in a big beaker. One litre DI water is added to it. 100 ml of H_2SO_4 98% is added and enough DI water is added to it to bring the total volume to 2 litres. The ratios for this 0.1 molar solution of $CuSO_4$ were obtained from literature [82].

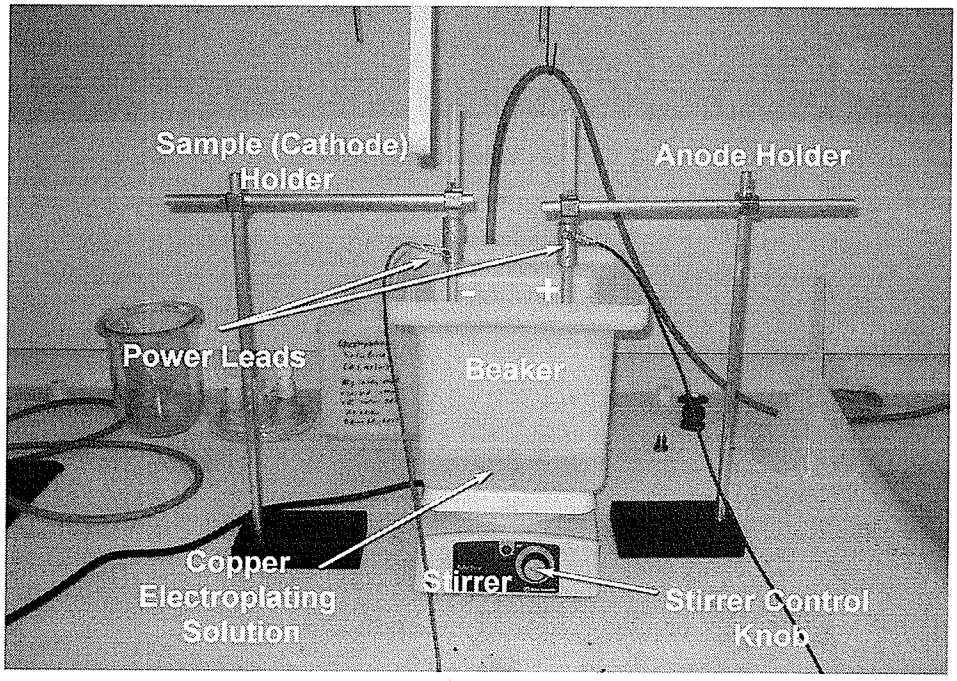

Figure 8-14. Copper electroplating bath.

The pulse current generating system can be seen in Figure 8-15. This system includes three parts. First is a voltage pulse generator. This instrument can generate voltage pulses with the duty cycle of 10 – 90 % and with variable amplitude. The second part is a current source circuit which converts that voltage pulse to current pulse. The schematic of this circuit is shown in Figure 8-16 and its photo is shown in Figure 8-17. The output of this circuit is a current pulse with forward and reverse current. The amplitude of each of these forward and reverse currents can be varied, and the duty cycle depends on the duty cycle of the input voltage pulse. The output of this circuit is single ended and each of the forward and reverse currents can be adjusted by 100 Ω potentiometers. This circuit can generate current amplitude of 1A and mean current of 100 mA.

The voltage at the output of the circuit is monitored using an oscilloscope. This voltage was proportional to the output current. By reading the peak-to-peak and average values of the voltage signals on the oscilloscope, the peak amplitudes of the forward and reverse currents were calculated. In order to simplify this calculation, and since the impedance of the electroplating system is not fixed (it depends on several parameters like the composition of the solution, sizes of the anode and cathode and their distance, and the applied current), a small 1 Ω resistor was put in series with the electroplating bath. Using this resistor the numbers shown on the screen of the oscilloscope for "voltages" are the same as the values of the currents. For example for the signal shown in Figure 8-18, the average current is 41.22 mA and the peak-to-peak current is 140 mA.

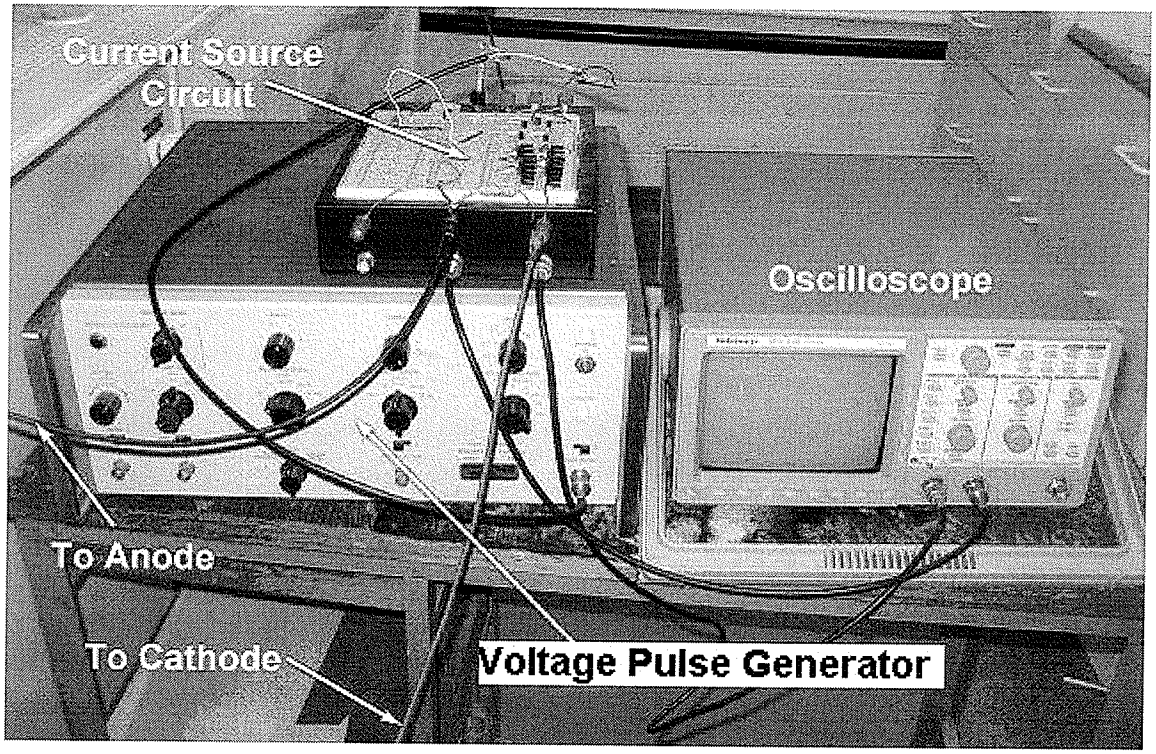

Figure 8-15. Pulse current generator and signal monitoring system.

The plating process started from the moment that the pulse current was applied to the electrodes. The quality of the first deposited layers is very important. Hence there is no time to set up and adjust the signal parameters values and it is important to adjust the values of the pulse current before connecting it to the electroplating bath. The resistance of the electroplating bath was measured to be in the range of 5 – 30 Ω depending on the bath parameters. A high power 20 Ω resistor was used to adjust the current. First it was put at the output of the pulse current generating system and the values of the signal were adjusted. Then it was removed and the current signal generator output was connected to the anode and cathode. Since this is a current generator, and the current value is almost independent from the output impedance, the output current will remain unchanged, despite the small change in the output impedance.

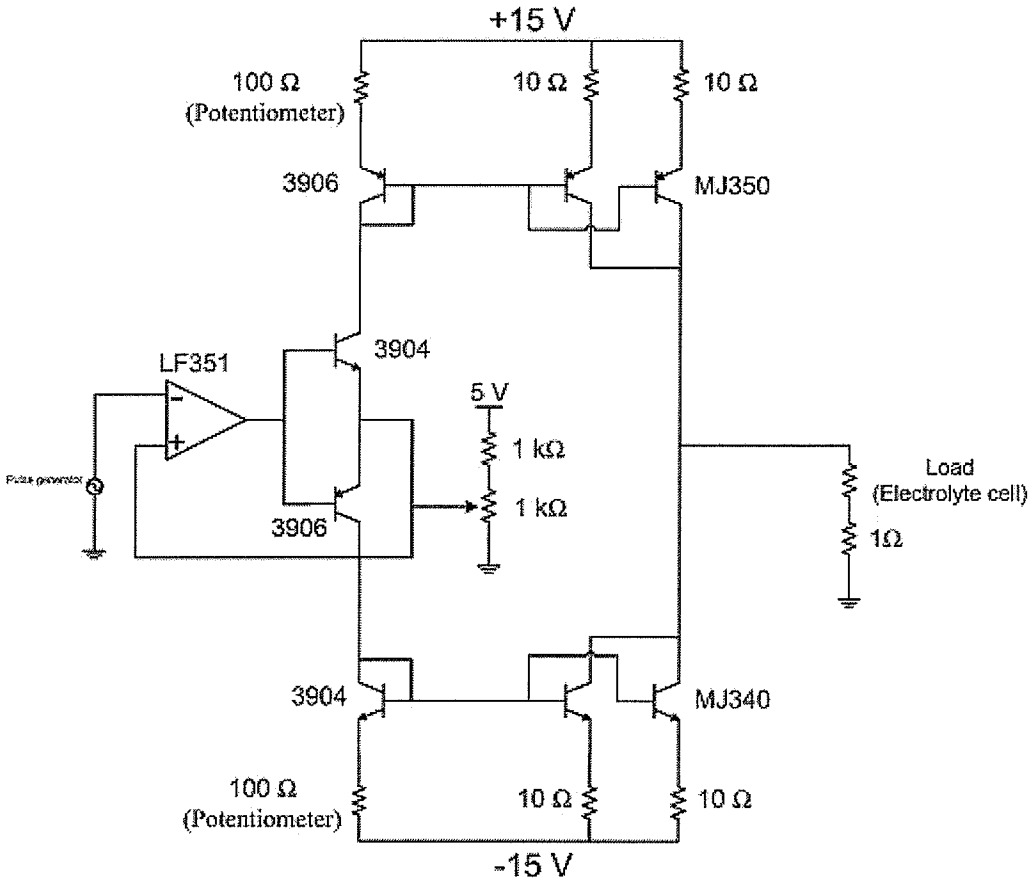

Figure 8-16. The circuit used for generation of current pulse for electroplating.

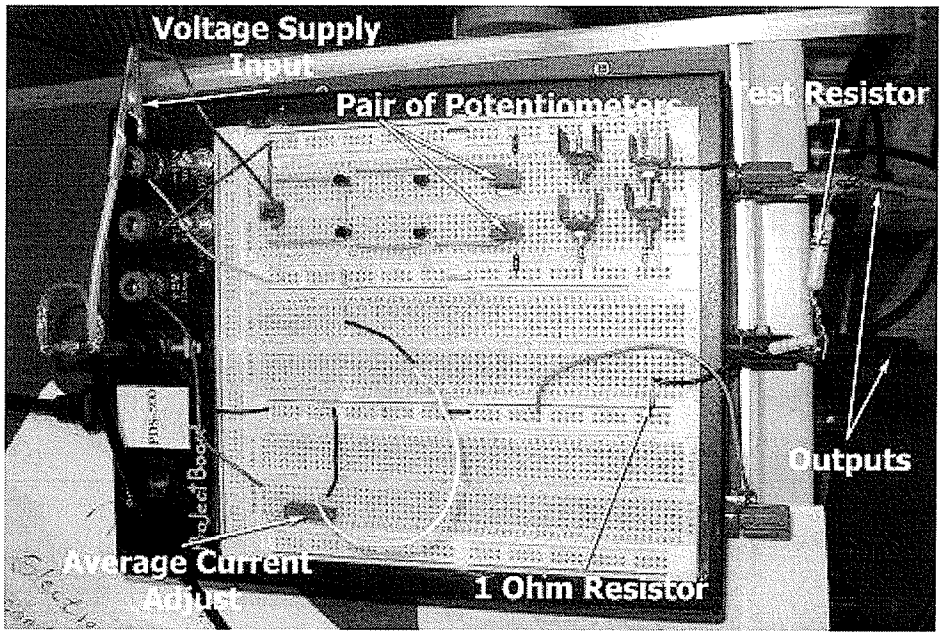

Figure 8-17. Pulse current generating circuit.

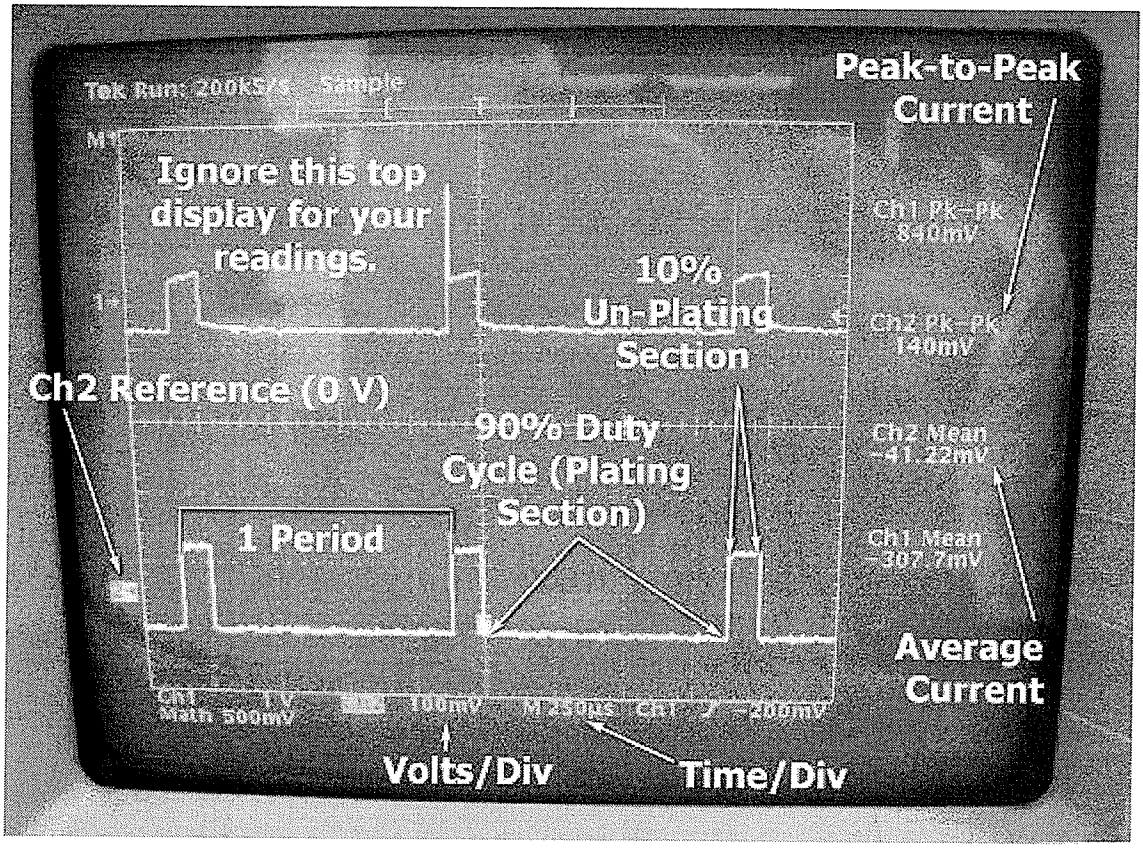

Figure 8-18. Pulse current signal used for copper plating. It consists of a small forward current a sharp pulse of reverse current.

After setting up the electroplating system, the important step was to optimize the input signal parameters. There were four parameters that had to be optimized: peak-to-peak current and average current (or amplitudes of the forward and reverse currents), duty cycle, and frequency. There are other parameters related to the electroplating bath like the distance of the anode and cathode, and the stirring rate.

For test plating of copper, the structure shown in Figure 8-19 is used. It consists of a seed layer of 2×2 cm area on a glass plate. This area is connected through a narrow tail to a contact area. Only the 2×2 cm area is dipped into the electrolyte solution and copper is electroplated on it.

Copper is plated on this structure and parameters such as peak-to-peak current, average current, frequency, duty cycle and stirring rate were changed to find the best conditions. For each case, the deposited film's average roughness and peak roughness were measured. These parameters depended a little on film thickness. Hence, all cases were done at the thickness of about 3 μm. The results are summarized at Tables 8-2 to 8-4.

It is important to note that the quality of the plated layer highly depends on the fluid dynamics of the electrolyte solution. This means that the distance between the electrodes, their position and direction toward each other, and the way the solution is stirred and flows over the surfaces of the electrodes all affect the quality of the plated layer.

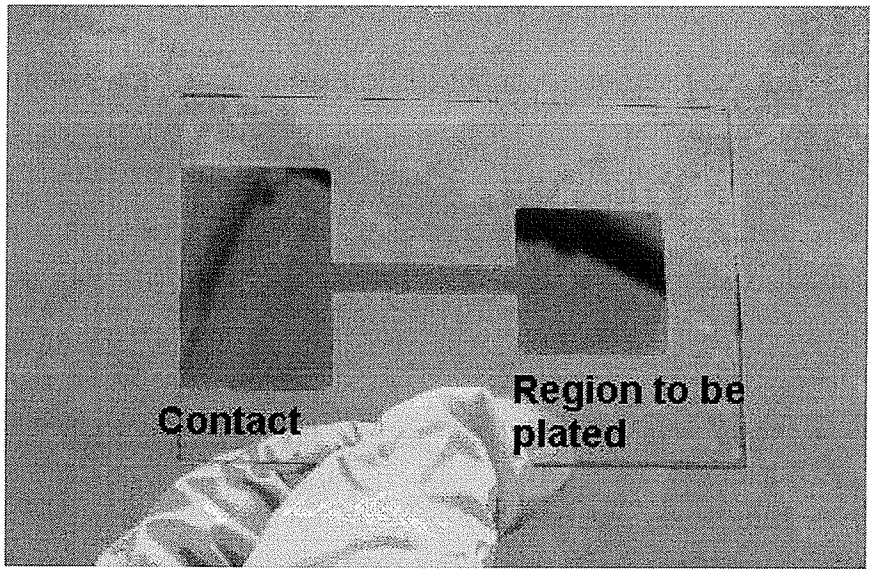

Figure 8-19. A structure containing a 2×2 cm area of seed layer used for test plating of copper. This area is connected through a narrow tail to a contact area for connecting electricity.

From preliminary tests (Table 8-1) it was found out that the frequency of 1 kHz and duty cycle of around 80 % or more are the best values. Hence the data collected in tables 8-2 to 8-4 are from the tests performed in these conditions. In these tables RA indicates the average roughness and TIR indicates the peak roughness of the surface.

Table 8-1. Preliminary electroplating tests.

	I_{Av} (mA)	I_{P-P} (mA)	Duty Cycle	Frequency (kHz)	Thickness (μm)	Spinning Speed (rps)	R_A (nm)
1	45	100	50 %	1 kHz	30	1	900
2	45	160	50 %	10 kHz	40	1	800
3	40	200	50 %	50 kHz	33	1	750
4	20	160	70 %	10 kHz	30	1	450
5	35	140	75 %	100 Hz	41	2	400
6	35	140	75 %	10 kHz	32	2	500
7	40	160	75 %	1 kHz	64	2	600
8	40	160	80 %	1 kHz	23	1	100

Table 8-2. Metal: Copper, Area: 2×2 cm, Frequency: 1 kHz, Duty Cycle: 90 %, Spinning speed: 4 rps.

		I_{AV}, Average Current (mA)								
		20 (20 minutes)			**40 (10 minutes)**			**80 (6 minutes)**		
I_{P-P} (mA)	**200**	Thickness 3.2 μm	R_A 373.3 Å	TIR 3511 Å	Thickness 3.0 μm	R_A 237.5 Å	TIR 2876 Å	Thickness 2.8 μm	R_A 285.2 Å	TIR 3127 Å
	300	Thickness 3.2 μm	R_A 503.2 Å	TIR 6727 Å	Thickness 2.9 μm	R_A 281.9 Å	TIR 2576 Å	Thickness 3.0 μm	R_A 231.1 Å	TIR 2842 Å
	400	Thickness 2.9 μm	R_A 690.0 Å	TIR 5416 Å	Thickness 3.0 μm	R_A 451.9 Å	TIR 5396 Å	Thickness 3.2 μm	R_A 611.7 Å	TIR 6236 Å

Table 8-3. Metal: Copper, Area: 2 × 2 cm, Frequency: 1 kHz, Duty Cycle: 90 %, Spinning speed: 2 rps.

			I_{AV}, Average Current (mA)					
			20 (20 minutes)			**40 (10 minutes)**		
I_{P-P} (mA)	**120**	Right Side	Thickness 2.86 μm	R_A 272.2 Å	TIR 1674 Å	Thickness 3.23 μm	R_A 374.2 Å	TIR 2781 Å
		Left Side	Thickness 2.29 μm	R_A 183.4 Å	TIR 1316 Å	Thickness 1.98 μm	R_A 111.0 Å	TIR 1105 Å
	200	Right Side	Thickness 2.90 μm	R_A 280.1 Å	TIR 1917 Å	Thickness 3.27 μm	R_A 440.5 Å	TIR 5203 Å
		Left Side	Thickness 2.58 μm	R_A 248.8 Å	TIR 2975 Å	Thickness 2.10 μm	R_A 169.8 Å	TIR 1727 Å

From Table 8-2 it can be inferred that I_{p-p} = 300 mA and I_{av} = 40 mA or 80 mA are the best conditions when the spinning rate is 4 rps. From Table 8-3 it is observed that I_{p-p} = 120 mA and I_{av} = 20 mA are the good conditions when the stirring rate is 2 rps. In this table it is seen that there is a difference between the roughness of the plated layer on the right and left side of the 2×2 cm area. From Table 8-4 it is observed that stirring the solution during electroplating is better than not stirring it, and the signal frequency of 1 kHz is better than 100 Hz and 10 kHz.

Table 8-4. Metal: Copper, Area: 2×2 cm, Time: 10 minutes, I_{AV} = 40 mA, I_{P-P}= 120 mA.

		Spinning Speed (rps)					
		0			1		
#14-15 **Duty Cycle: 90% Frequency: 1kHz**	Right Side	Thickness 2.99 µm	R_A 5757 Å	TIR 3.78 µm	Thickness 3.10 µm	R_A 277.0 Å	TIR 2192 Å
	Left Side	Thickness 2.70 µm	R_A 6269 Å	TIR 3.93 µm	Thickness 2.46 µm	R_A 169.5 Å	TIR 1477 Å
#16 **Duty Cycle: 90% Frequency: 100Hz**	Right Side	N/A			Thickness 3.38 µm	R_A 403.3 Å	TIR 2852 Å
	Left Side				Thickness 2.80 µm	R_A 338.2 Å	TIR 2955 Å
#17 **Duty Cycle: 90% Frequency: 10kHz**	Right Side	N/A			Thickness 3.34 µm	R_A 300.2 Å	TIR 1823 Å
	Left Side				Thickness 2.83 µm	R_A 221.6 Å	TIR 2331 Å
#18 **Duty Cycle: 70% Frequency: 1kHz**	Right Side	N/A			Thickness 2.65 µm	R_A 211.5 Å	TIR 1465 Å
	Left Side				Thickness 2.21 µm	R_A 148.5 Å	TIR 1560 Å
#19 **Duty Cycle: 99% Frequency: 1kHz**	Right Side	N/A			Thickness 2.44 µm	R_A 177.8 Å	TIR 1536 Å
	Left Side				Thickness 2.77 µm	R_A 189.9 Å	TIR 1647 Å
#20 **Duty Cycle: 99% Frequency: 1kHz**	Right Side	N/A			Thickness 2.88 µm	R_A 269.6 Å	TIR 2277 Å
	Left Side				Thickness 2.36 µm	R_A 179.0 Å	TIR 1864 Å

The interesting finding was about sample #19 in Table 8-4 which by mistake the back of the cathode plate was put in a way that it was facing the anode, and surprisingly the roughness of the plated copper layer was still very good for this case.

Using reverse current pulse electroplating, it was possible to plate high quality and low stress copper layers with the thickness of 150 μm. Plating conditions that were selected for this test were: I_{P-P} = 120 mA, I_{av} = 40 mA, frequency = 1 kHz, duty cycle = 90 %, and stirring rate = 2 rps. The images of the surface of this electroplated layer taken by Atomic Force Microscopy (AFM) are shown in Figure 8-20.

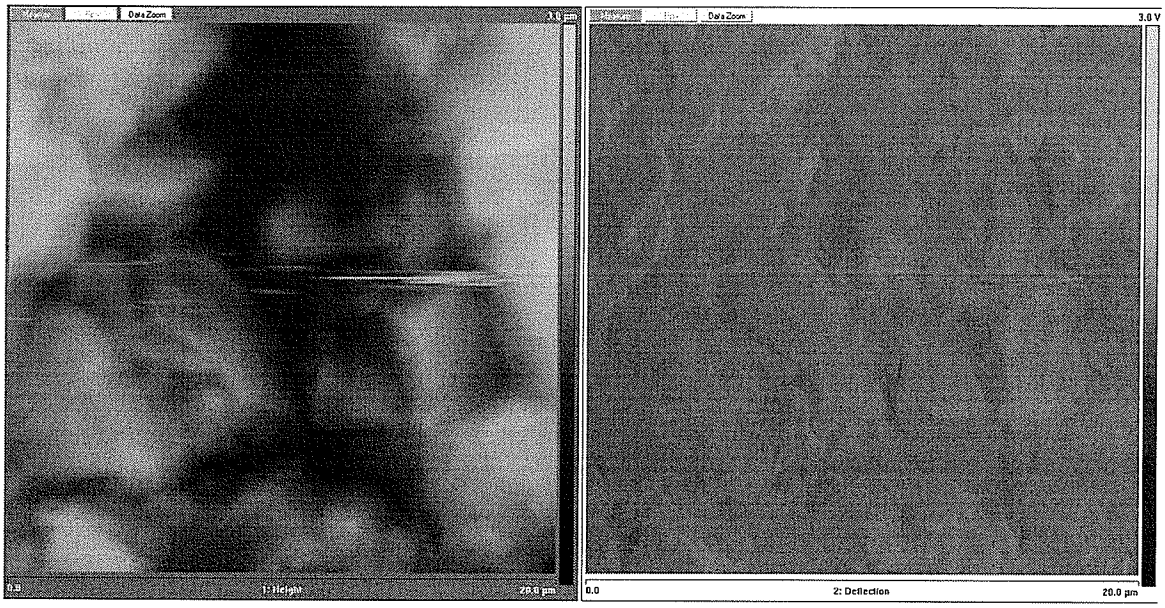

(a)

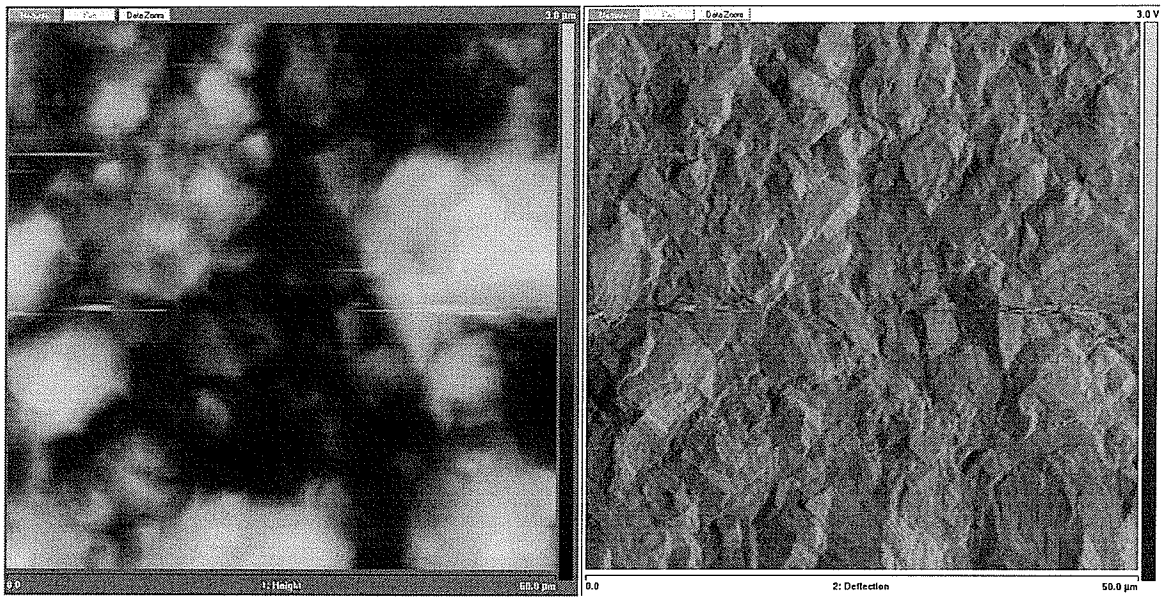

(b)

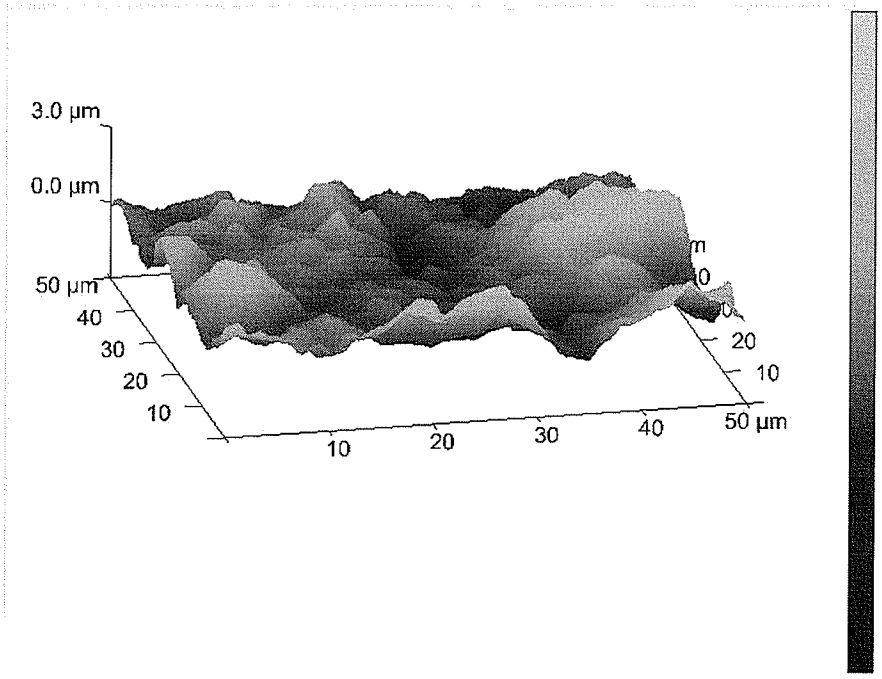

(c)

Figure 8-20. The AFM images of the surface of the 150 µm thick electroplated copper layer. (a) The image of a 20 × 20 μm^2 area. (b) The image of a 50 × 50 μm^2 area. (c) The 3D image of a 50 × 50 μm^2 area.

Adhesion Testing:

The plated copper layer appeared firmly attached to the substrate. A tape test was performed to test adhesion. In this test a piece of scotch tape is attached to the deposited layer and then the tape is detached. This applies a large force to the deposited layer interface with the substrate. If the layer was not detached from the substrate and did not come off with the tape, it was concluded that it has a good adhesion to the substrate. Of course this test is not a very good quantitative measurement and the result of this test depends on the tape adhesion strength and how it is taken off. The plated copper layer passed the tape test.

Thermal Conductivity Test:

As explained in chapter 1, thermal energy is transferred in metals primarily by electrons, which is contrary to insulators where heat is transferred by phonons, or lattice vibrations. Hence, copper's heat conductance can be estimated by measuring its electrical conductance and comparing it to the electrical conductance of bulk copper. For this purpose, a long resistor shown in Figure 8-21 was fabricated by electroplating copper on a glass substrate. The resistance of such a resistor is related to its length and cross-section area according to equation 8-9.

$$R = \rho_R \frac{L_R}{A_R} = \rho_R \frac{L_R}{T_R W_R} \tag{8-9}$$

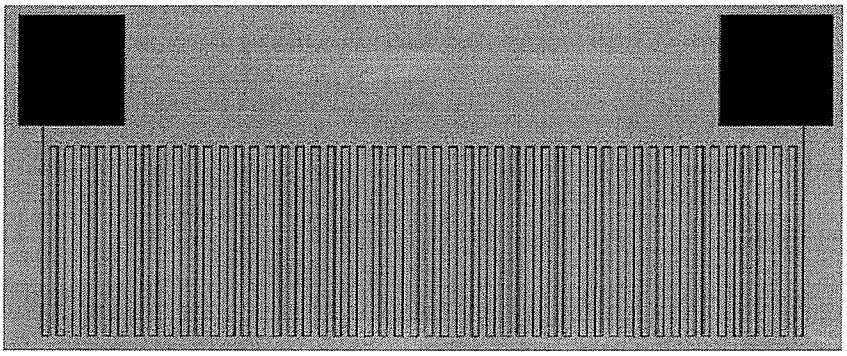

Figure 8-21. Copper resistor fabricated for testing the conductance of the plated copper.

Dimensions of the fabricated resistor are:

Resistor length $L_R = 104.2$ cm

Resistor width $W_R = 100$ μm

Resistor thickness $T_R = 11$ μm

The resistance of the resistor is measured by a multi-meter:

Measured Resistance = 16.6 Ω

Hence from equation 8-9 the resistivity of the fabricated resistor is calculated:

$\rho_R = 1.752 \times 10^{-8}$ Ωm

Resistivity of bulk copper is $\rho_R = 1.724 \times 10^{-8}$ Ωm. Hence theoretical value for R calculated from equation 8-9 would be 16.33 Ω. Percentage of difference between the experimental value and theoretically expected value is 1.6 %.

The electrical conductance of the plated copper layer was measured, and was found to be almost the same as that of bulk copper. If the heat conductances of thin film and bulk copper have exactly the same ratio of electrical resistivities with each other, the

thermal conductance of the plated copper may be calculated as k_{Cu} = 394.6 W/mK, while the thermal conductance of the bulk copper is k_{Cu} = 401 W/mK. This shows that most probably the copper plated by this method has a good heat conductance, close enough to the bulk copper.

8.3.4. Bonding and Sealing

A cover plate on the channels can be bonded to the microchannels layer by different methods. Both plates should be conformally in contact with each other at every point of their surfaces. The bonding has to be strong enough to resist the fluid pressure, and change of temperature in the range of approximately 20 – 120 °C (This range depends on the surface which has to be cooled). Several bonding methods can be used.

1. **Diffusion Bonding:** When both sides are metal, diffusion bonding can be used. In this method, two metal surfaces are brought into contact with each other and are kept under high temperature (800 - 1000°C) and pressure for several hours (e.g. 7-8 hours). The problem of this method is that it needs very high pressure and temperature [83].
2. **Eutectic Bonding:** Eutectic bonding also requires relatively high pressure and temperature (but less than diffusion bonding), depending on the materials of the surfaces being bonded to each other. This type of bonding uses the concept of eutectic mixture. For some alloys the melting point of certain mixture ratios is lower than the melting point of each of the materials individually. This lower melting point is called the eutectic temperature [84]. It Table 8-5 the eutectic

temperatures of some materials are listed. As observed, the eutectic temperature for each pair of materials is less than the melting point of each of those materials.

Table 8-5. Eutectic temperatures of some materials.

Materials	**Eutectic Temperature**
Al and Si	577 °C
Au and Si	363 °C
Al and Cu	548 °C
Al and Ag	566 °C
Cu and Si	802 °C
Ag and Si	835 °C

In Eutectic type bonding, two surfaces are brought into contact with each other, pressed together, and then are held at elevated temperature above their eutectic temperature for a few hours. The materials at the interface alloy and make a firm bond. The problem of this method is that it needs a relatively high temperature. Gold-silicon eutectic bonding which happens at 363 °C, however is not strong enough [47].

3. **Adhesive Bonding:** Adhesive bonding uses an intermediate layer of polymer or other material to "glue" two substrates to each other [84]. This method likely is not suitable for cooling applications, due to the high temperatures that the heatsinks need to operate in, which may affect the chemical composition of the adhesive layer and degrades the bond.
4. **Solder Bonding:** Bonding using a solder. A layer of tin was selected for bonding two copper substrates. For many years tin, due to its low melting point and its

good adhesion to copper and other metals, has been used for soldering. Usually lead is also mixed with tin to reduce its melting point. In this thesis, tin solder bonding was used.

As observed in Figure 8-7, a very thin layer of tin is deposited on each plate by electroplating. Tin can be deposited by sputtering or thermal evaporation as well. Plating was selected since chemicals are inexpensive. After tin plating the substrates are placed together and high pressure is applied with a temperature a little higher than the melting point of tin (232 °C). Some experiments were done to find out the best conditions and parameters for electroplating of tin and bonding the plates.

These experiments showed, for tin, DC electroplating is better than pulse electroplating and gives a smoother and shinier surface. An important point about electroplating of tin is that the substrate's surface must be very clean. The polished copper plates had to be washed with a soft sponge using Sparkleen powder, and DI water mixture for at least 3-5 minutes, followed by DI water rinse for 5 minutes. Otherwise during plating, the tin didn't stick well to the substrate. It was also observed that if a very thin layer of copper was deposited by electroplating before the tin, then even without the 5 minute washing period, the tin adheres to the substrate, and was deposited on it, with good quality. It was observed that etching the copper substrate in chrome etch solution (which is normally used for slow etching of copper) for 45 seconds didn't improve the tin adhesion to the substrate. It was not desired to leave the copper substrate for a longer time in the chrome etch solution, because it would roughen the substrate.

After preparing the substrate, a thin layer of tin is electroplated on the plate's surface. For this purpose the tin plating solution and tin anode included in "Plug N' Plate" tin plating kit bought from Caswell Company were used. The tin plating solution is a dilute solution of stannous acid and sulfuric acid. For the copper plates with the area of 3 × 4.5 cm, plating with the total current of 100 mA and for 16 minutes resulted in a tin layer thickness of 2 μm. The plating solution was stirred by a magnetic spinner with the rate of 1 rps. The resulting tin layer is uniform and shiny. Its color turns a little dark in 3-5 seconds after taking it out of the plating solution. This can be due to oxidation of the surface.

After plating the tin layer, the two tin coated copper substrates were placed together, between two polished 1 cm thick aluminum blocks, and were held together using a C-clamp (Figure 8-22). The diameter of the screw of the C-clamp was 3/8 inch and the pitch of its teeth was 1/16 inch and it was made of cast steel. Using a torque wrench they were pressed together. The aluminum blocks were used to apply an even and uniform force on the copper substrates. Then they were placed in an oven and the temperature was increased to few °C higher than the melting point of tin (232 °C).

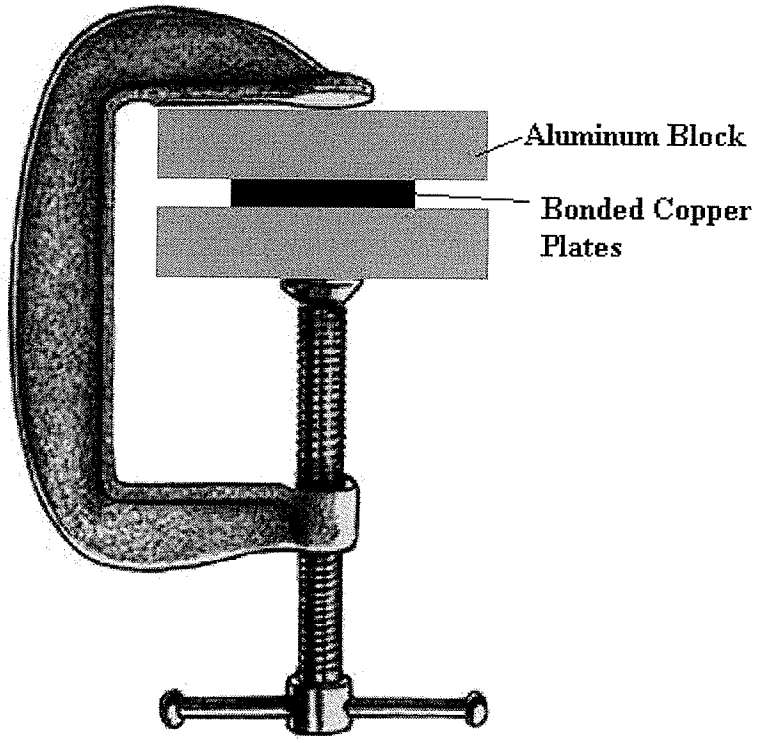

Fig. 8-22. Bonded copper plates held and pressed together by a C-clamp.

Several preliminary experiments were performed at different temperatures, heating times in the oven, applied torque, and tin layer thickness. The conclusion from those preliminary experiments was that for a good bond the tin layer thickness has to be a few microns thick, the bonding temperature has to be above 255 °C, the applied torque has to be around 20 lb/inch^2, and the plates have to be in the oven for a few hours. Three experiments were performed to find the optimum values for these parameters. At the end of this time, plates were left in the oven to cool down gradually over night, and then the clamp was opened.

Trial 1:

Tin layer thickness on each plate: 2 μm.

Bonding temperature: 255 °C.

Bonding time: 1.5 hours.

Torque: 20 lb/inch^2.

Figure 8-23(a) shows the surfaces of the separated copper substrates bonded under these conditions. The substrates were separated by hand, and the tin on the surfaces doesn't look uniform.

Trial 2:

Tin layer thickness on each plate: 2 μm.

Bonding temperature: 260 °C.

Bonding time: 3 hours.

Torque: 20 lb/inch^2.

Figure 8-23(b) shows the surfaces of the separated substrates. The plates were separated by hand, and the tin on the surfaces looks oxidized.

Trial 3:

Tin layer thickness on each plate: 4 μm.

Bonding temperature: 257 °C.

Bonding time: 2.5 hours.

Torque: 20 lb/inch^2.

Substrates were found to be firmly bonded to each other, and although they were separated by hand, much more force was needed to separate them. Figure 8-23(c) shows the plates bonded under the above mentioned conditions. Results of trials 1 and 2 obviously were not as good as the bonds resulting from trial 3. It is suspected that the primary reason that trial 3 had the best result is due to the thicker tin layer used.

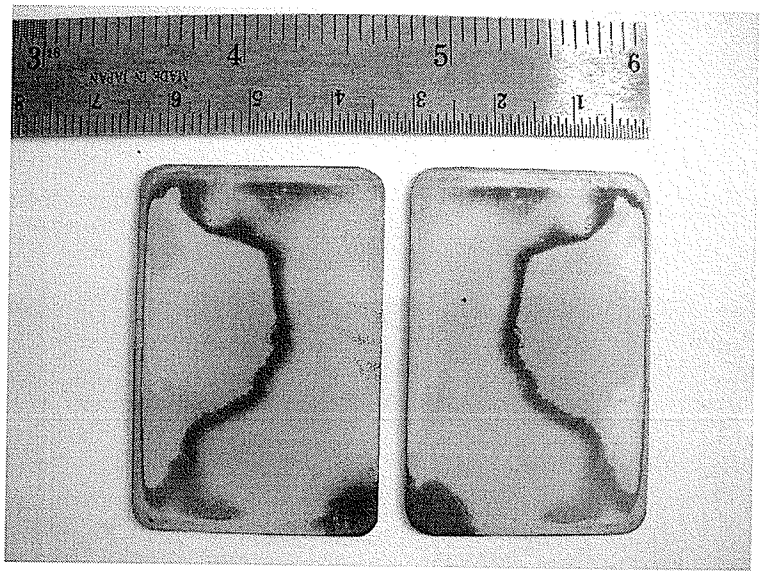

(a)

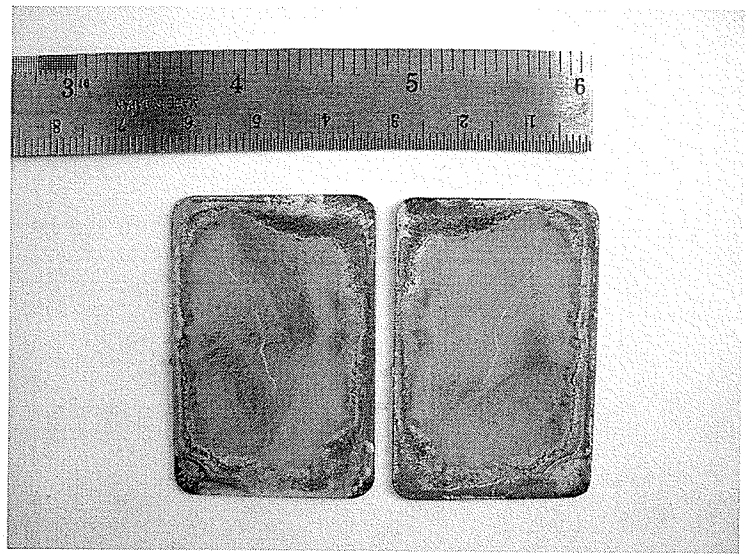

(b)

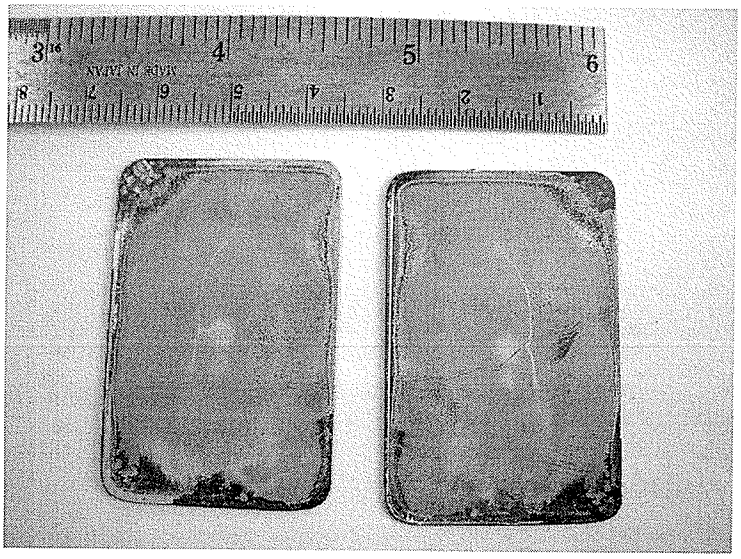

(c)

Figure 8-23. Surfaces of the tin coated copper plates after bonding and separating from each other. (a) Tin layer thickness on each plate: 2 μm, Bonding temperature: 255 °C, Bonding time: 1.5 hours, Torque: 20 lb/inch^2. (b) Tin layer thickness on each plate: 2 μm, Bonding temperature: 260 °C, Bonding time: 3 hours, Torque: 20 lb/inch^2. (c) Tin layer thickness on each plate: 4 μm, Bonding temperature: 257 °C, Bonding time: 2.5 hours, Torque: 20 lb/inch^2. This gave the best result.

Using the bonding conditions of trial 3, a copper substrate on which 20 μm tall copper microchannel structure was electroplated, was bonded to a copper lid plate. Then this structure was glued to a fixture which was made to connect the inlet and outlet to the tubes (Figure 8-24). This was tested by connecting water to the inlet from the water tap in the lab. The pressure of the water in the building was approximately 50 psi. The plates didn't separate, but the structure leaked and water came out through several holes around the structure. It seems that since the tin surface oxidizes very quickly after plating and before bonding, it cannot provide an ideal quality bond. In the microelectronics and optoelectronics industry AuSn is used instead of tin (Sn) for bonding and sealing purposes [85]. This alloy is more expensive and needs special equipment for electroplating of gold and tin in the same solution and at the same time, and so was not considered for this thesis.

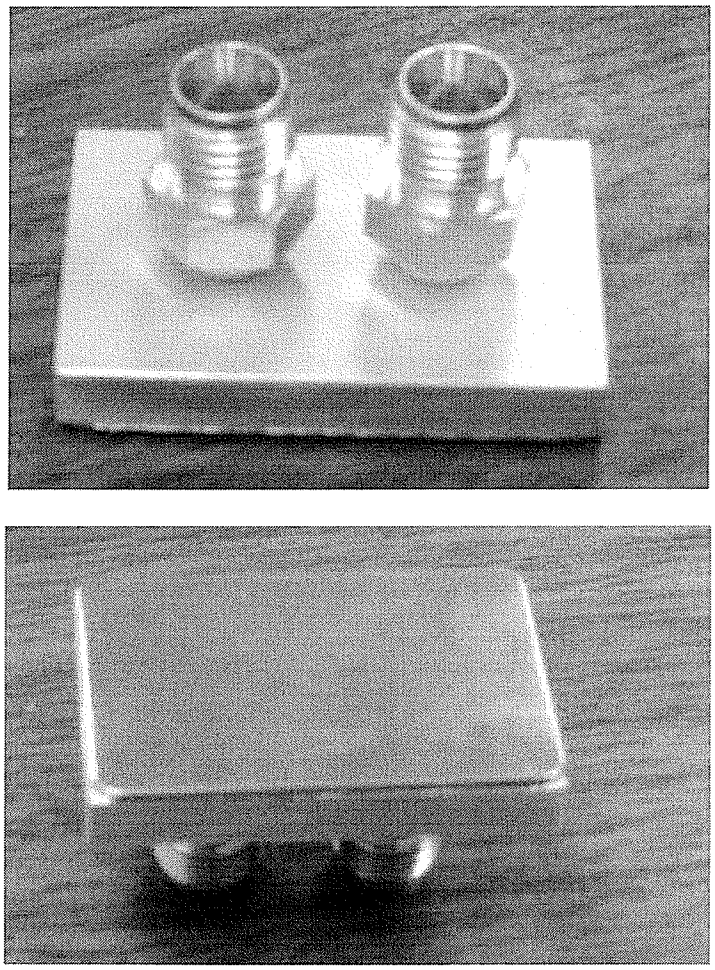

Figure 8-24. The copper heatsink glued to the inlet/outlet fixture.

Measurement of Microchannels after Bonding:

After the device Figure 8-24 was tested, the copper substrate with the plated microchannels was separated from the lid. The height of the 20 μm microchannels was measured with the Alpha-Step profiler, and the microchannels remained 20 μm tall. This indicates that the bonding process did not affect the microchannels.

Chapter 9

Conclusions and Future Work

9.1. Conclusions

In this thesis the effects of material type, fluid velocity, and fluid channel size and separation on the thermal performance of microfluidic heat exchangers have been investigated quantitatively. This study shows that a change of material from nickel or silicon to copper only has a significant percentage effect on heat resistance at high channel height to width ratios, and this difference is more pronounced at higher fluid velocities. Fluid flux is an important parameter in cooling performance; however, performance does not increase in proportion with fluid flux when inefficient heat spreading occurs in the liquid channel.

The temperature distribution on a chip containing a hot-spot while it is cooled by a microfluidic heat sink was simulated and studied. These simulations were performed for 1 mm and 3 mm wide hot spots. This study showed that a change of material from nickel or silicon to copper can have a pronounced effect. It was also shown that the thickness of the top layer of the heat sink, between the heat source and fluid channels, affects the peak temperature with two competing mechanisms which work opposite to each other; thermal resistance between the heat source surface and fluid, and axial heat conduction in solid. Simulation results showed the optimum value for this thickness is ~25 μm for heatsinks fabricated from nickel, ~50 μm for heatsinks fabricated from

silicon, and ~150 μm for heat sinks fabricated from copper. Simply, it is directly proportional to the thermal conductance of the solid.

Simulations of transient state show that the characteristics of the microfluidic heatsink is with a good approximation like a first order differential equation and its rise time and fall time are like a first order exponential term. Hence microfluidic heatsink can be modeled as a first order RC circuit. From steady state simulations we know that the thermal resistance of this heatsink mostly depends on the fluid velocity. The thermal capacitance for each case is obtained from the temperature rise time at the transient simulation result. From the thermal capacitance values obtained in this way it is concluded that the overall thermal capacitance mostly depends on the thermal capacitance of the solid part, and it is less dependent on the fluid flow. The other result is that the peak temperature reached for the short heat pulses is in some cases highly dependent on the thermal capacitance of the solid material. The peak temperature for copper heatsink is a lot less than that for silicon, because its time constant is smaller.

9.2. Future Work

This work can be continued and completed in three directions: simulation, fabrication, and test. The envisioned work in each of these areas is explained separately.

9.2.1. Simulation

In the steady state analysis, there is a lot of work that can be done about on heat sources with hot spot. The effect of different parameters like channel height and width on the peak temperature can be studied. If larger simulations can be done, small hot spots

(not hot bands in this work) with the size of for example 1 × 1 mm can be used and the effect of changing its position or size can be studied. Even the heat generation profile of the real chips that include two or more hot spots can be used for simulations.

In the transient analysis, in both cases of uniform heat input and heat input with hot spot, the effect of the heat sink parameters on the peak temperature and rise time and fall time of the surface temperature can be studied.

All of these simulations should be done with the purpose of finding the best heatsink structure which provides the least peak temperature in both steady and transient states for a certain amount of fluid flow and pressure drop.

9.2.2. Fabrication

Fabrication of a complete microfluidic heatsink based on electroplating can be accomplished by improvements and advancements in all three steps of lithography, electroplating, and bonding. For lithography step it is better to use a photoresist which can make the height of at least 50 μm. There are some negative thick layer photoresists that can be used for this purpose too. Among the positive photoresists, a suitable one that I found is AZ 50XT photoresist from AZ Electronic Materials. It is specially for plating applications and can make 40 – 80 μm layers with a single cot and up to 120 μm with a double coat. It can produce structures with the aspect ratio of 3 and excellent side walls.

The discussed electroplating method is sufficient for making layers of up to ~150 μm thick, but for thicker layers or for fabrication at a higher rate, this method needs to be improved. The most important step that needs to be improved is the bonding method.

Instead of a pure tin layer, a material like gold/tin (AuSn) which doesn't oxidize and is a strong material for soldering is better to be used.

9.2.3. Test

Testing and characterizing the microfluidic heat sink is an issue and needs special equipments. The main thing is a sensor which measures temperature on the heat sink. There are several methods for this. One method is using thermistors. Making such a sensor is fairly easy and a small set of thermistors can give a profile of temperature along the channels.

Figure 9-1 shows a fixture designed based on thermistors for testing the microfluidic heat sinks.

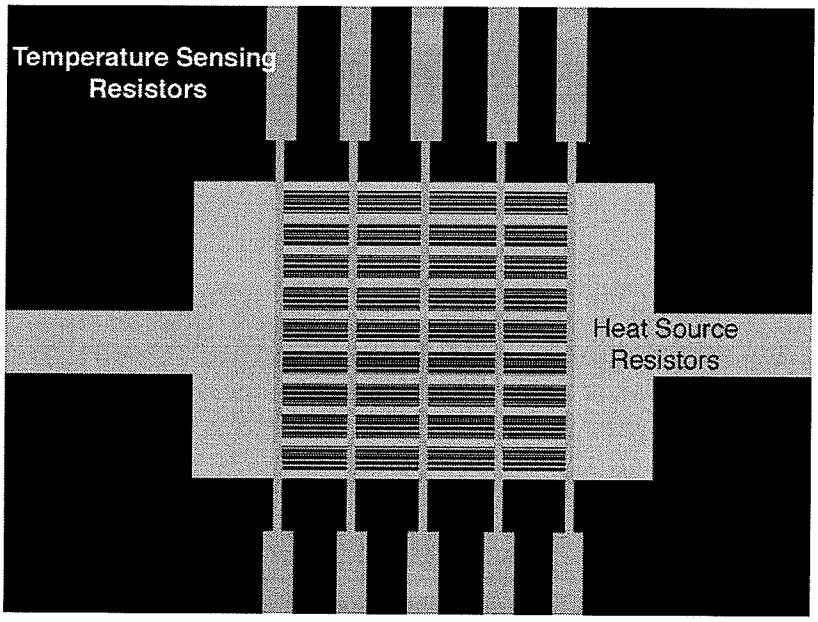

Figure 9-1. Test fixture used for testing the microfluidic heat sink. It consists of two metal layers, one for input heat generation, and one for temperature measurement.

This structure is made of two resistor layers. One layer at the bottom is for generating heat, and the other layer is for sensing and measuring the temperature. These resistors can be made with chrome or titanium. An insulator layer of Si separated two resistor layers, and another Si layer covers the top resistor layer. All of these layers are made by sputtering. Windows are opened by wet and plasma etching for electrical contact to the resistors. Silicon is etched by plasma etching and chrome is etched by wet etching. Five sensing resistors would be made to measure the temperature at five points along the microchannel structure. The length and width of the microfluidic heat sink is 1 cm. hence the size of the main area of this test structure covered by resistors is 1×1 cm^2.

There are a few other methods for measuring the temperature profile on the heat sink. Instead of thermistors, thermocouple sensors can be used. There are some experimental methods to examine these simulation results for the surfaces including hot spots. Such a method should propose a suitable way to measure the temperature distribution on the whole surface.

The first method is based on Infra Red (IR) imaging. In [14 & 86] detailed power maps are shown of fully operational microprocessors obtained by imaging the temperature-dependent IR emission of chips that are cooled by a custom designed IR transparent heat sink.

Another good technique to observe the temperature profile on a hot surface like a chip is using Thermochromic Liquid Crystals (TLC) [87]. In this method, a thin layer of a special liquid crystal is put on top of the heatsink. The color of the liquid crystal changes with temperature, and shows the temperature on every point of the heatsink surface.

The third method is using another chip at the size of the main chip. This extra chip contains thousands of very small temperature sensors, in an array which covers the whole surface. Each of these temperature sensors can be a small circuit unit, like a ring-oscillator, whose oscillation frequency depends on temperature. Each of these sensors appears as a pixel in the final temperature image of the surface. The time constant of such sensors can be very short, and hence such a method is suitable even for transient study of hot spots [88 & 89].

Each of the mentioned methods have advantages and disadvantages based on the parameters like their response time, precision, distance between the sensor and the hot surface, and need for transparent cover on the hot surface or microfluidic heat sink. The advantage of the mentioned three methods for observing a surface with hot spots is their good spatial and temporal resolution. Hence they are better choices than arrays of thermistors or thermocouples for studying the heat sources with hot spots or transients.

In Figure 9-2 the schematic of the test system is demonstrated. This is an open loop system, meaning that the heated water goes to the drain and is not reused. DI water is used for testing the heat sink. At the input, using a flow meter, a thermometer and a pressure meter, the total flux, temperature and pressure of the input water are measured. After the pressure meter, two valves are implemented to direct the water through the heat sink, or bypass the heatsink. After the heatsink there is again a thermometer to measure the temperature of the output water. In this way we can measure the temperature difference of the input and output water, and then the total power transferred to water. The heat source fixture is at the bottom of the copper heat sink and using a high power voltage source and a volt meter and an ampere meter the heat dissipation on the heat

generating resistor is controlled. When the system reaches the steady state, using an ohm meter the resistances of the thermistors are measured, and in this way the temperatures of the five points on the heat sink and along the channels are obtained.

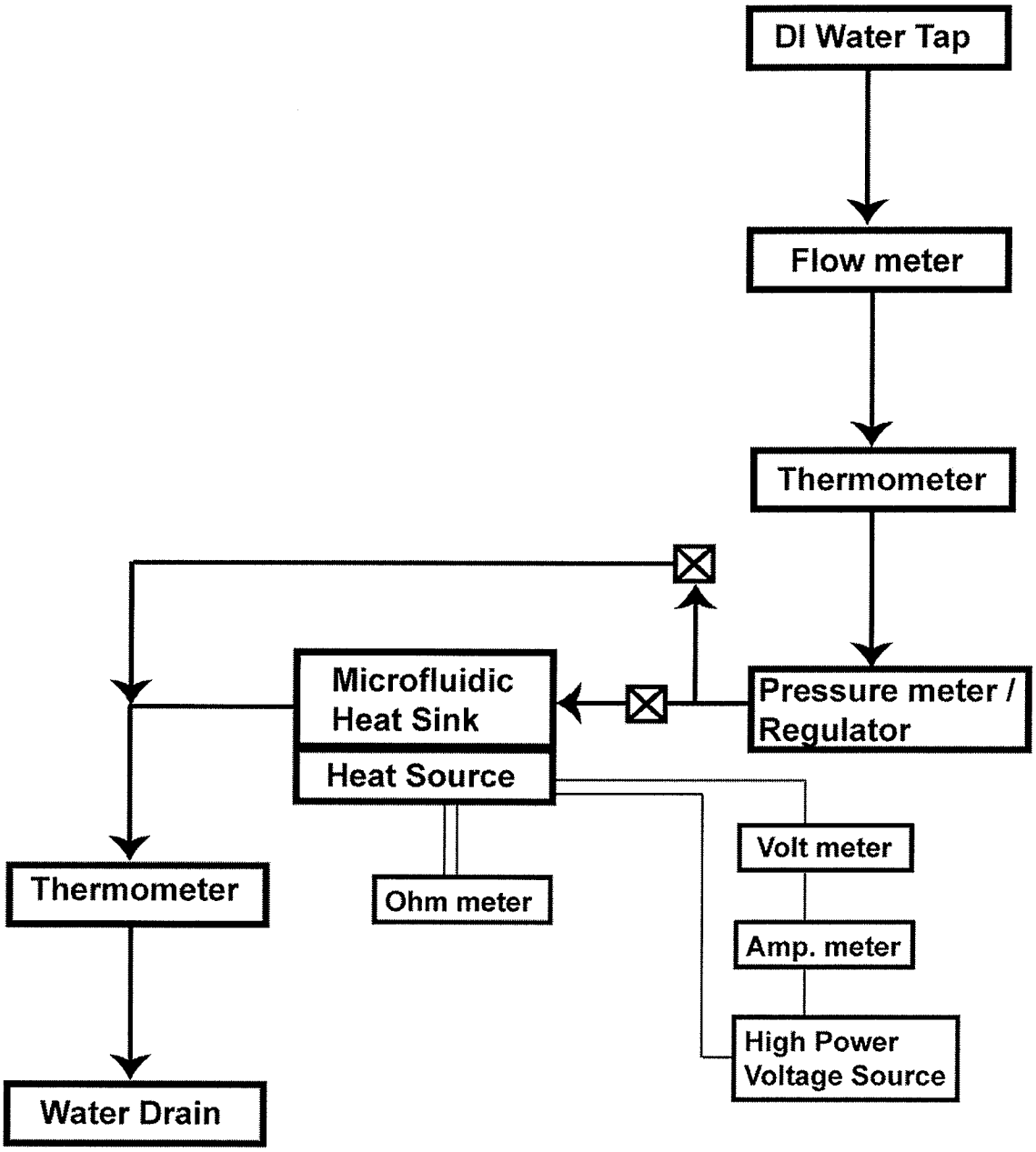

Figure 9-2. Diagram of the test system of the microfluidic heat sink.

Chapter 10

References

[1] P.E. Ross, "Beat the Heat", IEEE Spectrum Magazine, May 2004, pp. 38-43.

[2] M. Vogel and G. Xu, "Low Profile Heat Sink Cooling Technologies for Next Generation CPU Thermal Design", Electronics Cooling Magazine, Vol. 11, No. 1, 2005.

[3] Massoud Pedram, and Shahin Nazarian, "Thermal Modeling, Analysis, and Management in VLSI Circuits: Principles and Methods", Proceedings of the IEEE, Vol. 94, No. 8, August 2006, pp. 1487-1501.

[4] B. Guenin, "Packaging Challenges for High Heat Flux Devices", Electronics Cooling Magazine, Vol. 12, No. 3, 2006.

[5] J.L. Deeney and C.M. Ramsey, "Comparison of Finite-Difference and SPICE Tools for Thermal Modeling of the Effects of Nonuniform Power Generation in High-Power CPUs", The Hewlett-Packard Journal, Vol. 50, No. 1, Nov. 1998, pp. 37-45.

[6] V.H. Adams and K. Ramakrishna, "Impact of On-Die Discrete Heating on Thermal Performance Characteristics of Silicon Based IC Electronic Packages", Proceedings of the 1999 ASME IMECE, Nashville, TN, ASME Vol. EEP-Vol. 104, Nov. 14-19, 1999, pp. 99-106.

[7] Suresh V. Garimella, Vishal Singhal and Dong Liu, "On-Chip Thermal Management with Microchannel Heat Sinks and Integrated Micropumps", Proceedings of the IEEE, Vol. 94, No. 8, August 2006, pp. 1534-1548.

[8] D.B. Tuckerman and R.F.W. Pease, "High-Performance Heat Sinking for VLSI", IEEE Electron Devices Letters, Vol. EDL-2, No. 5, 1981, pp. 126-129.

[9] http://en.wikipedia.org/wiki/Heat#Heat_transfer_mechanisms

[10] http://en.wikipedia.org/wiki/Thermal_conductivity

[11] W. Owhaib and B. Palm, Experimental investigation of single-phase convective heat transfer in circular microchannels, Experimental Thermal and Fluid Science 28 (2004), pp. 105-110.

[12] Hsin-Chih Tim Yeh, Fabrication and Cooling Test of High-Aspect-Ratio Electroplated Microchannels, M.Sc. Thesis, UCLA, 1998.

[13] COMSOL Multiphysics, Produced by COMSOL AB, Tegnérgatan 23, SE-111 40 Stockholm, Sweden.

[14] Tze-Chiang Chen, Where CMOS is going: Trendy Hype vs. Real Technology, IEEE SSCES Newsletter, Vol. 20, No. 3, Sep. 2006, pp. 6.

[15] S.F. Choquette, M. Faghri, M. Charmchi, Y. Asako, "Optimum Design of Microchannel Heat Sinks", Microelectromechanical Systems (MEMS), ASME DSC-Vol. 59, 1996, pp. 115-126.

[16] C. Yang, D. Li, and J. Masliyah, "Modeling Forced Liquid Convection in Rectangular Microchannels with Electrokinetic Effects", International Journal of Heat and Mass Transfer, Vol. 41, 1998, pp. 4229-44249.

[17] A. Federov, and R. Viskanta, "Three-Dimensional Conjugate Heat Transfer in the Microchannel heat Sink for electronic Packaging", International Journal of Heat and Mass Transfer, Vol. 43, 2000, pp. 399-415.

[18] W. Qu, and I. Mudawar, "Analysis of Three-Dimensional Heat Transfer in Micro-Channel Heat Sinks", International Journal of heat and Mass Transfer, Vol. 45, 2002, pp. 3973-3985.

[19] R.W. Knight, D. Hall, J. Goodling, and R. Jaeger, "Heat Sink Optimization with Application to Microchannels", IEEE Transactions on Components, Hybrids, and Manufacturing Technology, Vol. 15, No. 5, 1992, pp. 832-842.

[20] W. Qu, and I. Mudawar, "Experimental and Numerical Study of Pressure Drop and Heat Transfer in a Single-Phase Micro-channel Heat Sink", International Journal of Heat and Mass Transfer, Vol. 45, 2002, pp. 2549-2565.

[21] K.C. Toh, X.Y. Chen and J.C. Chai, "Numerical Computation of Fluid Flow and Heat Transfer in Microchannels", International Journal of Heat and Mass Transfer, Vol. 45, 2002, pp. 5133-5141.

[22] X.F. Peng, and G.P. Peterson, "Convective Heat Transfer and Fluid Flow Friction for Water Flow in Microchannel Structures", International Journal of heat and Mass Transfer, Vol. 39, No. 12, 1996, pp. 2599-2608.

[23] X.F. Peng, and G.P. Peterson, "The Effect of Thermofluid and Geometrical Parameters on Convection of Liquids Through Rectangular Microchannels", International Journal of heat and Mass Transfer, Vol. 38, No. 4, 1995, pp. 755-758.

[24] X. Wei, and Y. Joshi, "Optimization Study of Stacked Micro-Channel Heat Sinks for Micro-Electronic Cooling", IEEE Transactions on Components and Packaging Technologies, Vol. 26, No. 1, 2003, pp. 55-61.

[25] K. Kawano, K. Minakami, H. Iwasaki and M. Ishizuka, "Microchannel Heat Exchanger for Cooling Electrical Equipment", Proceedings of the ASME Heat Transfer Division, Vol. 3. 1998, pp. 173-180.

[26] W. Qu, G.M. Mala, and D. Li, "Heat Transfer for Water Flow in Trapezoidal Silicon Microchannels", international Journal of Heat and Mass Transfer, Vol. 43, 2000, pp. 3925-3936.

[27] T. Harms and et al, "Experimental Investigation of Heat Transfer and Pressure Drop Through Deep Microchannels in a (110) Silicon Substrate", Proceedings of the ASME Heat Transfer Division, Vol. 1, 1997, pp. 347-357.

[28] T. Harms, M. Kazmierczak, and F.M. Gerner, "Developing Convective Heat Transfer in Deep Rectangular Microchannels", International Journal of Heat and Fluid Flow, Vol. 20, 1999, pp. 149-157.

[29] Tze-Chiang Chen, Where CMOS is going: Trendy Hype vs. Real Technology, IEEE SSCES Newsletter, Vol. 20, No. 3, Sep. 2006, pp. 6.

[30] J.L. Deeney, and C.M. Ramsey, "Comparison of Finite-Difference and SPICE Tools for Thermal Modeling of the Effects of Nonuniform Power Generation in High-Power CPUs", The Hewlett-Packard Journal, Vol. 50, No. 1, Nov. 1998, pp. 37-45.

[31] V.H. Adams, and K. Ramakrishna, "Impact of On-Die Discrete Heating on Thermal Performance Characteristics of Silicon Based IC Electronic Packages",

Proceedings of the 1999 ASME IMECE, Nashville, TN, ASME Vol. EEP-Vol. 104, Nov. 14-19, 1999, pp. 99-106.

[32] S. Sharifian Attar M.C.E. Yagoub F. Mohammadi, "New Electro-Thermal Integrated Circuit Modeling using Coupling of Simulators", Proceedings of the IEEE Canadian Conference on Electrical and Computer Engineering, 2006, pp. 930-934.

[33] J.R. Rujano, M.M. Rahman, "Transient Response of Microchannel Heat Sinks in a Silicon Wafer", Journal of Electronic Packaging, Vol. 119, 1997, pp. 239-246.

[34] G. Joyce, H.M. Soliman, "Analysis of The Transient Single-Phase Thermal Performance of Micro-Channel Heat Sinks", Heat Transfer Engineering, Vol. 30, No. 13, pp. 1058-1067.

[35] L. Jiang, M. Wong, and Y. Zohar, "Transient Temperature Performance of an Integrated Micro-Thermal System", Journal of Micromechanics and Microengineering, Vol. 10, 2000, pp. 466-476.

[36] http://www.cooligy.com/

[37] M. Le Berre, S. Launay, V. Sartre, and M. Lallemand, "Fabrication and Experimental Investigation of Silicon Micro Heat Pipes for Cooling Electronics", Journal of Micromechanics and Microengineering, Vol. 13, 2003, pp. 436-441.

[38] X.F. Peng, B.X. Wang, G.P. Peterson, and H.B. Ma, "Experimental Investigation of Heat Transfer in Flat Plates with Rectangular Microchannels", International Journal of Heat and Mass Transfer, Vol. 38, No. 1, 1995, pp. 127-137.

[39] J. Brandner, L. Bohn, T. Henning, U. Schygulla, and K. Schubert, "Microstructure Heat Exchanger Applications in Laboratory and Industry",

Proceedings of the Fourth International Conference on Nanochannels, Microchannels, and Minichannels, June 19-21, 2006, Limerick, Ireland.

[40] C. Yang, C. Yeh, W. Liu, and B. Yang, "Advanced Micro Heat Exchanger for High Heat Flux", Proceedings of the Fourth International Conference on Nanochannels, Microchannels, and Minichannels, June 19-21, 2006, Limerick, Ireland.

[41] http://www.gigabyte.com.tw/Products/LiquidCooling/

[42] http://www.pipeline-communications.com/

[43] http://www.mikrostechnologies.com/

[44] T. Brunschwiler, H. Rothuizen, M. Fabbri, U. Kloter, and B. Michel, "Direct Liquid Jet-Impingement Cooling With Micronsized Nozzle Array and Distributed Return Architecture", Proceedings of the IEEE 10th Intersociety Conference on Thermal and Thermomechanical Phenomena in Electronics Systems (ITHERM'06), 2006, pp.196-203.

[45] B. Dang, M. Bakir, J. Meindl, "Integrated Thermal Fluidic i/O Interconnects for an On-Chip Microchannel Heat Sink", IEEE Electron Devices Letters, Vol. 27, No. 2, pp. 117-119.

[46] Hsin-Chih Tim Yeh, Fabrication and Cooling Test of High-Aspect-Ratio Electroplated Microchannels, M.Sc. Thesis, UCLA, 1998.

[47] X. Wei, Stacked Microchannel Heat Sinks for Liquid Cooling of Microelectronics Devices, PhD Thesis, Georgia Institute of Technology, 2004.

[48] E. Colgan and et al, "High Performance and Sub-Ambient Silicon Microchannel Cooling", Proceedings of the Fourth International Conference on Nanochannels, Microchannels, and Minichannels, June 19-21, 2006, Limerick, Ireland.

[49] Ravi Mahajan, Chia-Pin Chiu and Greg Chrysler, "Cooling a Microprocessor Chip", Proceedings of the IEEE, Vol. 94, No. 8, August 2006, pp. 1476-1486.

[50] Avram Bar-Cohen, Mehmet Arik, and Michael Ohadi, "Direct Liquid Cooling of High Flux Micro and Nano Electronic Components", Proceedings of the IEEE, Vol. 94, No. 8, August 2006, pp. 1549-1570.

[51] Tze-Chiang Chen, Where CMOS is going: Trendy Hype vs. Real Technology, IEEE SSCES Newsletter, Vol. 20, No. 3, Sep. 2006, pp. 6.

[52] P.H. Oosthuizen and D. Naylor, An Introduction to Convective Heat Transfer Analysis, McGraw Hill, 1999.

[53] J. P. Holman, Heat Transfer, 6th Edition, McGraw Hill, 1986.

[54] COMSOL Multiphysics User's Guide version 3.5a, COMSOL AB, Sweden, 2008.

[55] R.K. Shah, and A.L. London, "Laminar Flow Forced Convection in Ducts", 1978, Academic Press, New York.

[56] S.G. Kandlikar, S. Garimella, D. Li, S. Colin, and M.R. King, Heat Transfer and Fluid Flow in Minichannels and Microchannels, Elsevier, 2006.

[57] R. Riddle and et al, "Design Calculations for the Microchannel Heatsink", Proceedings of the Technical Program – National Electronic Packaging and Production Conference, Vol. 1, 1991, pp. 161-171.

[58] J. Brandner, L. Bohn, T. Henning, U. Schygulla, and K. Schubert, "Microstructure Heat Exchanger Applications in Laboratory and Industry", Proceedings of the Fourth International Conference on Nanochannels, Microchannels, and Minichannels, June 19-21, 2006, Limerick, Ireland.

[59] B.G. Subramani, and P. Selvaganapathy, "Surface Micromachined PDMS Microchannels", Proceedings of the Fifth International Conference on Nanochannels, Microchannels, and Minichannels, June 18-20, 2007, Puebla, Mexico.

[60] B. Dang, M. Bakir, J. Meindl, "Integrated Thermal Fluidic I/O Interconnects for an On-Chip Microchannel Heat Sink", IEEE Electron Devices Letters, Vol. 27, No. 2, pp. 117-119.

[61] A. J. Bard, and L. R. Faulkner, Electrochemical Methods, John Wiley & Sons, 1980, New York.

[62] J. T. Hinatsu, and F. R. Foulkes, "Diffusion Coefficient for Copper (II) in Aqueous Cupric Sulfate-Sulfuric Acid Solutions", Journal of Electrochemical Society, Vol. 136, 1989, pp. 125-132.

[63] W. Tsai, C. Wan, and Y. Wang, "Pulsed Current and Potential Response of Acid Copper System with Additives and the Double Layer Effect", Journal of Electrochemical Society, Vol. 149, No. 5, 2002, pp. C229-C236.

[64] http://www.wikipedia.com

[65] R. Caban, and T. W. Chapman, "Statistical Analysis of Electrode Kinetics Measurements-Copper Deposition from $CuSO_4$-H_2SO_4 Solutions", Journal of Electrochemical Society, Vol. 124, 1977, pp. 1371-1379.

[66] L.J. Durney, Electroplating Engineering Handbook, 4th Edition, Van Nostrad, 1984, Berkshire.

[67] C. Van Horn, Pulsed Current Plating, in ASM Handbook, ASM International, 1994.

[68] E. J. Podlaha, and D. Landolt, "Pulse Reverse Plating of Nanocomposite Thin Films", Journal of Electrochemical Society, 1997, Vol. 144, pp. L200-L202.

[69] K. Ogura, K. Sakurai, and S. Uehara, "Room Temperature-Coloration of Stainless Steel by Alternating Potential Pulse Method", Journal of Electrochemical Society, 1994, Vol. 141, pp. 648-651.

[70] L.J. Durney, Electroplating Engineering Handbook, 4th Edition, Van Nostrad, 1984, Berkshire.

[71] H.Y. Cheh, "The Limiting Rate of Deposition by P-R Plating", Journal of Electrochemica Society, Vol. 118, No. 7, 1971, pp. 1132-1134.

[72] L. I. Antropov, Theoretical Electrochemistry, Mir Publishers, 1977, Moscow.

[73] J. D. Lisius, and P. W. Hart, "Mass Transfer Requirements for Alternating Polarity, Alternating Voltage Synthesis", Journal of Electrochemical Society, Vol. 138, 1991, pp. 3678-3685.

[74] C.J. Chen, and C.C. Wan, "A Study of the Current Efficiency Decrease Accompanying Short Pulse Time for Pulse Plating", Journal of Electrochemical Society, Vol. 136, 1989, pp. 2850-2855.

[75] N. Tantavichet, and M. Pritzker, "Low- and High-Frequency Pulse Current Plating of Copper onto a Rotating Disk Electrode", Journal of Electrochemical Society, Vol. 149, No. 5, 2002, pp. C289-C299.

[76] C. Van Horn, Pulsed Current Plating, in ASM Handbook, ASM International, 1994.

[77] W. Tsai, C. Wan, and Y. Wang, "Pulsed Current and Potential Response of Acid Copper System with Additives and the Double Layer Effect", Journal of Electrochemical Society, Vol. 149, No. 5, 2002, pp. C229-C236.

[78] S. Roy, and D. Landolt, "Determination of the Practical Range of Parameters during Reverse-Pulse Current Plating", Journal of applied Electrochemistry, Vol. 27, 1997, pp. 299-307.

[79] A. Pesco, and H.Y. Cheh, "Mass Transfer in Alternating Current Electrolysis", Journal of Electrochemica Society, Vol. 131, No. 10, pp. 2259-2266.

[80]] N. Tantavichet, and M. Pritzker, "Low- and High-Frequency Pulse Current and Pulse Reverse Plating of Copper", Journal of Electrochemical Society, Vol. 150, No. 10, 2003, pp. C665-C677.

[81] K. Viswanathan, M.A. Farrell Epstein, and H.Y. Cheh, "The Application of Pulsed Current Electrolysis to a Rotating-Disk Electrode System", Journal of Electrochemica Society, Vol. 125, No. 11, pp. 1772-1776.

[82] J.T. Hinatsu, and F.R. Foulkes, "Diffusion Coefficients for Copper (II) in Aqueous Cupric Sulfate-Sulfuric Acid Solutions", Journal of Electrochemica Society, Vol. 136, No. 1, pp. 125-131.

[83] N.F. Kazakov, Diffusion Bonding of Materials, Pergamon Press, 1985.

[84] N.T. Nguyen and S.T. Wereley, Fundamentals and Applications of Microfluidics, 2nd Edition, Artech House, 2006.

[85] http://www.micralyne.com

[86] P. Paik, K. Chakrabarty and V. Pamula, Adaptive Cooling of Integrated Circuits Using Digital Microfluidics, Artech House, 2007, page 36.

[87] K. Azar, D.J. Farina, "Measuring Chip Temperatures with Thermochromic Liquid Crystals", Electronics Cooling Magazine, Vol. 3, No. 1, Jan. 1997.

[88] J. Altet, W. Claeys, S. Dilhaire and A. Rubio, "Dynamic Surface Temperature Measurement in ICs" Proceedings of the IEEE, Vol. 94, No. 8, August 2006, pp. 1519-1533.

[89] J.C. Tsang, J.A. Kash, D.P. Vallett, "Picosecond Imaging Circuit Analysis", IBM Journal of Research and Devlopment, Vol. 44, No. 4, 2000, pp. 583-603.